AD-A035 321

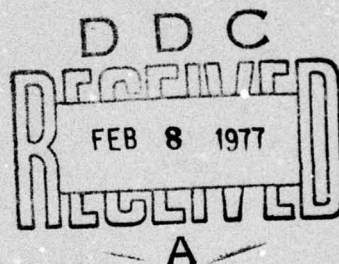# PRESSURE DRIVEN ANGLE OF ATTACK INDICATING SYSTEM

AIR FORCE ACADEMY, COLORADO

JANUARY 1976

ADA035321

PRESSURE DRIVEN ANGLE OF ATTACK INDICATING SYSTEM

DEPARTMENT OF AERONAUTICS
U. S. AIR FORCE ACADEMY, COLORADO 80840

JANUARY 1976

DDC

FEB 8 1977

RECEIVED

A

FINAL REPORT: MARCH 1972 - MARCH 1975

Distribution unlimited; approved for public release.

AIR FORCE ARMAMENT LABORATORY

AIR FORCE SYSTEMS COMMAND • UNITED STATES AIR FORCE

EGLIN AIR FORCE BASE, FLORIDA

REPORT DOCUMENTATION PAGE		READ INSTRUCTIONS BEFORE COMPLETING FORM
1. REPORT NUMBER AFATL-TR-76-10	2. GOVT ACCESSION NO.	3. RECIPIENT'S CATALOG NUMBER
4. TITLE *(and Subtitle)* PRESSURE DRIVEN ANGLE OF ATTACK INDICATING SYSTEM		5. TYPE OF REPORT & PERIOD COVERED Final Report: March 1972 to March 1975
		6. PERFORMING ORG. REPORT NUMBER
7. AUTHOR(s) Roger W. Gallington James W. Christian		8. CONTRACT OR GRANT NUMBER(s)
9. PERFORMING ORGANIZATION NAME AND ADDRESS Department of Aeronautics U. S. Air Force Academy, CO 80840		10. PROGRAM ELEMENT, PROJECT, TASK AREA & WORK UNIT NUMBERS ILIR 7411 DRS 61102F 7905-01-29
11. CONTROLLING OFFICE NAME AND ADDRESS Air Force Armament Laboratory Armament Development and Test Center Eglin Air Force Base, Florida 32542		12. REPORT DATE January 1976
		13. NUMBER OF PAGES 100
14. MONITORING AGENCY NAME & ADDRESS(if different from Controlling Office)		15. SECURITY CLASS. (of this report) UNCLASSIFIED
		15a. DECLASSIFICATION/DOWNGRADING SCHEDULE

16. DISTRIBUTION STATEMENT *(of this Report)*

Distribution unlimited; approved for public release.

17. DISTRIBUTION STATEMENT *(of the abstract entered in Block 20, if different from Report)*

18. SUPPLEMENTARY NOTES

Available in DDC.

19. KEY WORDS *(Continue on reverse side if necessary and identify by block number)*

Angle of Attack Measurement
Angle of Sideslip Measurement

20. ABSTRACT *(Continue on reverse side if necessary and identify by block number)*

Technically inclined flyers have long recognized the importance to the pilot of angle of attack information. Unfortunately, a reliable, accurate, and low cost angle of attack indicator has not been available. From the outset, the goal of this research has been to develop an angle of attack indicator as simple, accurate, reliable, and inexpensive as the common airspeed indicator so that it could be used as a primary landing approach aid and for the other flight control functions. This report describes the solution to that problem.

Item 20: (CONCLUDED)

The pressure driven angle of attack indicating system usually consists of an external probe and an internally mounted indicator, the two elements being connected by three tubes. The approach is mainly experimental although extensive analytics are provided to aid engineers in the design of pressure driven angle of attack indicating systems for almost any application. Accuracy of $\pm$0.08 degree was demonstrated in the wind tunnel. Accuracy of $\pm$0.17 degree was demonstrated in flight. Flight tests showed the response characteristics to be ideal for pilot use. The pressure driven angle of attack indicating system equals or exceeds the best of other systems in all performance areas.

ia

PREFACE

This report documents work performed by the Department of Aeronautics, United States Air Force Academy, Colorado, during the period from March 1972 to March 1975 under Project ILIR 7411. For the first year, the effort consisted of a few cadet projects defined and supervised by the authors. The Frank J. Seiler Research Laboratory began supporting work on angle of attack indicators in early 1973. In the summer of 1973 the Air Force Armament Laboratory also began to support the project.

The authors gratefully acknowledge the administrative support of Major Charles Simon of the Frank J. Seiler Research Laboratory. Dr. George B. Findley (DLMA) was program manager for the Air Force Armament Laboratory.

This technical report has been reviewed and is approved for publication.

FOR THE COMMANDER

CLIFFORD H. ALLEN, JR., Colonel, USAF
Chief, Guided Weapons Division

i**b**
(The reverse of this page is blank)

TABLE OF CONTENTS

iii

LIST OF FIGURES

LIST OF FIGURES (CONTINUED)

LIST OF FIGURES (CONCLUDED)

LIST OF TABLES

LIST OF SYMBOLS

a	constant defined for Equation (5)
b	constant defined for Equation (5), distance between crease planes at $c_\alpha = 0$
C_L	aircraft lift coefficient
C_D	aircraft drag coefficient
C_α	pressure coefficient depending primarily on angle of attack - an odd function
$C_{\alpha 1}$	conventional pressure coefficient at port $\alpha 1$
C_β	pressure coefficient depending primarily on angle of sideslip - an odd function
CAS	calibrated airspeed
E	modulus of elasticity
e	base of the natural logarithm
F	fluid mechanical resistance
F_ℓ	force supportable by tensile stresses in the left diaphragm
$F_{\ell_{req}}$	force required of left diaphragm to support backing plate assembly
F_{max}	maximum force supportable by tensile stresses in diaphragm
F_r	force supportable by tensile stresses in right diaphragm
$F_{r_{req}}$	force required of right diaphragm to support backing plate assembly
f	a frictional force
g	acceleration
k	constant in equation for identical left and right paraboloids
k_ℓ	constant in equation for left paraboloid
k_r	constant in equation for right paraboloid
ℓ	length of connecting tube, length of link in balance type instrument
M	Mach number
m_a	equivalent mass of air in tubes
m_b	equivalent mass of backing plate assembly and attached mechanism
n	load factor

n_ϕ	load factor calculated from bank angle
n_θ	load factor calculated from indicated angle of attack
p	pressure difference across diaphragms, pressure at a general point on probe or wing surface
p_ℓ	pressure in left chamber of instrument
p_m	pressure in middle chamber of instrument
p_o	stagnation pressure of stream
p_{0_2}	stagnation pressure behind normal shock
p_r	pressure in right chamber of instrument
p_s	pressure at static port on probe
p_t	pressure at center port on probe
p_α	static pressure of stream
$p_{\alpha 1}$	pressure at upper port on probe
$p_{\alpha 2}$	pressure at lower port on probe
p_{β_1}	pressure at right port on probe
p_{β_2}	pressure at left port on probe
q	free stream dynamic pressure
q_o	pressure coefficient depending primarily on Mach number and independent of angle of attack
q_α	pressure coefficient depending primarily on angle of attack - an even function
R	radius of crease at $C_\alpha = 0$
R_e	Reynold's number based on probe diameter or airfoil chord
r	distance from axis of symmetry to surface of backing plate or diaphragm, length of lever in balance type instrument
r_c	general diaphragm crease radius
r_ℓ	left diaphragm crease radius
r_r	right diaphragm crease radius
r_t	radius of connecting tube
T	diaphragm thickness
t	time

t_c — circumferential tension in diaphragm material - along parallels

t_r — radial tension in diaphragm material - along meridians

V, V_∞ — velocity of free stream

V_ℓ — volume of left chamber

V_r — volume of right chamber

x — displacement of backing plate assembly from $C_\alpha = 0$ position

$\bar{x}$ — non-dimensional displacement of backing plate assembly defined differently for different diaphragm shapes

y_ℓ — for spherical diaphragms and backing plates the distance from the plane of the left diaphragm crease at $C_\alpha = 0$ to the center of curvature

y_r — for spherical diaphragms and backing plates the distance from the plane of the right diaphragm crease at $C_\alpha = 0$ to the center of curvature

z_ℓ — distance from the apex of the left diaphragm or backing plate in the axial direction

z_r — distance from the apex of the right diaphragm or backing plate in the axial direction

α — angle of attack

β — angle of sideslip, azimuthal angle for diaphragm and backing plate strength calculations

Δ — prefix indicating a finite change

δ — prefix indicating an infinitesimal change, output of balance type instrument defined in Figure 4

θ — angle in balance type instrument defined in Figure 4, angle backing plate or diaphragm surface makes with a plane perpendicular to the axis of symmetry, output of the diaphragm type pressure coefficient meter

θ_ℓ — angle left conical backing plate makes with a plane perpendicular to the axis of symmetry

θ_r — angle right conical backing plate makes with a plane perpendicular to the axis of symmetry

ρ — radius of curvature of left and right spherical diaphragms and backing plates if equal, distance from axis of symmetry to surface of left and right paraboloidal diaphragms and backing plates if identical

ρ_ℓ radius of curvature of left spherical diaphragm and backing plate, distance from axis of symmetry to surface of left paraboloidal diaphragm and backing plate

ρ_r radius of curvature of right spherical diaphragm and backing plate, distance from axis of symmetry to surface of right paraboloidal diaphragm or backing plate

ρ_∞ density of free stream, density of air in tubes

ϕ bank angle

τ_i time constant associated with inertia

τ_v time constant associated with viscosity

μ viscosity, Poisson's ratio

SECTION I

INTRODUCTION

The objective of this report is to describe a new, more accurate and reliable but less expensive way to measure angle of attack and angle of sideslip in flight. It is instructive to review how angle of attack and angle of sideslip measurements have been used in the past. With a small stretch of the imagination one can suggest additional uses that become possible as a result of the reduced cost. A survey of the merits and deficiencies of existing systems describes the state of the art to which the new system must be compared. A brief description of the principle of operation of the new system shows how most deficiencies of the older systems are overcome. Finally, a short chronology of the development of the new system reveals certain other possible systems which have not yet been fully investigated.

USES OF ANGLE OF ATTACK AND ANGLE OF SIDESLIP INFORMATION

Angle of attack indicators and angle of sideslip indicators have been extensively used in applications where the cost of the system is relatively unimportant--that is, in expensive and heavy aircraft such as those used by the military services. Lambdin[1] has conveniently summarized Air Force uses of angle of attack information and his table is reproduced here.

In the cases of aircraft listed in Table 1 which are used in air-to-air combat, the angle of attack indicator also warns of impending buffet or high speed stall during maneuvering. More recent applications include the AC-130 Gunship[2] where accurate angle of attack information was a

---

[1] Lambdin, R. L., "Standardized Angle of Attack System Feasibility Study," Aeronautical Systems Division Technical Memorandum, ASNF 68-4, August 1968.

[2] Gunship Operational Flight Program, Part II, Specification for Gunship Software Product Specification, Volume II, Prepared for Gunship System Program, Air Force Systems Command, Wright Patterson Air Force Base, Ohio, Contract F33-657-71-C-0595, 15 Sept 1971 Revised 17 Sept 1973, IBM File No. 71-M-54-001.

required input to the fire control system and the F-106 demonstrator of the "Snap Shoot Gunsight"[3,4] where both angle of attack and sideslip angles were required by the fire control systems. Lead computing sights also require the measurement of angle of attack and sideslip angle.[5] All functions listed in Table 1 are appropriate to any aircraft except for fire control, engine control, and terrain avoidance which apply primarily to military missions.

TABLE 1. AIR FORCE USE OF ANGLE OF ATTACK

Function	Definition	Examples	
1. Fire control computer input	Provide input to missile guidance and release point system	F-102 F-106 F-111	YF 12
2. Flight control system	Stick shaker - Stick pusher	C-123 C-133 C-141	C-5A F-101 F-104
3. Gust alleviators	Input to system that automatically conditions aircraft configuration for local gusting	Rough rider and other severe weather penetration aircraft	
4. Stall warning	Gives indication of impending stall	C-123 C-133 C-141	C-5A F-4C T-37
5. Flight instrument compensator	Airspeed, Mach, altitude display data corrected for angle of attack errors	F-101 F-104 F-106	F-4 F-111
6. Cruise control	Obtain max endurance, etc. based on best lift-to-drag ratio	None	

_____

[3]D. Donato, A. R., Jarnagin, M. P., Jr., and Hageman, R. K., "The Preyss-Willes Method in Air to Air Gunnery-Proofs and Computer Evaluation," U. S. Naval Weapons Laboratory Technical Report TN-K-64/73, Dec 1973.

[4]Gilbert, S. W., Preyss, A. E., and Willes, R. E., "Snap-Shoot Gunsight for Fixed-Gun Fighter Aircraft," USAF Academy Technical Report TR-69-3, Dec 1969.

[5]Leatham, A. L., Durrette, J. C., and Alfano, S., "Digital Lead Computing Optical Sight Model," USAF Academy Technical Report, USAFA-TR-74-17, Sept 1974.

2

TABLE 1. AIR FORCE USE OF ANGLE OF ATTACK (CONCLUDED)

Function	Definition	Examples	
7. Approach control	Display optimum approach attitude-speed	F-4C F-105 F-106 F-111	C-141 C-123 C-130 T-137 B-58
8. Rotation and climb out	Display optimum angle of attack for max/best climb out	C-141 C-133 C-130	
9. Pitch-up control	Stick pusher	C-141 F-101	
10. Maximum glide	Display best angle of attack for max C_L/C_D	F-4C B-58 F-104	X-15
11. Engine control	Input to system that controls variable geometry engine inlet	B-70 F-111	
12. Terrain avoidance	Input to terrain avoidance system	F-111	

Continuing Air Force interest in improving the measurement and display of angle of attack is evidenced by numerous Air Force-funded studies[6,7,8] of rather complex and expensive computational methods of deriving angle of attack from other measurements.

In addition to reducing the cost of the instrumentation required to perform the military functions listed, certain additional possibilities arise if the instrumentation is sufficiently inexpensive. It may be possible to reduce the static stability margin of guided expendable munitions by measuring angle of attack and sideslip and integrating this

[6] Dendy, J. B. and Transier, K. G., "Angle of Attack Computation Study," Air Force Flight Dynamics Laboratory Technical Report, AFFDL-TR-69-93, October 1969.

[7] Mellinger, B. L., Kramer, R. M., Griffiths, D. M., et al, "Design Definition Study Universal Stall Margin Indicating System," Aeronautical Systems Division Technical Report, ASD-TR-69-91, December 1969.

[8] Freeman, D. B., "Angle of Attack Computation System," Air Force Flight Dynamics Laboratory Technical Report, AFFDL-TR-73-89, October 1973.

information into the guidance scheme. An example of this use of angle of attack information is provided by the Modular Guided Glide Bomb[9] which now uses a relatively expensive and fragile angle of attack measuring vane.

Using unmanned test items, telemetry, and computerized data reduction schemes it is possible to obtain all the aerodynamic characteristics of a shape without the usual problems of wall effects, turbulence, etc., associated with wind tunnel testing.[10]

Additionally, dynamic phenomena such as spinning of aircraft, coning motion of missiles, and missile flight control system performance are difficult to simulate in the tunnel but relatively easily done with free-fall models. The accurate and low cost air angle measuring scheme described here may contribute significantly to the adequacy of free flight data taking.

Because of the relatively low cost of the new system, it is important to consider what applications now become possible on low-cost aircraft of the type commonly used for flight instruction and in general aviation. The following paragraphs address these potential applications in some detail.

Professional pilots have for many years described aircraft performance in terms of angle of attack because of the fundamental dependence of the major aerodynamic force--namely lift--on this pilot-controlled angle. The Wright Brothers were aware of the importance of knowing and controlling angle of attack as evidenced by a letter from Wilbur or Orville on 11 June 1907 which reads in part, "We can put on a vane to show our angle of incidence is six or seven degrees and climb without any attempt to estimate from looking at the ground." The FAA Flight Instructor Handbook[11] laments the lack of a good indicator by saying, "The angle of attack of a wing in flight is a direct indication of the efficiency with which it is doing its job. Unfortunately, a low priced satisfactory angle of attack indicator is not available for general aviation usage."

----

[9]Webb, J. A., "Static Stability and Control Effectiveness of the MK-84 Modular Guided Glide Bomb II at Transonic Mach Numbers," Arnold Engineering Center Report AEDC-TR-74-58 or Air Force Armament Test Laboratory Report AFATL-TR-74-99, July 1974.

[10]Advisory Group for Aerospace Research and Development, Paris (France), "Methods for Aircraft State and Parameter Identification," N75-29997, May 1975, Meeting held at Hampton, VA, 5-8 Nov 1974.

[11]Department of Transportation, Federal Aviation Administration, Flight Standards Service, "Flight Instructors Handbook," Revised 1969.

4

Experienced pilot and aviation writer, Robert Blodget[12] says, ". . . angle of attack indicators could do more than anything in the history of powered flight to reduce accidents, especially fatals." Another general aviation expert, Peter Garrison,[13] anticipates the use of angle of attack indicators in training pilots by writing, "I also think that students would find the whole approach and landing process easier if they had a real-time display to work from rather than the airspeed indicator. I would like to see the results of exposing students to this kind of instrument; it could be that the ease with which I can fly the airplane by it is really the result of years of experience hidden away in the back of my subconscious and that a student pilot would find the angle of attack indicator just as hard to master as the airspeed; but I doubt it."

How would an angle of attack indicator be used in instructing student pilots? Verbal instructions for take off from the instructor to the student are, "Accelerate to 'x' miles per hour then apply enough back pressure to lift the nose wheel off the runway." or ". . . enough back pressure to assume a normal climb attitude." Great imprecision results from the fact that a new student cannot tell if the nose wheel is on the runway or not, and does not recognize the normal climb attitude. Also, the correct takeoff attitude appears much different in different models of light aircraft due to different cowl shapes, etc. With a good angle of attack indicator the instruction becomes, "Accelerate to 'x' miles per hour, rotate to 'y' degrees angle of attack and let the aircraft fly itself off." No imprecision. No subsequent corrections like, "Your pitch attitude on takeoff is too high." or ". . . too low." These errors will be obvious to the student while doing the maneuver.

The perfect steep turn could be accurately described in terms of angle of attack and bank angle for a given airspeed. During the flight tests of the instrument described herein, the authors flew several steep turns which would have appeared perfect to the most particular FAA examiner. However, the angle of attack indicator revealed every minor bobble. A solo student practicing steep pylon turns and steep eights on pylons would be constantly reminded that such maneuvers are near the limit of light aircraft performance and would be protected from an accidental accelerated stall at low altitude.

The final approach phase of flight seems especially difficult for many students. Most instructors have had the feeling that it would be easy to teach students to land if they could first get a stabilized

---

[12]Blodget, R., "What's It All About, Alpha?" Flying Magazine, November 1971.

[13]Garrison, P., "Angle of Attack Indicator," Flying Magazine, April 1973.

airspeed and pitch attitude on short final. Kohlman and Brainerd[14] have investigated several simplified (one handle) flight path control strategies and concluded that a device which modulated thrust or drag only would be the most effective. Unfortunately the throttle of a light plane not only controls the thrust but also the trimmed angle of attack and corresponding airspeed. Kohlman and Brainerd[14] estimate the trim airspeed is about 10 kt. lower at full power than at idle. Consequently, throttle changes require corresponding elevator changes to avoid exciting the phugoid. The question is "How much must the elevator position or trim be changed to maintain constant C_L?" The angle of attack indicator answers this question exactly. Imagine a student on final at the correct airspeed but above the desired glide slope. The instructor would tell him to reduce power slightly which would reduce the angle of attack and then to correct the angle of attack back to its original value with elevator and trim. This procedure should stabilize the airplane on the desired glide path with little or no phugoid exitation. Some short flight at the reduced angle of attack is used to provide the small "transition arc" to the new glide path. Once on the new glide path, the correct angle of attack is exactly as before.

For the experienced pilot, the angle of attack indicator allows confident and full use of the aircraft capabilities. First, short field obstacle landing approaches would be flown at the same angle of attack at all aircraft weights, thus neatly avoiding the problem of excessive float from a little bit too much speed at the lighter weights. The other side of the same coin is the avoidance of hard touchdown resulting from a slightly slow approach at the heavier weights. Secondly, the maximum range cruise condition for a light aircraft, especially those with constant speed propellers, is a nearly constant angle of attack (corresponding to max C_L/C_D) independent of aircraft weight. One would achieve maximum range at constant altitude (which is more or less dictated by the route structure) by flying the correct angle of attack and gradually reducing the engine speed or manifold pressure as the flight progresses. Third, in climbs, the cruise climb would be flown at the same angle of attack as the max range cruise while the max rate of climb would occur at a higher unique angle of attack (corresponding to max $C_L^{3/2}/C_D$) again independent of aircraft weight. This higher unique angle of attack would also be used for maximum endurance flight as it represents the minimum power requirement for level flight.

Finally, there are three applications of the angle of attack indicator to light business type aircraft that may become practical using the angle of attack indicator described herein. First it may be possible to decrease the pitch static stability margin with resulting reduction in horizontal stabilizer size by using the angle of attack indicator to drive the elevator through a simple stability augmentation system. This

---

[14] Kohlman, D. L. and Brainerd, C. H., "Evaluation of Spoilers for Light Aircraft Flight Path Control," Journal of Aircraft, Vol II, No 8, Aug 1974.

technology is being thoroughly investigated on higher cost aircraft.[15] Lower cost aircraft may follow suit as inexpensive components for the system, such as this angle of attack sensor, become available. Secondly, the ride quality of aircraft with light wing loading could be greatly improved, if one could sense angle of attack changes at the nose of the aircraft in time to modulate wing flaps to maintain constant lift. Since a light twin cruises typically at 300 ft/sec and the tip of the nose is about 10 ft ahead of the wing, an angle of attack sensor with a time constant of less than 0.03 sec is required. The angle of attack sensor described herein can be designed to operate this quickly making a gust alleviation system practical for business aircraft. Thirdly, in the design of general aviation aircraft, the elevator control power required is usually determined by the requirement to achieve maximum lift coefficient with full flaps and forward center of gravity. Consequently the wing can be easily stalled with rearward center of gravity and no flaps.* With a reliable angle of attack sensor one could construct a pitch control system which would cause the max lift coefficient to occur at full back stick in all configurations, thus totally eliminating stall and spin accidents while allowing full use of the aircraft capabilities.

MERITS AND DEFICIENCIES OF EXISTING ANGLE OF ATTACK SYSTEMS

There are currently four types of angle of attack sensors available for use by the Air Force. The null-seeking differential pressure sensor-- for example, part number SLZ9170B manufactured by Automated Specialties Division of Teledyne Incorporated--is currently used on all F-4, F-111 and F-15 type aircraft. The null seeking vane sensor is manufactured by CONRAC Corporation in accordance with MIL-T-25627B and is used on the F-105, T-38, F-5E, C-141 and C-5. The lift transducer sensor manufactured by the Safe Flight Instrument Corporation apparently gives an output which depends on angle of attack over a very narrow range near the stall angle and is used in the T-37, C-123, and A-10. The hemispherical headed probe combined with capacitive pressure transducers manufactured by Rosemount Corp[16] is used on the SR-71, the YF-16, and is being planned for the space shuttle. These four sensors are compared with each other and with the new system proposed herein in Table 2.

---

*The authors are indebted to Bill Fuchs of Piper Aircraft Corporation for communicating this fundamental aircraft design problem.

[15] Yaffee, M. L., "New Controls to Shape Future Aircraft," Aviation Week and Space Technology, October 16, 1972.

[16] Rosemount promotional brochure, "Model 858 Flow Angle Sensors," Bulletin 1014, 1974, Rosemount Inc., Post Office Box 35129, Minneapolis, Minnesota 55435.

TABLE 2. COMPARISON OF ANGLE OF ATTACK SENSORS AND INDICATORS

	Null-Seeking Differential Pressure Sensor	Null-Seeking Vane	Lift Transducer	Hemispherical Headed Probe With Capacitive Pressure Transducers	New Pressure Driven System
Sensitivity to Linear & Angular Accelerations	Insensitive	Sensitive	Insensitive	Insensitive	Insensitive
Ruggedness of External Element	Rugged	Fragile	Fragile	Rugged	Rugged
Response Characteristics	Damped	Too Much Inertia	Adjustable	Adjustable	Adjustable
Small Clearances and Tolerances	Yes	No	No	Yes	No
Likelihood of Foreign Object Damage	High	Low	Low	Low	Low
Calibration	Difficult	Easy	Impossible	Easy	Easy
Cost (Sensor & Cockpit Indicator)	~$2000	~$2000	~$500	~$2100	~$60*
Mean Time Before Failure	437 hr	600 hr	?	10,000** hr	>3000*** hr
Mounting Positions	Fuselage Side Only	Fuselage Side Only	Wing Leading Edge Only	Anywhere	Anywhere
Independent of Other Systems	No	No	No	No	Yes

* Based on cost of simple heated pitot tube and airspeed indicator. No detailed production cost estimate has been made.

** Based on Rosemount promotional literature.

*** Based on abbreviated diaphragm fatigue test described in this report.

8

The characteristics listed for the new pressure driven system have not all been experimentally demonstrated. However, all the claimed characteristics except mean time before failure and cost can be verified by suitable analysis. To this end, a functional description of the pressure driven angle of attack indicating system follows.

PRINCIPLE OF OPERATION OF THE NEW SYSTEM

The pressure driven angle of attack indicating system consists of two major components shown in Figure 1. The probe has no moving parts and measures at least three pressures denoted $p_{\alpha 2}$, P_t, and $p_{\alpha 1}$ for down, center, and upper, respectively. The pressure coefficient meter is divided into three chambers having pressures p_ℓ, p_m and p_r for left, middle and right, respectively. The probe and pressure coefficient meter are operatively connected by three tubes such that, in equilibrium, $p_{\alpha 1} = p_\ell$, $p_t = p_m$ and $p_{\alpha 2} = p_r$. By elementary dimensional analysis, any non-trivial pressure coefficient formed using these three pressures depends only on the angle the probe makes with the stream and the Reynolds number and the Mach number. The pressure coefficient

$$C_\alpha \equiv \frac{p_{\alpha 2} - p_{\alpha 1}}{p_t - \frac{p_{\alpha 2} + p_{\alpha 1}}{2}} = \frac{p_\ell - p_r}{p_m - \frac{p_\ell + p_r}{2}} \tag{1}$$

(Equilibrium Only)

is chosen for our purposes for reasons that will become clear shortly. It will be shown that probes can be selected or designed such that C_α is nearly independent of Mach number and Reynolds number over significant ranges. All that remains is to show that output of the pressure coefficient meter depends only on the pressure coefficient C_α and not on the magnitudes of the individual pressures or pressure differences.

9
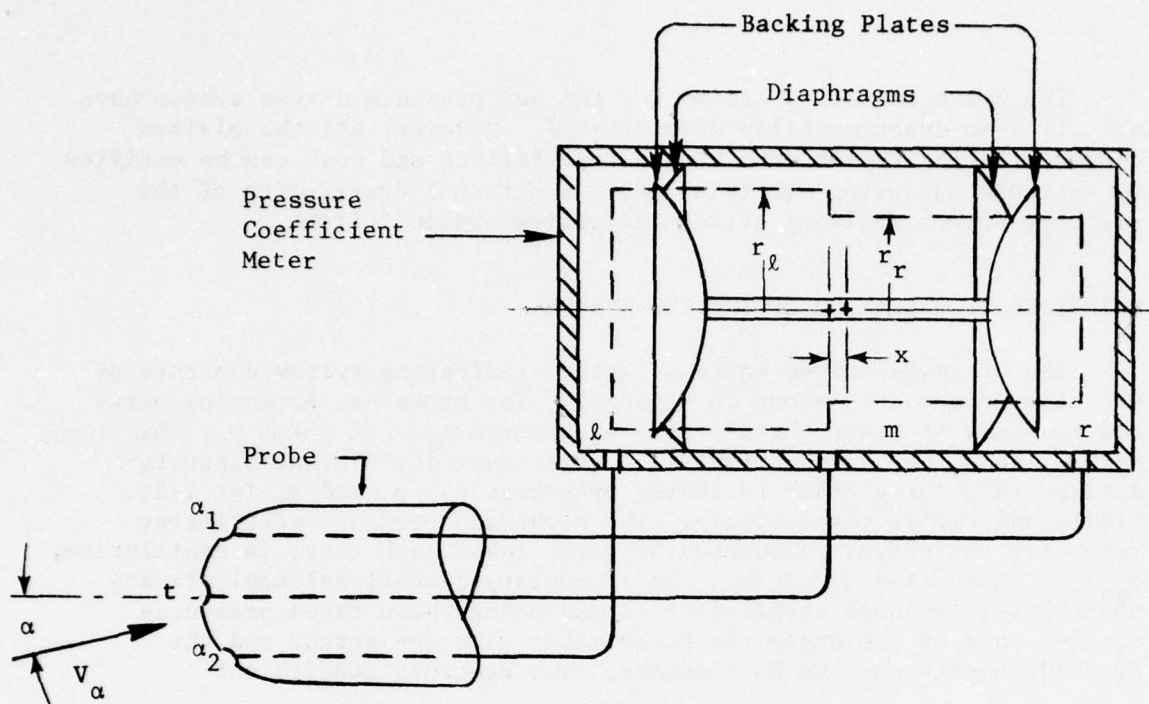
Figure 1. The Pressure Driven Angle of Attack Indicating System

The middle chamber of the pressure coefficient meter is separated from each end chamber by an effectively variable-area mechanism composed of a diaphragm made of very thin but dimensionally stable (not stretchy) material (e.g., Mylar®) and light rigid backing plates (e.g., aluminum). The two backing plates are rigidly connected together to form the backing plate assembly. The pressure in the middle chamber must be higher than the pressure in either end chamber to inflate the diaphragms. The backing plate assembly is supported away from the case by the inflated diaphragms much as a wheel is supported by a tire. The inflated diaphragm is a surface of revolution identical in shape to the backing plate surface. As a backing plate moves toward the center, it simply turns the diaphragm inside-out in the process. As the angle of attack increases, the pressure on the down side of the probe is increased and the pressure on the upper side of the probe is reduced while the pressure at the center port remains nearly unchanged. The increased pressure conveyed to the left chamber and the reduced pressure conveyed to the right chamber clearly encourage the backing plate assembly to move to the right.

Now consider the axisymmetric control volume indicated in Figure 1 by the broken lines. Considering forces along the axis, equilibrium of the control volume requires

$$0 = p_\ell \pi r_\ell^2 - p_r \pi r_r^2 + p_m(\pi r_r^2 - \pi r_\ell^2). \tag{2}$$

10

It is important to notice that the control volume "cuts" the diaphragms exactly in the crease so that the tensile stresses in the diaphragm have no component along the axis. Also, there are no axial forces in the backing plates where they are "cut" by control volume because the backing plates have no loads acting outboard of the crease in the diaphragm. Equation (2) can be rewritten, with some difficulty, in the form

$$C_\alpha = \frac{p_\ell - p_r}{p_m - \dfrac{p_\ell + p_r}{2}} = \frac{2(r_\ell^2 - r_r^2)}{r_\ell^2 + r_r^2} . \tag{3}$$

Since r_ℓ and r_r are simply kinematic functions of the position of the backing plate assembly, say x, and for the equilibrium condition Equation (1) and (3) together may be written functionally

$$C_\alpha = f(x) . \tag{4}$$

Therefore, the position of the backing plate assembly depends only on C_α and not individually on the pressures forming C_α. The form of the function appearing in Equation (4) depends upon the shape of the diaphragms and matching backing plates. Depending on the application, a mechanical linkage is added to indicate the position of the backing plate assembly to the pilot, or, an electrical position sensor such as a variable resistance variable differential transformer may be added to provide an electrical input for flight control or fire control.

With the operating principle of the pressure driven angle of attack indicating system in mind, some of the features listed in Table 2 can be supported. The external element is as rugged as the ordinary pitot tube. Obviously there are no small clearances. Small foreign objects inhaled will fall harmlessly to the bottom of the case. Calibration of the aircraft could be easily verified by applying known pressures at probe sensing ports. Since the probe and indicator are no more complicated than the corresponding parts of a simple airspeed indicator, one would expect the production costs to be about the same. Clearly there is great flexibility in the mounting position of both probe and indicator. Also, the system is totally independent of all other aircraft systems and will continue to operate after complete electrical, pitot-static, and vacuum system failures.

HISTORICAL DEVELOPMENT SEQUENCE

Early in 1972 we became aware of the need for an accurate, rugged, reliable, and inexpensive angle of attack indicator. A device similar to the common pressure driven airspeed indicator was envisioned and we set out quite deliberately to produce such a device. Our first thought was to use the position of the stagnation point near the leading edge of the wing to derive the angle of attack. The "Safe Flight" stall

11

warner uses this principle. It has a small metal tab protruding from
the lower curvature of the leading edge. With increased angle of attack
and as the stagnation point moves from above to below the tab, the
loading on the tab changes from a down load to an up load closing a
switch which turns on the stall warning horn in the cockpit. We wanted
to use the same principle to indicate a range of stagnation point positions
and corresponding range of angle of attack. A rotary angle of attack in-
dicator, diagrammed in Figure 2, using movement of the stagnation point
around the wing leading edge to activate a remote indicator was designed
and built. Careful examination of Figure 2 reveals that the rotor of the
indicating instrument is only in equilibrium when the two ports being
sensed are at equal pressures which, in turn, implies that the stagnation
point is between the two ports. Also, if the rotor is not in the equi-
librium position, the resulting pressure difference tends to drive the
rotor to the equilibrium position. Duncan Keirnes, who was then a cadet
at the Air Force Academy, connected the device to a large cylinder (to
simulate the wing leading edge), and tested it in the subsonic wind
tunnel. The rotary angle of attack indicator worked, but was easily
rendered inoperative by small pieces of dirt working their way into the
necessarily narrow mechanical clearances. Also the movement was quite
slow due to inertia of the rotor and viscosity of the air. The requirement
for a large number of pressure sensing ports and tubes was an obvious
disadvantage.
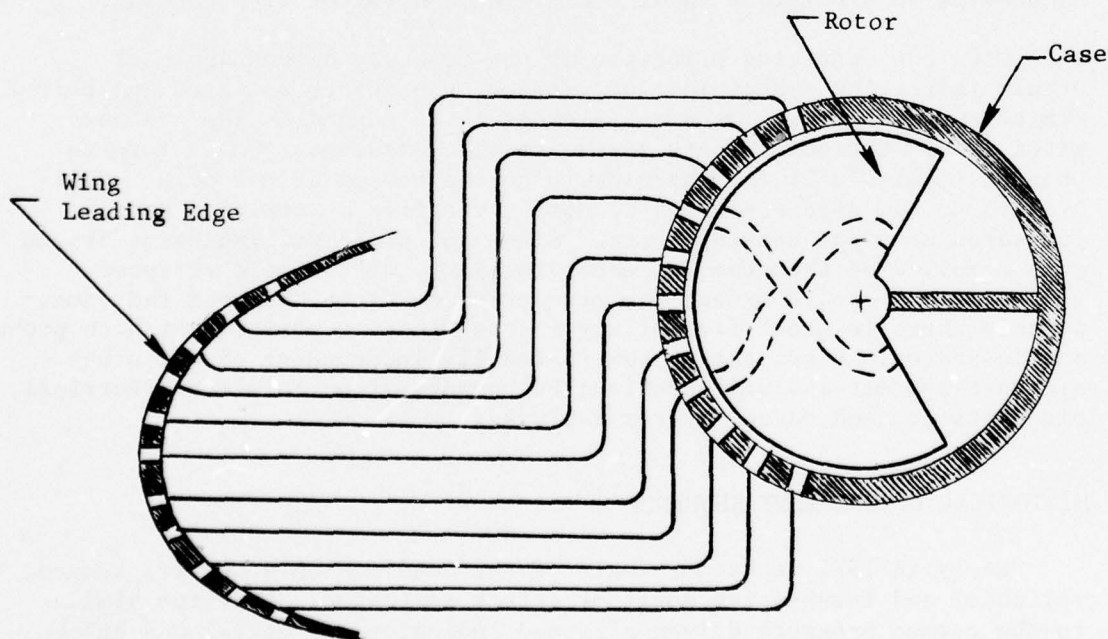
Figure 2. The Rotary Angle of Attack Indicator

12

Another Academy cadet, Steven Marinella, asked a most relevant question, "What is the minimum number of pressure measurements made on the aircraft necessary to infer the angle of attack?" The correct answer, as discussed before, is three. The idea of determining angle of attack from pressure measured on the wing is quite old.[17] Rettie[18] investigated this concept both theoretically and experimentally and suggested determining angle of attack from the difference between two pressures measured on the upper side of the wing divided by the dynamic pressure measured by the pitot-static system of the aircraft. Marinella experimentally investigated the pressure distribution around the nose of a NACA 65_3-418 airfoil in detail to assess the possibility of using this pressure distribution, which varies rapidly with angle of attack, to drive an indicator.

Marinella located a point on the top surface of the wing just behind the leading edge where the pressure coefficient varies strongly and uniformly with angle of attack over the useful angle of attack range of the section. A summary of this small part of Marinella's data is reproduced in Figure 3.
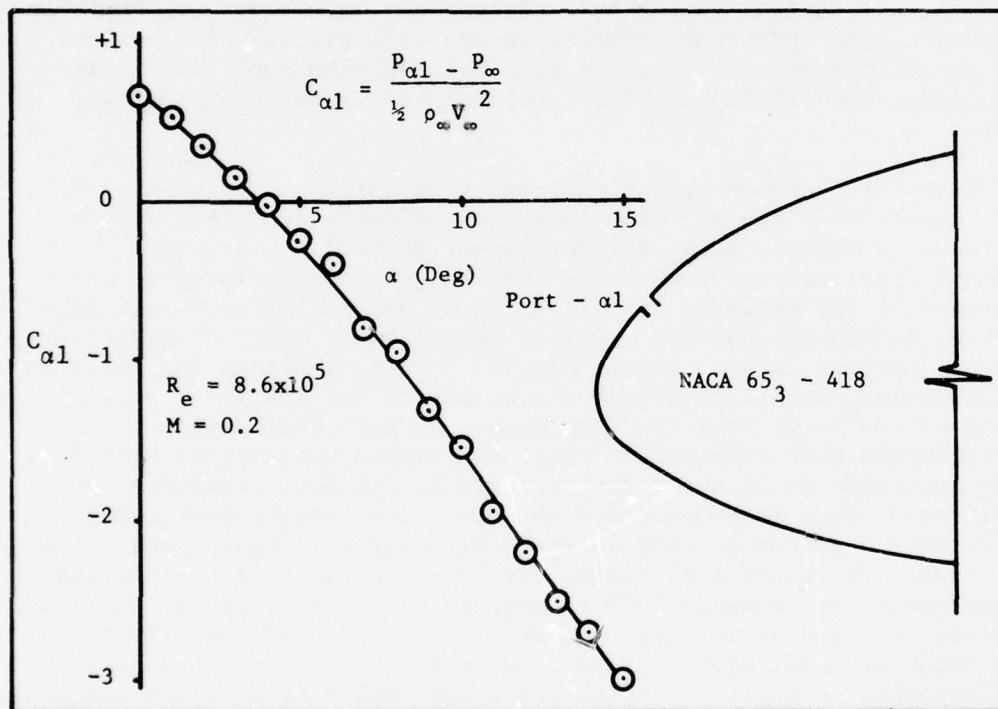
Figure 3. Pressure Coefficient Variation on Upper Surface of Wing

[17] Pringle, G. E., "Stall Warning Devices," A.R.C. 5049, 1941.

[18] Rettie, I. H., "An Investigation of the Velocity Distribution Around the Nose of the Aerofoil with a Flap," Reports and Memoranda No. 3027, May 1955.

13

The author conceived the force balance type of indicator shown in Figure 4. As the angle of attack of the aircraft is increased, the pressure under the right ball is reduced displaying the needle to the right. That the output of this instrument depends only on the pressure coefficient measured on the wing (which, in turn, depends only on the angle of attack for a given section) can easily be shown by taking the sum of the moments about the shaft. If we take the length, ℓ, to be very long compared to the length, r, equilibrium of the needle shaft requires

$$(p_o - p_\infty) A \sin (\theta + \delta) \ r = (p_\infty - p_{\alpha_1}) A \sin (\theta - \delta) \ r$$

$$\frac{p_o - p_{\alpha 1}}{p_o - p_\infty} = \frac{\sin (\theta + \delta)}{\sin (\theta - \delta)}$$

$$1 - C_{\alpha 1} = f (\delta) \ .$$

Thus, the output, δ, depends only on the pressure coefficient $C_{\alpha 1}$. The small clearances required in the ball pistons are an obvious disadvantage of the balance type indicator. Replacing the ball pistons with bellows would be an improvement if one could find bellows with small intrinsic spring constant and friction. These problems led us in three separate directions.

An attempt to develop spring constant free bellows eventually led to the very successful diaphragm type instrument already described. In an attempt to use available metal bellows, Steve Marinella proposed a displacement type instrument in which the two pressure differences cause displacements of two bellows, one displacement being divided by the other in a mechanical linkage and the quotient displacement being displayed as the output. Another Academy cadet, Michael Larson, designed and built an electrical analog circuit to divide the output of one low level pressure transducer by another. Pressure transducers by Ball Engineering of Boulder, Colorado were selected as they have proven accurate in sensitive sailplane instrumentation where the pressure differences are quite low. The displacement type instrument and the electrical analog device may warrant further development because their ultimate performance and price are not known. The electrical analog device using the Ball Engineering transducer would cost roughly $300 to manufacture. In series production the displacement type device might be about twice that of a vertical velocity meter or about $150. In passing, it is interesting to note that Schuck[19] patented an angle of attack indicator employing an electromechanical device to perform the required division.

---

[19] Schuck, O. H., "Angle of Attack Indicating Device," U. S. Patent No. 2,948,149, Aug 9, 1960.

14
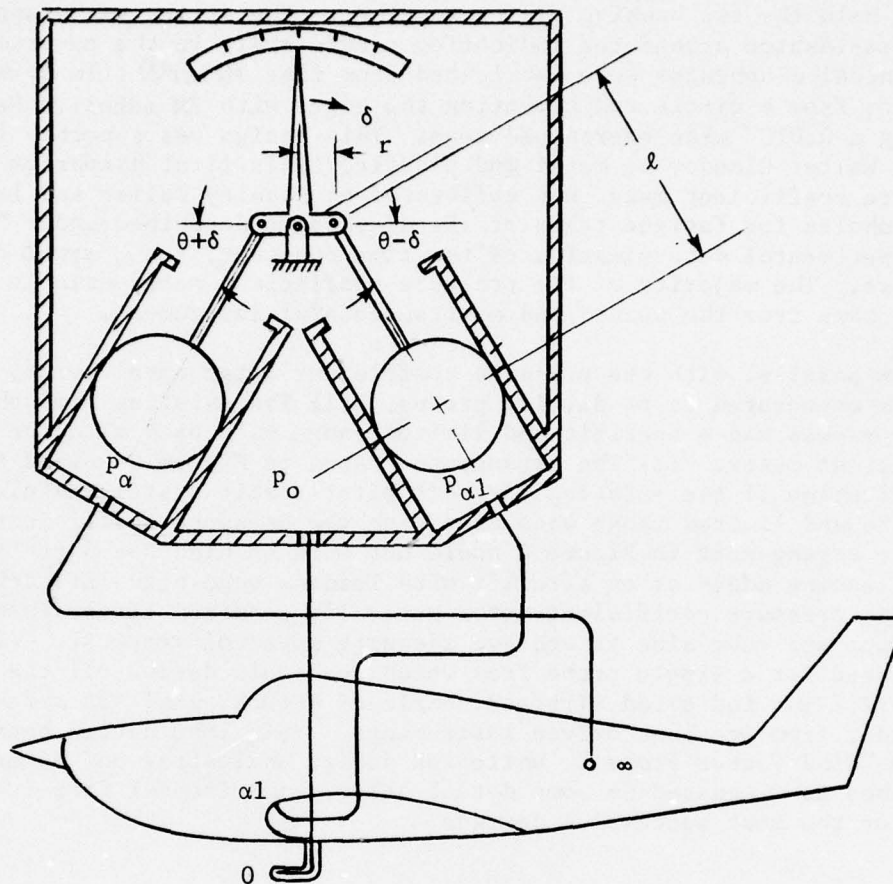
Figure 4. Balance Type Angle of Attack Indicator

Of the possibilities we were most highly motivated to develop the balance type, which later evolved into the diaphragm type, because of its relative simplicity in concept. Consider the following. The balance divides the two pressure differences directly resulting in a displacement which can be displayed. The displacement instrument converts the two pressure differences into displacements, then divides one displacement by the other mechanically to arrive at a quotient displacement which is displayed. The electrical device converts the two pressure differences into displacements then into voltages in the transducers. One voltage is divided by the other in the analog circuit, and the resulting quotient voltage is converted by a meter to a displacement for display. The balance type and diaphragm type can boast "Honest Weight-No Springs." It is really a balance as opposed to a scale.

15

In the first diaphragm type pressure coefficient meter design a string held the two backing plates together. The string was wrapped windlass-fashion around the indicating needle shaft in the central chamber. The conical diaphragms were fabricated from flat Mylar® film by cutting a sector from a circle and cementing the edges with 3M adhesive No. 4693 forming a 0.010" wide overlapped seam. This design was superbly produced by Mr. Walter Glander in metal and plastic. This first diaphragm type pressure coefficient meter was calibrated by Stanley Fuller and later used by Reinholtz for fatigue tests of the diaphragms described under "Testing" and experimental determination of the time constant, i.e., speed of response. The majority of the pressure coefficient meter data in this report came from the second and most successful instrument.

In parallel with the pressure coefficient meter development, several factors encouraged us to develop probes. (1) The existing hemispherical headed probes had a specific and limited range when used with the pressure coefficient meter. (2) The arrangement shown in Figure 4 voided the certification of the existing aircraft pitot-static system and also had a specific and limited range when used with the pressure coefficient meter. (3) The arrangement in Figure 4 would not work on high speed craft with sharp leading edges or on aircraft with leading edge high lift devices. (4) The pressure coefficient meter generally requires larger than common port size and tube size to achieve adequate speed of response. (5) There was a need for a single probe from which one could derive all the common air data, i.e., indicated airspeed, angle of attack, angle of sideslip and altitude, from pressure driven instruments. This last device became known as the "Wind Vector Probe." While the design philosophy and literature on probes is discussed in some detail below, experimental data is presented only for the most successful designs.

16

SECTION II

DESIGN

Design considerations for the two major system components, namely the probe and the pressure coefficient meter, are discussed in turn. Then the interfacing of the probe with the meter followed by the interfacing of the whole pressure driven angle of attack indicating system with the aircraft are addressed.

PROBE DESIGN CONSIDERATIONS

The function of the probe is to sense three pressures for each air angle to be measured. If a single probe has provisions for measuring angle of attack, angle of sideslip, and total and static pressure (to infer airspeed and altitude) the resulting device is called a "wind vector probe." Beecham & Collins[20] provide a complete calibration for a hemispherical headed wind vector probe for supersonic speeds. The Rosemount Corp. markets such a device. Figure 5 shows how outputs from a wind vector probe would be used to drive instruments to indicate angle of attack, angle of sideslip, indicated airspeed and altitude. For many applications the full system is not needed. For example, existing aircraft may already have carefully located static pressure ports and these would not be required on the probe. Or, the application may require only part of the complete system. Spherical and hemispherical probes for measuring angles only have been studied extensively.[21,22,23,24,25,26]

---

[20]Beecham, L. J. and Collins, S. J., "Static and Dynamic Response of a Design of a Differential Pressure Yawmeter at Supersonic Speeds," RAE Report No. GW 19, February 1954.

[21]Dean, R. C., Jr., "Aerodynamic Measurements," The MIT Press, 1953, (Chapter VI - Flow Direction Measurements).

[22]Hutton, P. G., "Static Response of a Hemispherical-Headed Yawmeter at High Subsonic and Transonic Speeds," RAE Technical Note No. Aero 2525, CP No. 401, Aug 1957.

[23]Rogal, B., "Differential Pressure Measurements in Sensing Sideslip and Angle of Attack," Flight Test Instumentation Proceedings of the Third International Symposium - 1964, Vol 3, M. A. Perry, ed., Pergamon Press, 1965, pp 1-22.

[24]Nowack, C. F. R., "Improved Calibration Method for a Five-Hole Spherical Pitot Probe," Journal of Physics, Part E - Journal of Scientific Instruments, Vol. 3, Jan 1970.

[25]Wright, M. A., "The Evaluation of a Simplified Form of Presentation for a Five-Hole Spherical and Hemispherical Pitometer Calibration Data," Journal of Physics, Part E - Journal of Scientific Instruments, Vol 3, May 1970.

The hemispherical or spherical headed probe, when used in conjunction with the diaphragm type pressure coefficient meter to indicate an angle, has several limitations which can be overcome by thoughtful probe design. If the angle of attack or angle of sideslip becomes so large (about $\pm 22\frac{1}{2}°$) that equal pressures occur at the total pressure port (T) and one of the angle measuring ports (α_1, α_2, β_1 or β_2), the corresponding diaphragm of a pressure coefficient meter will have no supporting pressure difference to keep it properly inflated. The ends of the useful range are also identified by $C_\alpha = \pm 2$ as can be verified by substituting $p_m = p_\ell$ and $p_m = p_r$ in turn into Equation (3). The details of this problem are discussed under "Probe and Pressure Coefficient Meter Interfacing" below, but it is sufficient for the present purpose to realize that the hemispherical headed probe has a definite useful angle range when used with the diaphragm type pressure coefficient meter. Certain applications require very accurate angle measurement over narrow ranges. One example was the F-106 test bed for the snap shoot gunsight where sideslip angles were limited to ± 2 degrees by the aircraft configuration. Another example might be an aircraft angle of attack application where the extremes of the desired angular range are defined by maximum C_L/C_D (corresponding to maximum range for propeller aircraft) and maximum $C_L^{3/2}/C_D$ (corresponding to maximum endurance for propeller aircraft). The section angle of attack range for this last example is typically $3°-4°$. To achieve great sensitivity
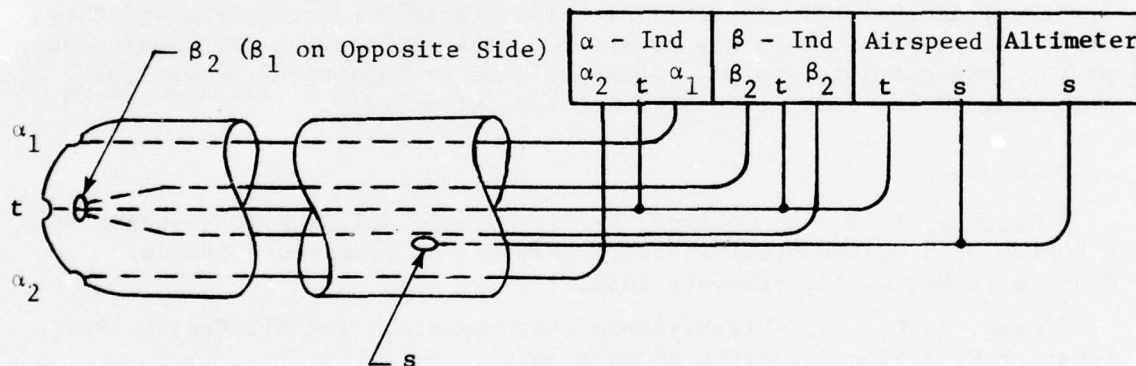
Figure 5. A Complete Wind Vector Probe and Pressure Driven Indicators

and accuracy at the expense of reduced angular range one can use the two-dimensional flow around a wing or fin leading edge. Other applications, such as expendable munitions and low aspect ratio aircraft, require operation over larger angle of attack ranges than can be indicated with the hemispherical headed probe and diaphragm type pressure coefficient meter. For these other applications, bodies of revolution such as cone-sphere-cylinders, ogives, and ellipsoids are less sensitive and can

[26] Armistead, K. H. and Webb, L. D., "Flight Calibration of a Nose-Boom-Mounted Fixed Hemispherical Flow-Direction Sensor," NASA TN D-7461, October 1973.

operate over a larger angular range than hemisphere headed probe. For example, Dau, McLeod, and Surrey[27] have investigated an ellipsoid tipped probe. Strakes or wings may be added to increase the sensitivity of certain probes.

The diaphragm type pressure coefficient meter inhales and exhales air while moving and the probe must, therefore, have considerably larger ports and internal tubing than is typical in pitot static systems to assure adequate speed of response. Probes made of tubes and having very large ports and flow areas as in Figure 6 have been built and calibrated.[28],[29],[30]
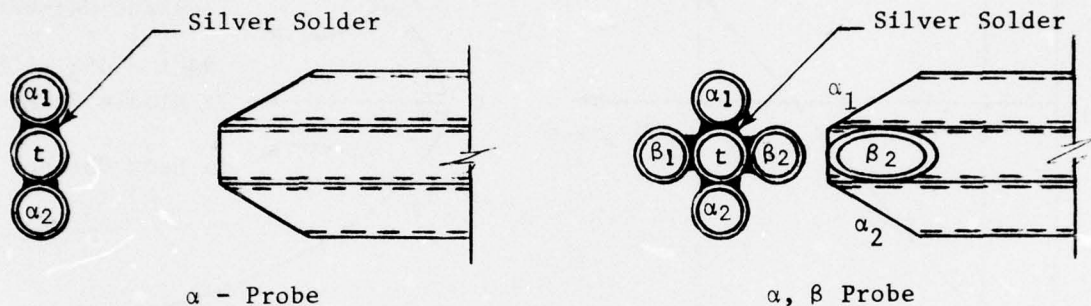
Figure 6.   Flow Angle Measuring Probes Assembled from Tubing

Two Dimensional Wing Leading Edge--The pressure distribution around the leading edge of a wing is very sensitive to the angle of attack. This phenomena may be used with the diaphragm type pressure coefficient meter to indicate angle of attack very accurately over a small angular range. Figure 7 presents a small amount of the data taken by Steve Marinella on the pressure distribution around the nose of a NACA 65_3-418 airfoil. If a diaphragm type pressure coefficient meter was attached as shown, the right diaphragm would collapse at about 0° and the left diaphragm would collapse at about 7°. Therefore, we suppose that $1^o < \alpha < 5^o$ to be a suitable range. Over this range, the sensitivity of

[27] Dau, K., McLeod, M., and Surrey, D., "The Probes for the Measurement of the Complete Velocity Vector in Subsonic Flow," Aeronautical Journal, Vol 72, December 1969.

[28] Bryer, D. W., Walshe, D. E., and Garver, H. C., "Pressure Probe Selected for Three Dimensional Flow Measurements," ARC R&M 3037, 1958.

[29] Dudzinski, T. J. and Krause, L. N., "Flow Direction Measurements With Fixed-Position Probes in Subsonic Flow Over a Range of Reynolds Numbers," NASA TM X 1904, N69 40059, 1969.

[30] Rojaratnam, N. and Muralidhar, D., "Yaw Probe Used as Preston Tube," Aeronautical Journal, Vol 72, A69 16396, Dec 1969.

the wing leading edge used on a probe is about $\partial C_\alpha / \partial \alpha = 0.4/\text{deg}$ or about five times the corresponding value for the hemisphere headed probe.
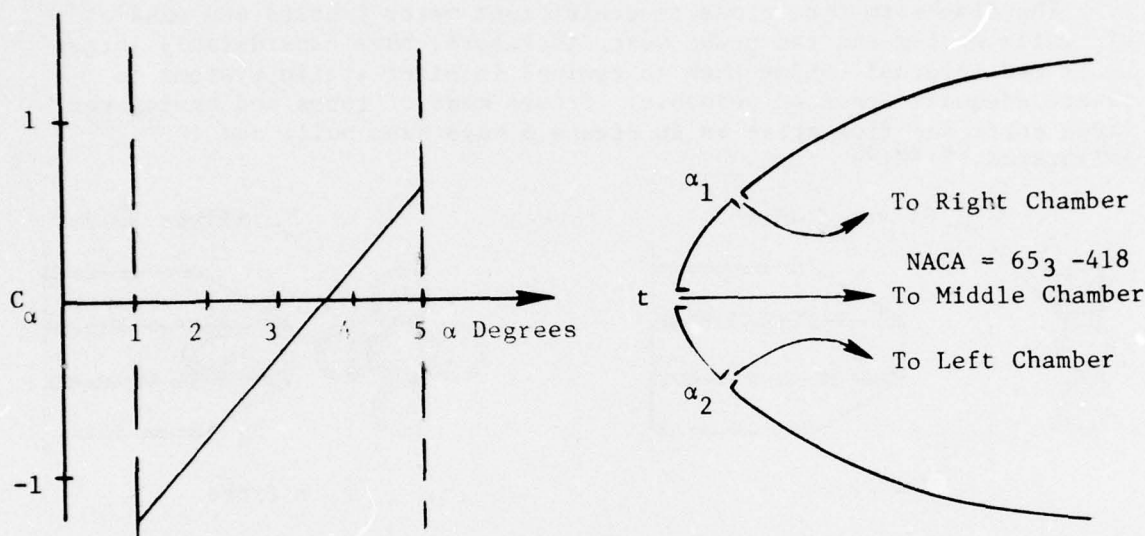
Figure 7. Wing Leading Edge Used as Angle of Attack Probe

Apparently the sensitivity can be increased and the range narrowed to any degree required by using thinner wing sections or by moving the down-side and upperside ports closer to the center port. However, moving the ports closer together reduces the pressure difference across the diaphragms which is undesirable in low speed applications. The angular range can be extended by connecting the middle chamber to the aircraft total pressure source, the left chamber to the aircraft static pressure source, and the right chamber to the upper port on the wing leading edge exactly as shown for the balance type instrument in Figure 4. This apparently very practical arrangement requires either enlarging the existing aircraft pitot static system or paralleling the existing pitot static systems with a separate system to drive the angle of attack indicator. Current FAA and military regulations prohibit modifying in any way existing certified pitot static systems. For these reasons we have considered various self-contained probes. If angle of attack indicators become as reliable and common as airspeed indicators, then it may be possible to do away with the external probe and certify the combined pitot static and angle of attack system. Then, the only external change necessary is a single static pressure port on the upper surface of the wing near the leading edge.

20

Bodies of Revolution--Probes with greater angular range than the hemisphere with 45° off centerline angle measuring ports can be designed by moving the angle measuring ports farther from the center port and by using more slender nose shapes such as cones, ogives, or elipsoids. The logical extreme of this strategy leads to a pitot tube with the angle measuring ports far back on the cylindrical surface. According to slender body theory,[31] such a probe would have zero sensitivity at small angles. However, at higher angles of attack vorticity will be shed and a pressure difference will develop between the upper and lower surfaces. Therefore, the calibration curve of such a probe is likely to be quite nonlinear. To reduce these difficulties one could move the angle sensing ports just ahead of the cylindrical portion. It was this rationale that led to the family of probes illustrated in Figure 8. This family of probes will be calibrated at the Arnold Engineering Development Center during June 1975. It is hoped that from this family one will be able to select a probe for nearly any required range and sensitivity.

$$\ell = \frac{0.375 \, \text{Cos} \, \theta_n - 0.090}{\text{Tan} \, \theta} + 0.375 \, \text{Sin} \, \theta_n$$

Note: All Ports 0.150 Diameter

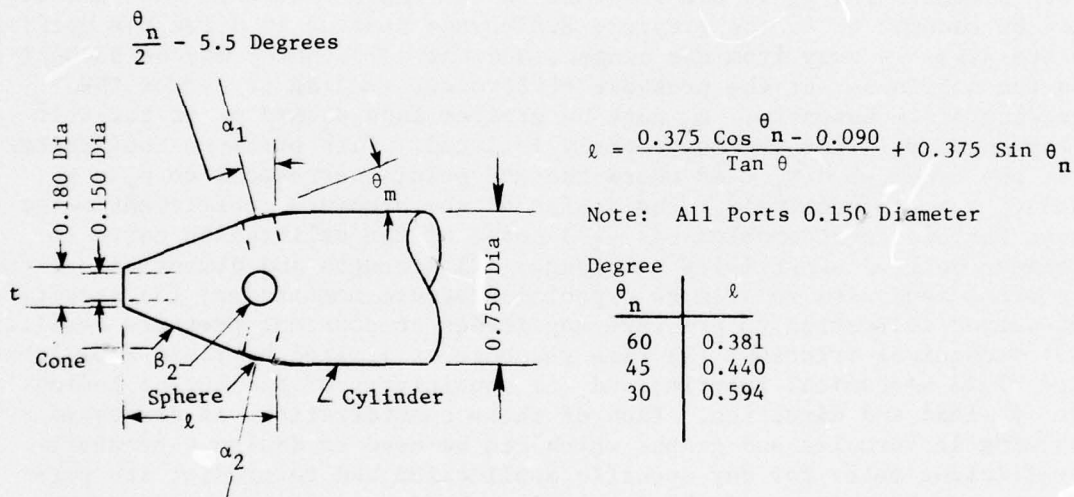| Degree θ_n	ℓ
60	0.381
45	0.440
30	0.594

Figure 8. A Family of Probes

[31]Liepmann, H. W. and Roshko, A., "Elements of Gasdynamics," John Wiley & Sons, 1957.

21

Strakes and Wings--To enhance the sensitivity of a probe at low angles, one can add strakes or wings. The idea here is to begin generating circulation and shedding vorticity at low angles with resultant increase in pressure on the lower side and reduction in pressure on the upper side. The only functional difference between strakes and wings is that wings shed vorticity mainly along their trailing edges whereas strakes shed vorticity mainly along their side, or leading edges. The probe illustrated in Figure 9 has been designed using wings and its calibration curves are presented in the section titled "Testing."

PRESSURE COEFFICIENT METER DESIGN

The indicating instrument is provided with three pressures. The output is intended to depend only on the pressure coefficient

$$C_\alpha = \frac{p_\ell - p_r}{p_m - \frac{p_r + p_\ell}{2}} \tag{3}$$

where p_m is the pressure in the middle chamber, p_ℓ is the pressure in the left chamber, and p_r is the pressure in the right chamber. The numerator may be thought of as the pressure difference tending to drive the backing plate assembly away from the center, and the denominator may be thought of as the stiffness, or the pressure difference, tending to center the backing plate assembly. p_m must be greater than p_ℓ and p_r or the thin diaphragms will not remain properly inflated. This pressure coefficient has the range $-2 < C_p < +2$ where the end points correspond to $p_r = p_m$ and $p_\ell = p_m$, respectively. The design of the pressure coefficient meter must include consideration of: (1) shape of the calibration curve to achieve desired sensitivity and range; (2) strength and dimensions of the internal mechanism related to expected pressure magnitudes; (3) sensitivity of output indication to pressure magnitudes at constant pressure coefficient; (4) mechanical friction; (5) time response as limited by fluid flow losses and fluid mechanical inertia; and (6) sensitivity of the output indication to g load and direction. Each of these considerations is discussed resulting in formulas and graphs which can be used to design a pressure coefficient meter for any specific application and to predict its performance. Resistance of the internal mechanism to movement due to the flexing of the diaphragms and sensitivity of the output to temperature changes are logical topics for future study.

Derivation of Theoretical Calibration Curves--The shape of the calibration curve $x = f(C_\alpha)$ where x is the displacement of the backing plate assembly can be controlled to some extent by selecting the shapes of the diaphragms and backing plates appropriately. The shapes of the diaphragms and their matching backing plates can be arbitrary surfaces of revolution consistent with the requirement that the thin diaphragms have a stable inflated shape. Consequently, considerable variation in the shape of the calibration curve is possible. Initially, some effort was made to select

22

diaphragm and corresponding backing plate shapes so that output, x, would be linear with the input, C_α. However, since the output of the probe, C_α, is rarely linear with the flow angle, the probe and pressure coefficient meter must be considered together.

There are three families of shapes which are of particular interest. Cones are developable shapes and may be fabricated from flat material although, we have not found this to be the best procedure. Spherical shapes are easily formed or turned and result in uniform bi-axial stress in the thin diaphragms. Paraboloids result in a linear calibration curve. These three shapes, to be discussed here, by no means exhaust the possibilities. Different shapes could be used on the left and right sides.

Now, if one supposes diaphragms and matching backing plates to be cones and with reference to Figure 10

$$\frac{dr_\ell}{dx} = \frac{1}{2 \tan \theta_\ell} \quad \text{and} \quad \frac{dr_r}{dx} = \frac{-1}{2 \tan \theta_r}$$

$$r_\ell = R + \frac{x}{2 \tan \theta_\ell} \quad \text{and} \quad r_r = R - \frac{x}{2 \tan \theta_r}$$

where R is the radius of the crease at $C_\alpha = 0$ and $r_\ell = r_r$.

To reduce the amount of notation, let the average slope of the cones be defined by

$$(\tan \theta)_m = \frac{\tan \theta_\ell + \tan \theta_r}{2} .$$

And let

$$a = \frac{\tan \theta_r}{(\tan \theta)_m} , \quad b = \frac{\tan \theta_\ell}{(\tan \theta)_m}$$

and

$$\bar{x} = \frac{x}{2R (\tan \theta_m)} .$$

The equation for C_α as a function of $\bar{x}$ becomes

$$C_\alpha = 2 \; \frac{(1 + \frac{\bar{x}}{b})^2 - (1 - \frac{\bar{x}}{a})^2}{(1 + \frac{\bar{x}}{b})^2 + (1 - \frac{\bar{x}}{a})^2} \tag{5a}$$

where a and b must satisfy $a + b = 2$. $\tag{5b}$

Theoretical calibration curves for $a = b = 1$ (i.e., identical conical left and right diaphragm and backing plate assemblies) and for $a = 1.5$, $b = 0.5$ (i.e., for a flatter cone on the left side) are presented in Figure 11. One must recall that the displacement, x, is made dimensionless with

23

2R $(\tan \theta)_m$ to form $\bar{x}$. Thus, larger displacements are caused by increasing either the size of instrument, R, or the average slope of the cones, $(\tan \theta)_m$.
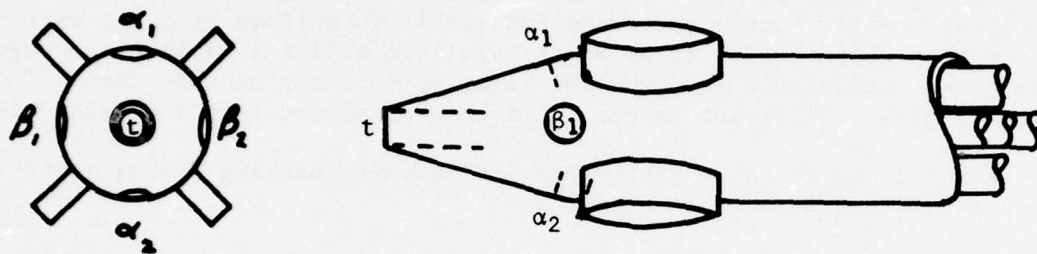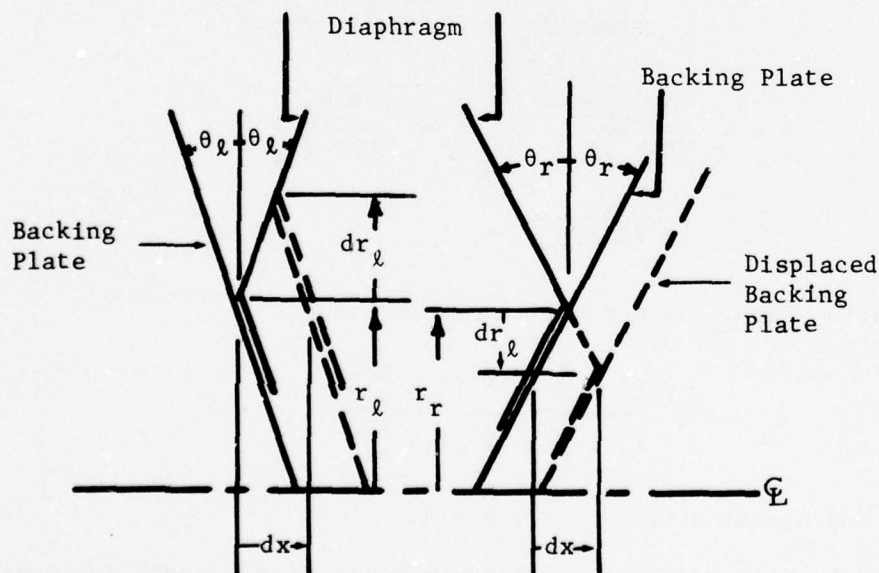

Figure 9. A Probe Utilizing Wings

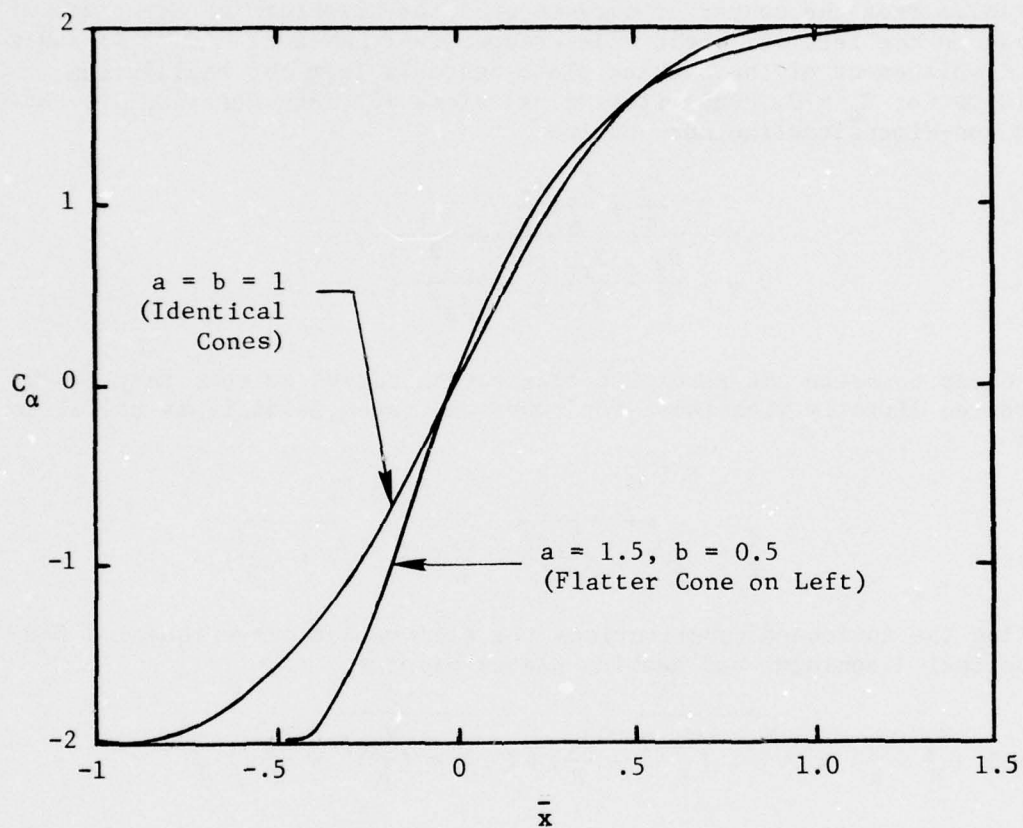Figure 10. Kinematics of Conical Diaphragms and Backing Plates

24

Figure 11. Calibration Curves for Conical Diaphragms and Backing Plates

The kinematics of the spherically shaped diaphragms and backing plates illustrated in Figure 12 requires

$$r_\ell^2 = \rho_\ell^2 - (y_\ell - \frac{x}{2})^2 \quad \text{and} \quad r_r^2 = \rho_r^2 - (y_r + \frac{x}{2})^2 \qquad (6)$$

where ρ_ℓ and ρ_r are the radii of curvature of the spherical diaphragms and backing plates on the left and right sides, respectively; y_ℓ and y_r are the distances from the center of curvature of the diaphragm to the plane of the crease on the left and right sides, respectively, when $r_\ell = r_r = R$; and x is the displacement of the backing plate assembly from the equilibrium position for $C_\alpha = 0$. Substituting relations (6) into Equation (3) and using R to non-dimensionalize, one obtains

$$C_\alpha = \frac{2 \left(\frac{y_\ell}{R} + \frac{y_r}{R}\right) \frac{x}{R}}{2 + \left(\frac{y_\ell}{R} - \frac{y_r}{R}\right) \frac{x}{R} - \frac{x^2}{2R^2}} \quad .$$

In order to scale the resulting calibration curves so that they can be compared directly with those for cones and paraboloids, it is useful to let

$$\bar{x} = \frac{x}{d}$$

where

$$\frac{d}{R} = \left(\sqrt{1 + \left(\frac{y_r}{R}\right)^2} - \frac{y_r}{R}\right) + \left(\sqrt{1 + \left(\frac{y_\ell}{R}\right)^2} - \frac{y_\ell}{R}\right)$$

Making the indicated substitutions the calibration curve equation for spherical diaphragms and backing plates becomes

$$C_\alpha = 2 \left(\frac{y_\ell}{R} + \frac{y_r}{R}\right) \bar{x} \left[\sqrt{1 + \left(\frac{y_r}{R}\right)^2} - \frac{y_r}{R}\right) + \left(\sqrt{1 + \left(\frac{y_\ell}{R}\right)^2} - \frac{y_\ell}{R}\right) \right] \Bigg/$$

$$\left\{ 2 + \left(\frac{y_\ell}{R} - \frac{y_r}{R}\right) \bar{x} \left[\left(\sqrt{1 + \left(\frac{y_r}{R}\right)^2} - \frac{y_r}{R}\right) + \left(\sqrt{1 + \left(\frac{y_\ell}{R}\right)^2} - \frac{y_\ell}{R}\right)\right] \right.$$

$$\left. - \frac{\bar{x}^2}{2} \left[\left(\sqrt{1 + \left(\frac{y_r}{R}\right)^2} - \frac{y_r}{R}\right) + \left(\sqrt{1 + \left(\frac{y_\ell}{R}\right)^2} - \frac{y_\ell}{R}\right) \right]^2 \right\} \qquad (7)$$

Figure 13 gives the calibration curve from Equation (7) for $y_\ell/R = y_r/R = \sqrt{3}$ corresponding to left and right diaphragms and backing plates having equal radii and for a case of unequal radii. As y_ℓ/R and y_r/R become larger, the calibration curve becomes more nearly linear. This is because a paraboloid gives an exactly linear calibration curve and for the very flat diaphragms the sphere and paraboloid are nearly the same.

26
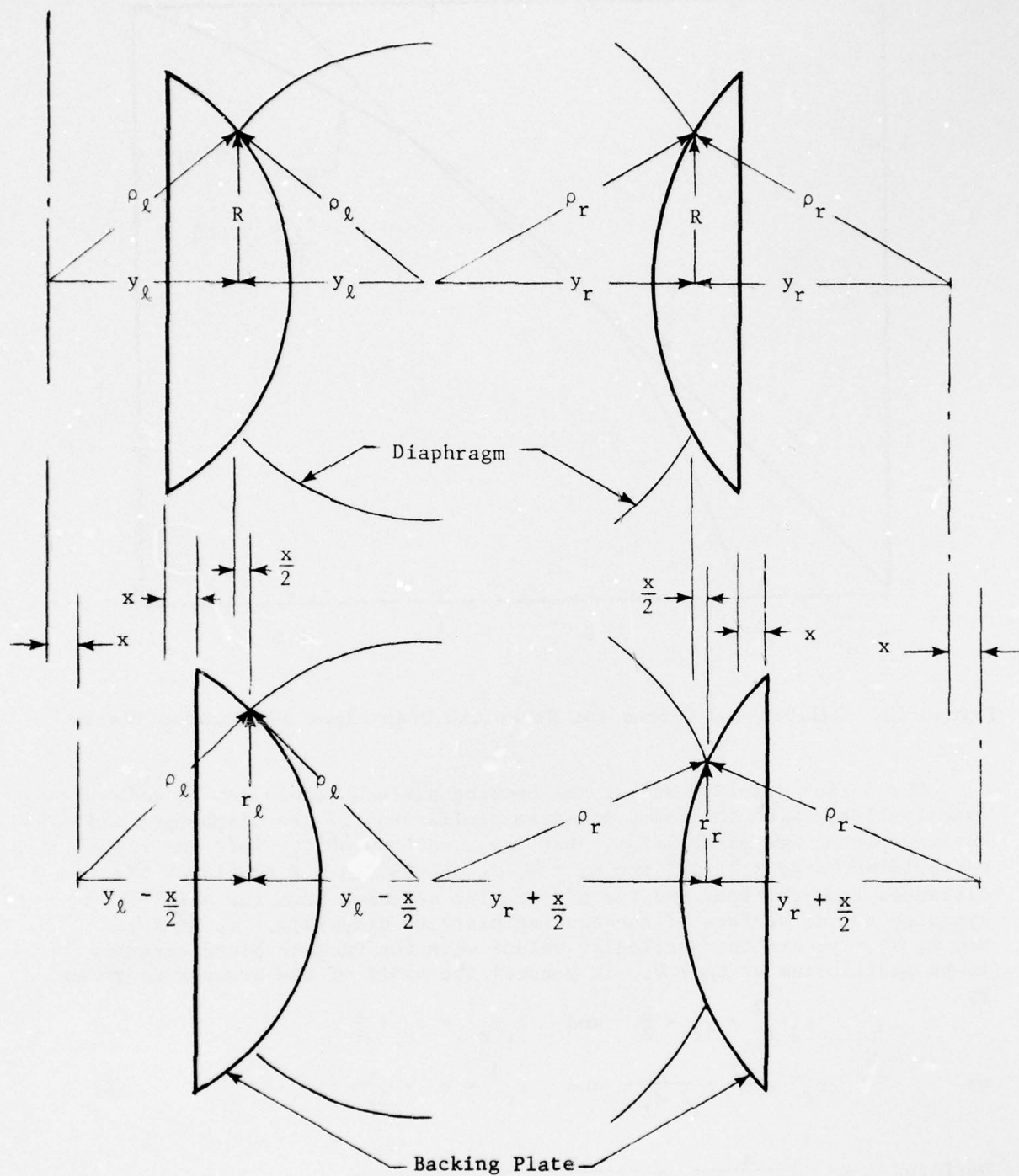
Figure 12. Kinematics of Spherical Diaphragms

27
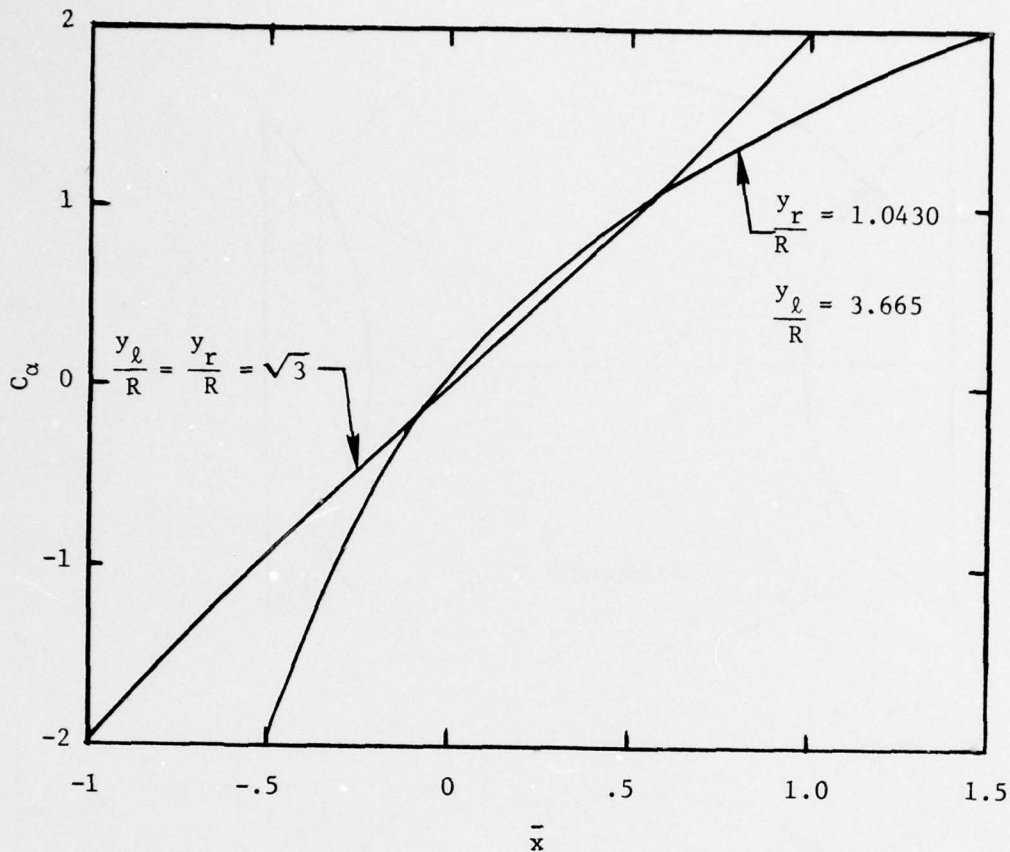
Figure 13. Calibration Curves for Spherical Diaphragms and Backing Plates

The output displacement of the backing plate assembly can be made exactly linear with the input pressure coefficient if the diaphragms and backing plates are paraboloids. Let the equations of the left and right paraboloids be $z_\ell = k_\ell \rho_\ell^2$ and $z_r = k_r \rho_r^2$ where the z's represent the distances from the apex and the ρ's are the distance from the axis of symmetry to the surface of the backing plate or diaphragm. $k_r R^2 = y_r$ and $k_\ell R^2 = y_\ell$ are the particular values when the backing plate assembly is in equilibrium at $C_\alpha = 0$. In general, the radii of the creases is given by

$$k_\ell r_\ell^2 = y_r - \frac{x}{2} \quad \text{and} \quad k_r r_r^2 = y_r + \frac{x}{2}$$

or

$$r_\ell^2 = R^2 + \frac{x}{2 k_\ell} \quad \text{and} \quad r_r^2 = R^2 - \frac{x}{2k_r} \ . \tag{8}$$

Defining $\bar{x}$ as $\dfrac{x}{(y_\ell + y_r)} = \dfrac{x}{R^2(k_\ell + k_r)}$

28

then
$$C_\alpha = \frac{(\frac{1}{k_\ell} + \frac{1}{k_r})\ (k_\ell + k_r)\ \bar{x}}{2 + (\frac{1}{k_\ell} - \frac{1}{k_r})\ \frac{(k_\ell + k_r)}{2}\ \bar{x}}$$
(9)

For the special case with identical diaphragm and backing plate assemblies on the two sides the calibration curve becomes simply

$$C_\alpha = 2\bar{x} \ .$$
(10)

Therefore, identical left and right diaphragms and backing plates shaped as paraboloids yield an exactly linear calibration curve.

Diaphragm and Backing Plate Strength Calculations--The only unique parts in the pressure coefficient meter which require very careful sizing and shaping are the diaphragms and backing plates. The diaphragms must be thin enough that the crease can roll easily along the backing plate yet strong and dimensionally stable to avoid significant stretching or bursting at the highest expected pressure difference. The backing plates must be as light as possible to avoid sensitivity to g load and stiff enough to avoid significant deflection under the highest expected pressure difference. The remaining parts are not unique to the pressure coefficient meter and will not be discussed.

A force balance in the axial direction performed on the axi-symmetric diaphragm shape in Figure 14 yields the following requirements for equilibrium,
$$2\pi r\ t_r\ \sin\theta = \pi r^2 p$$

where r is the distance from the axis of symmetry to the diaphragm surface, t_r is the tension along a meridian per unit length along a parallel, θ is the angle the surface of the diaphragm makes with a plane normal to the axis of symmetry, and p is the pressure difference across the diaphragm. A force balance performed along a meridian on the differential element as in Figure 15 yields another requirement for equilibrium.
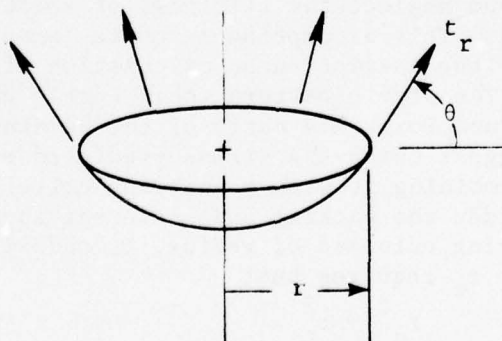
Figure 14. Radial Stress in Diaphragms

29

$$\frac{p\ (r - dr)}{2\ \text{Sin}\ (\theta - d\theta)}$$
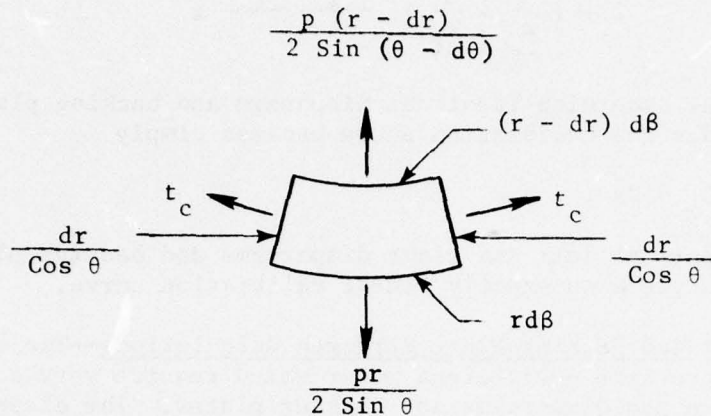
Figure 15. Circumferential Stress in Diaphragms

$$\frac{p_r}{2\ \sin\ \theta}\ rd\beta - \frac{p\ (r-dr)}{2\ \sin\ (\theta - d\theta)}\ (r - dr)\ d\beta = t_c\ \frac{dr}{\cos\ \theta}\ \frac{dr\ d\beta}{dr/\cos\ \theta}$$

where β is the azimuthal angle and t_c is the force along a parallel per unit length along a meridian. Solving the above two relations for t_r and t_c in terms of the pressures, one obtains

$$t_r = \frac{pr}{2\ \sin\theta} \tag{11}$$

$$t_c = \frac{pr}{\sin\theta} - \frac{pr^2}{2}\ \frac{\cos\theta}{\sin^2\theta}\ \frac{d\theta}{dr} \tag{12}$$

To predict the state of stress in the backing plate we first assume it to be very thin and neglect the stiffness of solid material outside of the diaphragm crease. This assumption is quite conservative. The only other models require the assumption or calculation of a strain pattern in the backing plate. The strain pattern would surely vary strongly with the backing plate shape and Poisson's ratio of the backing plate material. Consequently, we suggest using the stress predicted assuming a very thin backing plate and combining it with a buckling criteria or a failure criteria. Now consider the backing plate element shown in Figure 16. Equilibrium of the ring outboard of radius, r, and within the radius of the diaphragm crease r_c requires that

$$t_r = \frac{r_c^2 - r^2}{2r\ \sin\theta}\ . \tag{13}$$

30

To calculate the force along a parallel per unit length along a meridian consider the equilibrium of the element in Figure 17.
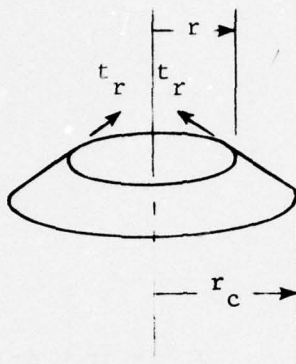
Figure 16. Radial Stress in Backing Plate

Equilibrium of the element requires

$$\frac{p\ (r_c^2 - r^2)}{2r\ \sin\ \theta}\ rd\beta\ -\ \frac{p\ (r_c^2 - (r - dr)^2)}{2\ \sin\ (\theta - d\theta)(r - dr)}\ (r - dr)\ d\beta = t_c\ \frac{dr}{\cos\ \theta}\ \frac{dr\ d\beta}{dr/\cos\ \theta}$$

Solving for t_c one obtains

$$t_c = -\ \frac{pr}{\sin\ \theta}\ -\ \frac{\cos\ \theta}{2\ \sin^2\theta}\ p\ (r_c^2 - r^2)\ \frac{d\theta}{dr} \tag{14}$$

From Equations (11-14) we conclude that the typical diaphragm is in tension both along parallels and along meridians while the backing plate is in tension along meridians and in compression along parallels. The yield stress and thickness of the plastic diaphragms are both generally much less than the corresponding values for the backing plates owing to the difficulty of manufacturing very thin metal backing plates and difference in material properties. Consequently, the most probable mode of failure for the backing plate is buckling.

The thin diaphragms are usually the weakest structure in the pressure coefficient meter. For cones the circumferential stress or "hoop stress" is twice the radial stress and is given by Equation (12) with $d\theta/dr = 0$. The stress is greatest at the outer edges of conical diaphragms. For example, the test instrument used Mylar®(σ_y = 12,000 psi) diaphragms 0.0005" thick. Thus, the maximum force per unit length of diaphragm was

31

t_y = 6 lbf/in = 72 lbf/ft. The outer radius of the diaphragm was 0.1 ft. Substituting into (12) and solving for the maximum possible pressure difference across the diaphragms, we get p_{oy} = 321 lbf/ft^2. This corresponds to a flight speed of about 350 miles/hour in sea level air. We only tested the instrument to about 140 miles/hour. One clearly should apply some safety factor and not plan to operate near the yield stress of the diaphragm material.

$$\frac{p}{2 \sin(\theta - d\theta)} \cdot \frac{r_c^2 - (r - dr)^2}{(r - dr)}$$

$(r - dr)\,d\beta$

$t_c \qquad t_c$

$\dfrac{dr}{\cos\theta} \qquad \dfrac{dr}{\cos\theta}$

$rd\beta$

$$\frac{p}{2 \sin\theta}\,\frac{\left(r_c^2 - r^2\right)}{r}$$
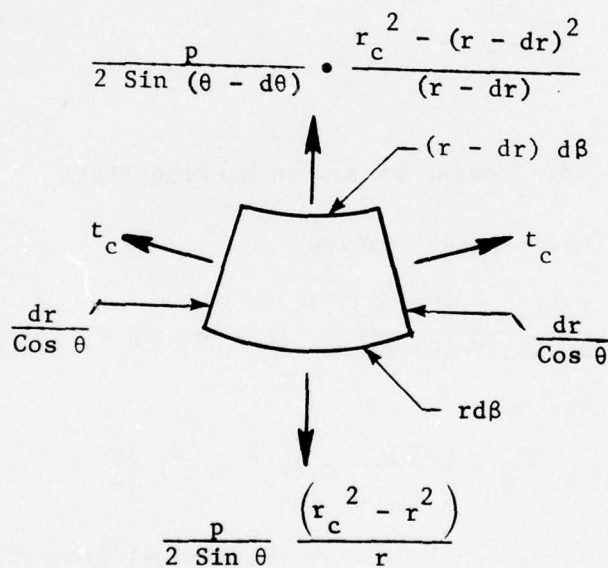
Figure 17. Circumferential Stress in Backing Plate

32

Stiffness and 'q' Sensitivity--An equation to estimate the error in the output of the pressure coefficient meter resulting from stretching or bulging of the diaphragms as the pressure difference across the diaphragms is increased while maintaining constant pressure coefficient is derived. To simplify the treatment we consider the pressure coefficient meter geometry shown in Figure 18 for $C_\alpha = 0$. If the pressure differences are increased in the instrument causing the diaphragms to bulge to the broken line; clearly the backing plate assembly will not move and there is no inaccuracy at $C_\alpha = 0$. However, if the pressure coefficient now changes the calibration curve will have a different slope. Specifically, with the bulged diaphragms, the backing plate assembly will have to move slightly farther to arrive an equilibrium position for a given pressure coefficient change. That is, the instrument may be slightly more sensitive to angle of attack at higher speed, and it is our goal here to estimate this effect.
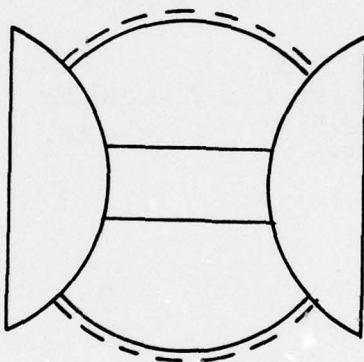
Figure 18. Spherical Diaphragm Instrument at $C_\alpha = 0$

The stress in the spherical diaphragm is given by Equations (11) and (12) with $r = \rho \sin \theta$ for a sphere of radius ρ.

$$t_c = t_r = \frac{p\rho}{2} \tag{15}$$

Since this is a state of uniform bi-axial stress and since a sphere has only one characteristic length, the strain results in an increase in ρ given by

$$\delta\rho = \frac{t_c (1 - \mu)}{ET} \rho$$

or

$$\frac{\delta\rho}{\rho} = \frac{\rho (1 - \mu) p}{2ET} \tag{16}$$

where E is the modulus of elasticity of the diaphragm material, μ is Poisson's ratio for the diaphragm material and T is the thickness of diaphragm material. Consider now the kinematics occurring near the

33

crease as the spherical diaphragm bulges, shown in Figure 19. Even at $C_\alpha = 0$, the crease will roll outward on the backing plate as the pressure difference across the diaphragm increases. The calibration curves of Figure 13 were derived assuming that the diaphragms would not stretch. Returning to Equation (7) we assume identical left and right diaphragms and backing plate assemblies and calculate the slope of the calibration curve near $C_\alpha = 0$.

$$\frac{dC_\alpha}{dx} = 2\,\frac{Y}{R} = \frac{2}{R}\,\frac{\cos\theta}{\sin\theta}$$

We now ask, how will the slope of the calibration curve change if the radius, R, is changed by the stretching?

$$\delta\left(\frac{dx}{dC_\alpha}\right) = \frac{\delta R}{2}\,\frac{\sin\theta}{\cos\theta} = \frac{\delta o}{4\cos\theta}$$

$$\frac{\delta\left(\frac{dx}{dC_\alpha}\right)}{\left(\frac{dx}{dC_\alpha}\right)} = \frac{\dfrac{\rho^2(1-\mu)\,p}{ET\,4\cos\theta}}{\dfrac{R\sin\theta}{2\cos\theta}} = \frac{p\,(1-\mu)\,\rho}{4\sin^2\theta\,ET} \tag{17}$$
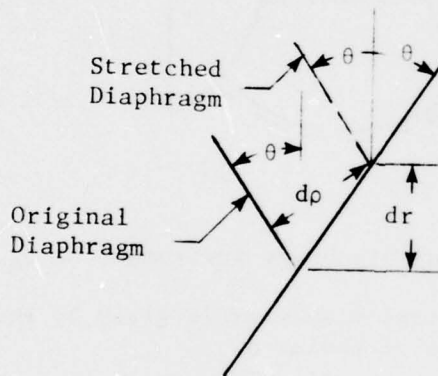
$$dr = d\rho\,\frac{\cos\theta}{\sin 2\theta} = \frac{d\rho}{2\sin\theta}$$

Figure 19. Kinematics of Crease with Diaphragm Stretching

Equation (17) greatly overestimates the effect of diaphragm stretching especially at small values of $\sin\theta$ because, particularly in that case, one would certainly restrain the diaphragm much closer to the crease than depicted in Figure 18. Less than one-fifth of the effect predicted by Equation (17) is likely to occur in practice. One should also note that a possibility exists for making the instrument self-correcting by designing the backing plates and connecting part such that these parts will deflect just enough to keep the slope of the calibration curve constant.

34

Typical values, taken from the test instrument and substituted into Equation (17),indicate a change in calibration curve slope of .03% at $p = 10$ lbf/ft^2 and .13% at 50 lbf/ft^2.

Inaccuracy Due to Friction--An estimate is needed of the inaccuracy in pressure coefficient indication due to mechanical friction in the needle or other display device which the diaphragm and backing plate assembly must drive. The display device is analyzed in the usual way to arrive at the force required at the backing plate assembly to cause it to move. Denote the force f. The condition for incipient movement becomes

$$(p_m - p_\ell) \pi r_\ell^2 (x) - (p_m - p_r) \pi r_r^2 (x) = f. \tag{18}$$

For any given three pressures one could, in principle, find 'x' as a function of the friction from Equation (18) and relate that to an error in C_α from the calibration curve derived earlier. However, since Equation (18) is unapproachable until one selects $r_\ell(x)$ and $r_r(x)$--which amounts to designing the instrument--it is more useful to be able to estimate the error in C_p resulting from friction independent of the functions $r_\ell(x)$ and $r_r(x)$. Consider the case where C_α is zero and we want to find the indicated C_α that could result from the friction f. First, we take the variation of Equation (3) which is a purely kinematic relation.

$$\delta C_{\alpha(ind)} = \frac{2[(R + \delta r_\ell)^2 - (R + \delta r_r)^2]}{(R + \delta r_\ell)^2 + (R - \delta r_r)^2} = \frac{2\delta r_\ell - 2\delta r_r}{R} \tag{19}$$

Now we return to Equation (18) of this section for small changes near $C_\alpha = 0$ when $p_n - p_\ell = p_n - p_r = p_o - p$.

$$\frac{2\delta r_\ell - 2\delta r_r}{R} = \frac{f}{\frac{1}{2} \rho_\alpha V_\infty^2 \pi R^2} \cdot \frac{1}{q_o} \tag{20}$$

q_o is an amplification factor, usually near one, dependent on probe design. Combining Equations (19) and (20) the desired equation for the erroneous pressure coefficient indication resulting from friction is obtained.

$$\delta C_{\alpha(ind)} = \frac{f}{\frac{1}{2} \rho_\infty V_\infty^2 \pi R^2} \cdot \frac{1}{q_o} \tag{21}$$

Of course this error can be in either direction as the frictional force changes sign depending on the direction of movement or incipient movement.

35

Pressure Coefficient Meter Response Characteristics--Early tests of
the Diaphragm-Type Angle of Attack Indicator where it was connected to a
wind tunnel model showed it to be unacceptably slow in response for
pilot use. Apparently this sluggishness was caused by the viscous
resistance to air movement through the narrow sections of tubing (internal
diameter equals 0.050") between the model and the instrument. It was also
recognized that if one provided large diameter and short length tubing,
the limiting factor in instrument response could well be the inertia of
the moving parts and the inertia of the air in the tubing. An approximate
linearized model of the pressure coefficient meter is developed here to
estimate the time constants associated with (1) viscous flow in the tubes,
and (2) the inertia of the air in the tubes and the internal mechanism.
To simplify the treatment we consider incompressible flow in a symmetrical
instrument with three connecting tubes of equal length and diameters and
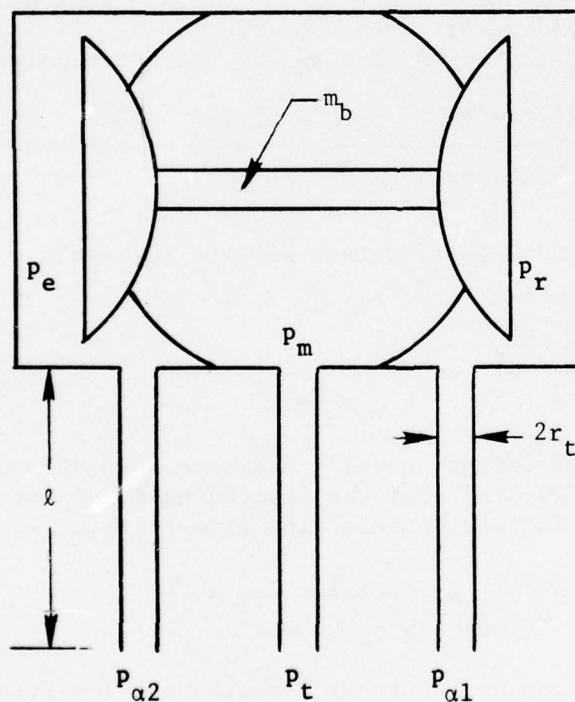allow only small displacement around the equilibrium position for $C_\alpha = 0$.

Figure 20. Symmetrical Pressure Coefficient
Meter for Deriving Time Responses

36

Consider now, Figure 20 and note that the kinematics of the diaphragm mechanism requires according to Equation (8).

$$r_\ell^2 = R^2 + \frac{x}{2k} \quad , \quad r_r^2 = R^2 - \frac{x}{2k}$$

Here we have assumed that the diaphragms and backing plates are identical paraboloids which is exactly equivalent to linearizing the equations for small displacements. The mass that must be accelerated when the instrument moves includes the backing plate assembly mass plus the equivalent mass of any attached indicating mechanism--the total being denoted by m_b. In addition, the mass of air in the tubes connected to the center chambers must be accelerated. The equivalent mass of the air in the two tubes is

$$m_a = \rho_\infty \pi r_t^2 \, 2\ell \, \frac{R^2}{r_t^2} \ = 2\rho_\infty \pi \, \ell R^2 \tag{22}$$

The factor R^2/r_t^2 is to account for the fact that the air in the tubes must move faster than the backing plate assembly by this factor. It may be easily verified that this equivalent mass is correct even when the velocity profile in the tubes is the characteristic paraboloid associated with laminar flow. The verification rests on the observation that the momentum of the air in the tubes varies like velocity to the first power. Consequently, the average momentum in the tube is equal to the average velocity multiplied by the mass of air in the tube. For small displacements about the $C_\alpha = 0$ equilibrium position the flow in the center tube can be neglected as the volume of the central chamber does not change. With these definitions the equation of motion becomes

$$(m_a + m_b) \frac{d^2x}{dt^2} = (p_m - p_r) \pi (R^2 - \frac{x}{2k}) - (p_m - p_\ell) \pi (R^2 + \frac{x}{2k}). \tag{23}$$

Conservation of mass and momentum applied to the tubes connected to the outer chamber yields:

$$\frac{dV_\ell}{dx} = \pi R^2 \qquad\qquad \frac{dV_\ell}{dt} = \frac{p_{\alpha 2} - p_\ell}{F}$$

$$\frac{dV_r}{dx} = - \pi R^2 \qquad\qquad \frac{dV_r}{dt} = \frac{p_{\alpha 1} - p_r}{F}$$

where V_r and V_ℓ are the volumes of the right and left chambers, respectively, the p's are identified in Figure 20 and F is the fluid mechanical resistance of the tubing. Combining the above equations we obtain

$$p_\ell = p_{\alpha 2} - \pi R^2 F \frac{dx}{dt} \text{ and } \quad p_r = p_{\alpha 1} + \pi R^2 F \frac{dx}{dt} \ .$$

Also observe that small displacements away from the equilibrium position causes no change in volume of the central chamber.

37

$$\frac{dV_m}{dx} = 0 \quad \text{and} \quad \frac{dV_m}{dt} = \frac{P_t - p_m}{F} \rightarrow (p_T - p_m) \approx 0$$

Solving for p_m, p_r, and p_ℓ and substituting in Equation (23) we obtain

$$(m_a + m_b) \frac{d^2x}{dt^2} = (P_t - p_{\alpha 1} - \pi R^2 F \frac{dx}{dt})(R^2 - \frac{x}{2k}) \pi - (P_t - p_{\alpha 2} + \pi R^2 F \frac{dx}{dt})(R^2 + \frac{x}{2k}) \pi.$$

Carrying out the indicated multiplication, discarding products of x and its derivative dx/dt and observing that $p_{\alpha 1} = p_{\alpha 2} = p$ for the equilibrium position described we have

$$(m_a + m_b) \frac{d^2x}{dt^2} = -2\pi^2 R^4 F \frac{dx}{dt} - \frac{P_t - p}{k} x .$$

From any standard fluid mechanics text one obtains

$$F = \frac{8 \mu \ell}{\pi r_t^4} ,$$

where ℓ is the length of the tube, r_t is the internal radius of the tube, and μ is the viscosity of the air. From the kinematics of the paraboloidal diaphragms and backing plates we have

$$\tan \theta = 2Rk .$$

Making these substitutions we arrive at the linearized equation of motion of the backing plate assembly.

$$(2\rho\pi\ell R^2 + m_b) \frac{d^2x}{dt^2} + \frac{16 \pi R^4 \mu \ell}{r_t^4} \frac{dx}{dt} + \frac{\pi 2R (p_t - p)}{\tan \theta} x = 0 \qquad (24)$$

One can investigate two limits in Equation (24) - the first corresponding to viscous damping dominated and the second corresponding to inertia dominated.

In the absence of inertia Equation (24) becomes

$$\frac{8 R^3 \mu \ell \tan \theta}{r_t^4 (p_t - p)} \frac{dx}{dt} + x = 0$$

which has the solution $x = x_o e^{(t/\tau_v)}$ where x_o is a constant and the time constant τ_v is given by

$$\tau_v = \frac{8 R^3 \mu \ell \tan \theta}{r_t^4 (p_t - p)} . \qquad (25)$$

38

In the absence of viscous damping Equation (24) becomes

$$(2\rho_\infty \pi \ell R^2 + m_b)\frac{d^2x}{dt^2} + \frac{2\pi R(p_t - p)}{\tan\theta} x = 0$$

which has the solution $x = x_o \sin(\frac{t}{\tau_i})$ where the time constant τ_i is given by

$$\tau_i = \sqrt{\frac{(2\rho_\infty \pi \ell R^2 + m_b)\tan\theta}{2\pi R(p_t - p)}} \quad . \tag{26}$$

Equations (25) and (26) may be used to estimate the behavior of a proposed design and installation. For the test installation in the T-41 aircraft the values were $\tau_i = .015$ sec and $\tau_v = .053$ sec indicating well damped behavior with sufficient speed for pilot use.

It should be realized that the foregoing derivation neglects the possibility of turbulent flow in the tubes which would tend to make the time constant τ_v larger than predicted by Equation (25). Entrance and exit losses at the tube ends were also neglected. In the case of higher speeds, where the air can no longer be regarded as incompressible, an additional time constant is associated with the viscous flow of air through the tube necessary to compress the air in the instrument to the new pressure.[32] If the tubes are made very short and the instrument volume is very small, acoustic propagation speed may become the limiting factor.[33]

Orientation and g Load Effects--Here we consider two specific problems to illustrate estimating the tolerance of the pressure coefficient meter to g loads in two directions. First, if the acceleration is along the axis of symmetry and the mass of the backing plate assembly is not balanced, then the assembly will move from the equilibrium position calculated in the section titled "Theoretical Calibration Curves," giving an erroneous reading. This error must be estimated. Second, if the acceleration is in a plane normal to the axis of symmetry; the backing plate assembly could be pulled toward the case causing "crinkling" of the diaphragms and an unreliable output indication. It is necessary to estimate the g load required to cause "crinkling" of the diaphragms.

---

[32] Herrington, R. M., Shoemacher, P. E., Bartlett, E. P., and Dunlap, E. W., "Pressure Lag Error--Theory and Calibration," Flight Test Engineering Handbook, Ch. 1, Sec. 4, Tech. Rep. No. 6273, Air Force Flight Test Center, May 1951 (rev. June 1964), pp. 28-47.

[33] Turner, K. J., "Free Flight Model Techniques for Aerodynamic Research at Supersonic and Hypersonic Speeds," Flight Test Instrumentation, Vol 3, Proceedings of the Third International Symposium, 1964, M. A. Perry, ed., Pergamon Press, pp 227-247.

If there is an acceleration of the pressure coefficient meter along the axis of symmetry of the diaphragm and backing plate assembly, the condition for equilibrium becomes

$$(p_m - p_\ell) \, \pi \, r_\ell^{\,2}(x) - (p_m - p_r) \, \pi \, r_r^{\,2}(x) = m_b \, g \tag{27}$$

where g is the acceleration and m_b is the mass of the backing plate assembly. For any given three pressures one could, in principle, find x as a function of the acceleration from Equation (27) and relate that to an error in C_α from the calibration curve derived as in the section titled "Theoretical Calibration Curves." However, since Equation (27) is unapproachable until we select $r_\ell(x)$ and $r_r(x)$, which amounts to designing the instrument, is is more useful to have an equation for estimating the error in C_α resulting from acceleration independent of the design of the instrument. To this end, consider the case where C_α is 0 and we desire to find the indicated C_α resulting from acceleration. First we take the variation of the kinematical relation.

$$C_{\alpha(ind)} = \frac{2 \, (r_\ell^{\,2} - r_r^{\,2})}{r_\ell^{\,2} + r_r^{\,2}}$$

$$\delta C_{\alpha(ind)} = \frac{2 \, [(R + \delta \, r_\ell)^2 - (R + \delta \, r_r)^2]}{(R + \delta \, r_\ell)^2 + (R + \delta \, r_r)^2} = \frac{2\delta r_\ell - 2 \, \delta \, r_r}{R} \tag{28}$$

Now we return to Equation (27) for small changes near $C_\alpha = 0$ where $p_m - p_\ell = p_m - p_r = p$.

$$p_m - p_\ell = p_m - p_r = p.$$

$$p \, \pi \, (R + \delta r_\ell)^2 - p \, \pi \, (R + \delta \, r_r)^2 = mg$$

$$\delta C_{\alpha(ind)} = \frac{2\delta r_\ell - 2\delta r_r}{R} = \frac{mg}{p \, \pi \, R^2} \tag{30}$$

To compute the g load in the plane perpendicular to the axis of symmetry necessary to "crinkle" the diaphragms, it is assumed that diaphragms will "crinkle" as soon as they are called upon to provide a compressive stress. Consider the force that can be procured by the diaphragm to support the backing plate assembly counting tensile forces only. Integrating this force over the half-circle we obtain

$$F_{max} = 2 \, t_r \cos \theta \, . \tag{31}$$

Combining this with Equation (11) the possible force becomes

$$F_{max} = \frac{pr^2}{\tan \theta} \tag{32}$$

40
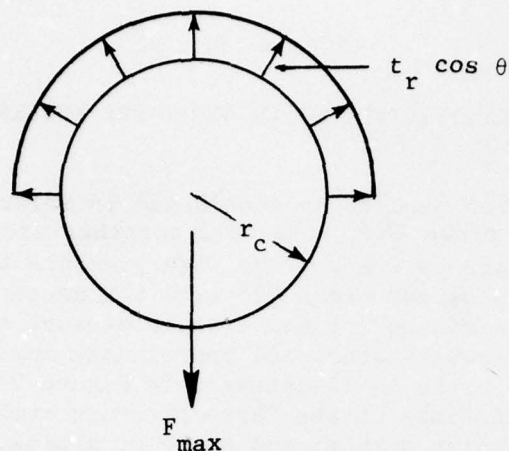
Figure 21. Tensile Forces in Diaphragms Supporting Backing Plate Assembly

Consider now the equilibrium of the entire backing plate assembly as in Figure 22. For a symmetrical assembly at $C_\alpha = 0$ we obtain a simple relation for the maximum g load consistent with an accurate output indication.

$$mg = \frac{p R^2}{\tan \theta} \tag{33}$$

For example, in the test instrument the typical values were $p = 10$ lbf/ft^2, $m_b = 5.5 \times 10^{-5}$ slg, and $R = 0.1$ ft. Equation (30) then indicates an error in C_α of 0.0175 would be caused by a 32.17 ft/sec^2 acceleration along the axis of the instrument. For this reason the instrument was designed so that the axis of symmetry would lie along the lateral axis of the test aircraft so that instrument error due to acceleration would only result from slips and skids and would be small. The value of $\tan \theta$ was 0.5 for the test instrument. Using this in Equation (33) reveals that the test instrument should be able to tolerate about 227 g's in a plane normal to the axis of symmetry before "crinkling" of the diaphragms would occur.

$$F_\ell < \frac{\left(P_m - P_\ell\right) r_r^2}{\tan \theta_\ell} \qquad\qquad F_r < \frac{\left(P_m - P_r\right) r_r^2}{\tan \theta_r}$$

Figure 22. Equilibrium of Backing Plate Assembly at $C_\alpha = 0$

41

SECTION III

PRESSURE COEFFICIENT METER AND PROBE INTERFACING

The factors which need to be considered in selecting a pressure co-efficient meter and probe that work well together are best illustrated by an example. A hemisphere-cylinder probe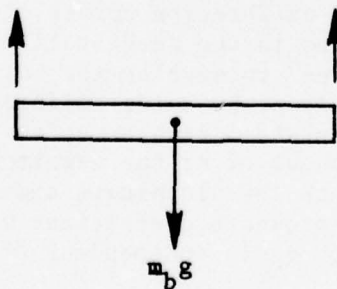 with pressure taps at the centerline on the nose and at plus and minus 45° from the centerline on the hemi-spherical surface is chosen for the example because this probe has been calibrated by many investigators and approximate analytical calibrations are possible. This probe is illustrated in Figure 23. The output of any three-holed probe consists of the three pressure coefficients as functions of Mach number, Reynolds number, and angle of attack. By combining the three pressure coefficients in a special way one can define three very useful coefficients, one of which is independent of the angle of attack α and two others which are nearly independent of Mach number and Reynolds number over rather wide ranges.

$$C_\alpha = \frac{P_{\alpha 2} - P_{\alpha 1}}{P_t - \dfrac{P_{\alpha 1} + P_{\alpha 2}}{2}} \tag{1}$$

$$q_\alpha = \frac{P_t - \dfrac{P_{\alpha 1} + P_{\alpha 2}}{2}}{\left[P_t - \dfrac{P_{\alpha 1} + P_{\alpha 2}}{2} \right]_{C_\alpha = 0}} \tag{34}$$

$$q_o = \frac{\left[P_T - \dfrac{P_{\alpha 1} + P_{\alpha 2}}{2} \right]_{C_\alpha = 0}}{\frac{1}{2} \rho_\infty V_\infty^2} \tag{35}$$

C_α and q_α are nearly independent of Mach and Reynolds numbers over wide ranges and are strong functions of angle of attack α. For a symmetrical probe, such as the hemisphere cylinder used in the example, C_α is an odd function of α and q_α is an even function of α. C_α vs. α clearly can be combined with calibration curves of the pressure coefficient meter, such as those described in the section titled "Derivation of Theoretical Calibration Curves" to develop the calibration curve of the probe-meter combination. This probe-meter calibration curve would give the displacement of the backing plate assembly, x, as a function of the angle of attack, α. q_α may be thought of as the magnitude of the driving pressures available to inflate the diaphragms and overcome friction and acceleration effects in the pressure coefficient meter ratioed with these driving pressures at $C_\alpha = 0$. q_o is independent of α, strongly dependent

42

on Mach number, and weakly dependent on Reynolds number. q_o is simply the available pressure to keep the diaphragms inflated at $C_\alpha = 0$ compared to the free stream dynamic pressure.
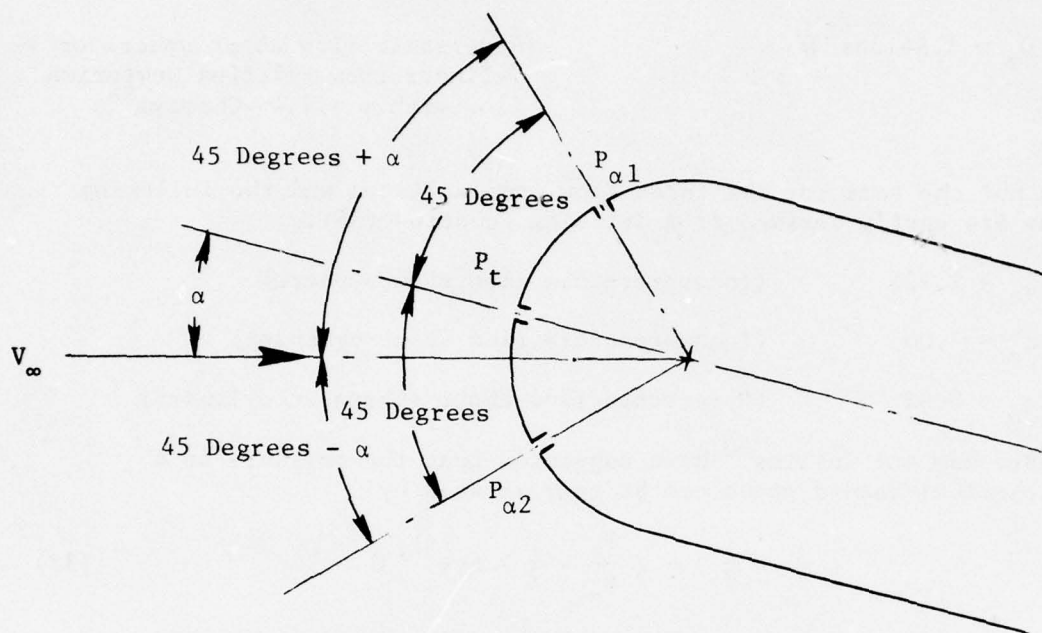
Figure 23. *Geometry of Hemisphere-Cylinder Probe*

Theoretical expressions for both C_α and q_α vs. the angle of attack, α, can easily be developed. Interestingly, these theoretically derived calibration curves are identical for (1) incompressible flow about a sphere, (2) incompressible flow about a right circular cylinder without circulation, and (3) hypersonic flow (modified Newtonian) about either a sphere or cylinder. The theoretically derived expressions are

$$C_\alpha = \frac{2\left[\sin^2 (45^\circ + \alpha) - \sin^2 (45^\circ - \alpha)\right]}{1 - 2 \sin^2 \alpha} \tag{36}$$

and
$$q_\alpha = 1 - 2 \sin^2 \alpha. \tag{37}$$

Equations (36) and (37) can be derived from any one of the following three expressions for pressure coefficient as a function of the angle away from the farthest upstream point on the hemisphere. θ of the upper hole is $45^\circ + \alpha$, θ of the lower hole is $45^\circ - \alpha$, and θ of the center hole is $|\alpha|$. The definitions (1) and (34) of course must be used.

43

$$\frac{p - p_\infty}{\frac{1}{2}\rho_\infty V_\infty^2} = C_p = 1 - \frac{\theta}{4}\sin^2\theta \qquad \text{(Incompressible flow about sphere-Lamb[34])}$$

$$C_p = 1 - 4\sin^2\theta \qquad \text{(Incompressible flow about cylinder-Kuethe \& Schetzer [35])}$$

$$C_p = 1.84\cos^2\theta \qquad \text{(Hypersonic flow about sphere or cylinder from modified Newtonian flow with } \gamma = 1.4 \text{ -Chernyi[36])}$$

q_o is not the same for the three flow models listed and the following values are easily derived from defining Equation (35).

$q_o = 1.125$ (Incompressible flow about sphere)

$q_o = 2.00$ (Incompressible flow about cylinder)

$q_o = 0.92$ (Hypersonic flow about sphere or cylinder)

Beecham and Collins[20] have suggested that the pressure on a hemispherical-headed probe can be approximated by

$$\left(\frac{p}{p_\infty} - \frac{1}{2}\right) = \left(\frac{p_o}{p_\infty} - \frac{1}{2}\right)\cos^{3/2}\theta \qquad (38)$$

for $0.7 < M < 2.0$ where θ in the angle measured from the forwardmost point on the hemisphere and p_o in the stagnation pressure for $M < 1$ and the stagnation pressure behind a normal shock for $M > 1$. The present author has also found that the Beecham & Collins empirical expression predicts, within a few percent, the more recent results of Markarieni[37] for "Nose C" at Mach numbers of 0.7, 0.8, 0.9, 1.0, and 1.1. However, the results at $M = 2.02$ are given more nearly by the modified Newtonian flow model. Using the Beecham and Collins empirical formula and the defining Equations (1), (34), and (35), the following expressions for C_α, q_α, and q_o are found.

---

[34] Lamb, Sir Horace, "Hydrodynamics," Dover Publications, New York, 6th Edition, 1932.

[35] Kuethe, A. M., and Schetzer, J. D., "Foundations of Aerodynamics," John Wiley and Sons, Inc., 2nd Edition, 5th Printing, October 1964.

[36] Chernyi, G. G., "Introduction to Hypersonic Flow," Academic Press, New York and London, 1961.

[37] Markarieni, F., "Experimental Surface Pressure Distribution on Three Bodies of Revolution from M = 0.7 to M = 2.2," Naval Weapons Center, NWC-TT-5393, AD-749934, August 1972.

$$C_\alpha = \frac{\cos^{3/2}(45^\circ - \alpha) - \cos^{3/2}(45^\circ + \alpha)}{\cos^{3/2}\alpha - \dfrac{\cos^{3/2}(45^\circ - \alpha) + \cos^{3/2}(45^\circ + \alpha)}{2}} \tag{39}$$

$$q_\alpha = \frac{\cos^{3/2}\alpha - \dfrac{\cos^{3/2}(45^\circ - \alpha) + \cos^{3/2}(45^\circ + \alpha)}{2}}{1 - \cos^{3/2}(45^\circ)} \tag{40}$$

$$q_0 = \frac{2}{1.4\ M^2}\left[(1 + 0.2\ M^2)^{3.5} - \frac{1}{2}\right](1 - \cos^{3/2}45^\circ),\quad \begin{matrix} M < 1 \\ \gamma = 1.4 \end{matrix} \tag{41}$$

$$q_0 = \frac{2}{1.4\ M^2}\left[\left(\frac{6}{7M^2}\right)^{2.5}\left(\frac{6M^2}{5}\right)^{3.5} - \frac{1}{2}\right](1 - \cos^{3/2}45^\circ),\quad \begin{matrix} M > 1 \\ \gamma = 1.4 \end{matrix} \tag{42}$$

Equations (36), (37), (39) and (40) are displayed in Figure 24. C_α is an
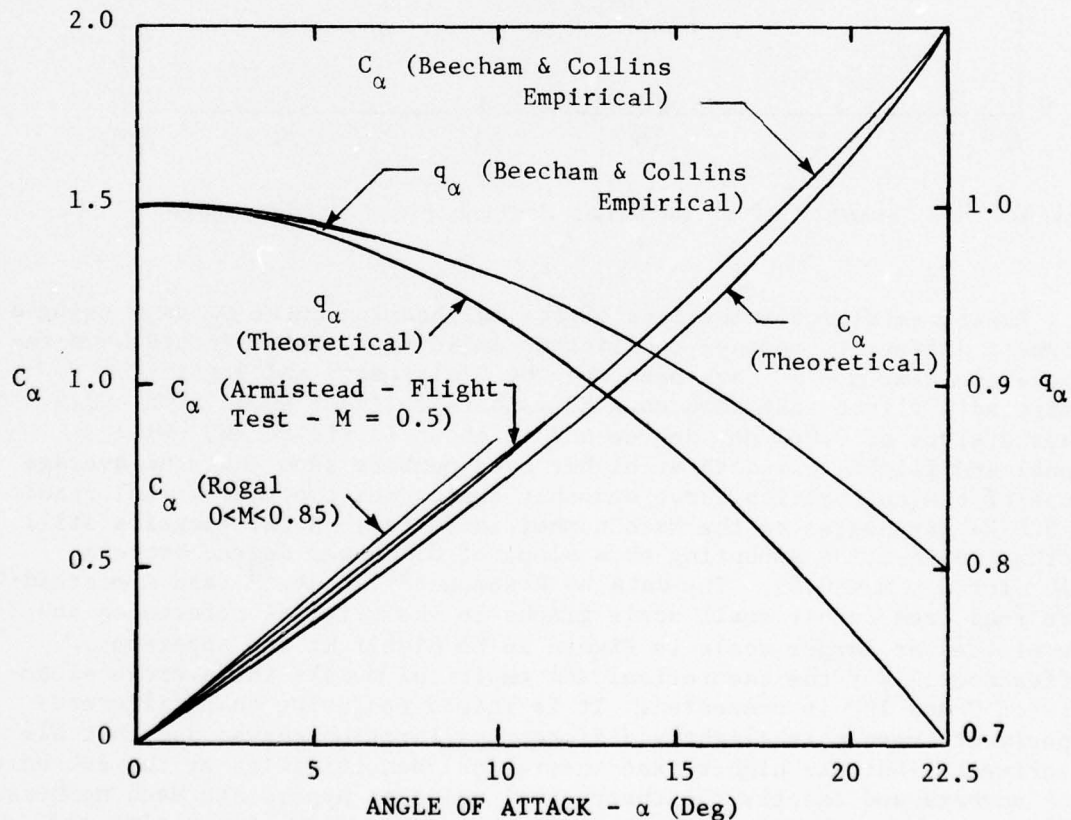

Figure 24. Hemispherical Headed Probe Calibration Curves

45

odd function of α and q_α is an even function of α. Equation (36) gives a value of 0.724 at $\alpha = 10^o$. Equation (39) gives a value of 0.788 at $\alpha = 10^o$. Figure 25 summarizes the rather sketchy available q_o data.
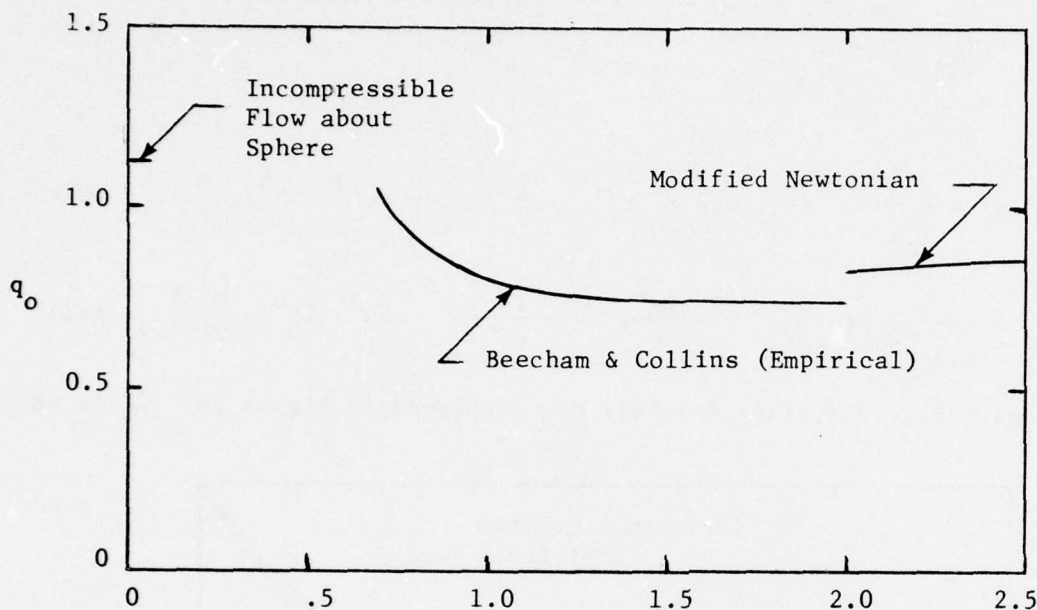
Figure 25. Summary of q_o Data for Hemispherical Headed Probe

Experimental determinations of the calibration curve C_α vs α using a slightly different pressure coefficient definition, which should have the same slope near $\alpha = 0$, have been made by Armistead[26] and Rogal[23]. Armistead's flight test data on a hemisphere-cylinder probe at M = 0.5 gives a slope of 0.080 per degree and is shown in Figure 24. Wind tunnel and flight test data at higher Mach numbers show that the average slope of the calibration curve smoothly approaches the theoretical result of 0.0724 per degree as the Mach number increases. Rogal suggests still another calibration amounting to a slope of 0.086 per degree between $\pm 10^o$ for $0 < M < 0.85$. The data by Rosemount[16], Rogal[23], and Armistead[26] were read from rather small scale graphs in the original references and are plotted at larger scale in Figure 26 to highlight the apparent differences. For the theoretical and empirical models the average slope between 0 and 10° is presented. It is indeed confusing that different experiments result in slightly different calibration curves and that all experiments indicate higher than theoretical sensitivities at the subsonic Mach numbers and exactly the theoretical value at hypersonic Mach numbers. Perhaps the after-body at angle of attack induces some circulation and associated lift causing the stagnation point to move slightly downward around the nose of the probe resulting in slightly enhanced sensitivity

46

at subsonic Mach numbers. Another factor that seems to have been neglected in the experiments is the condition of the boundary layer on the probe. Data taken by A. Frage[38] shows the pressure distribution in the vicinity of the 45° ports is significantly influenced by the condition of the boundary layer as it effects separation. The Reynolds number based on diameter above which permanent laminar separation does not occur on an aerodynamically smooth sphere is about 3×10^5 which corresponds to 563 ft/sec or 334 knots at standard sea level conditions for a one-inch-diameter sphere. Of course, surface condition of the probe and perhaps the static ports themselves could cause the critical Reynolds number to be more than a factor of four smaller corresponding to 140 ft/sec or 83.4 knots. A third possibility is the difference caused by the different sizes of static pressure ports used in the different experiments. Pressure port size is an especially important consideration for a probe to be used with the diaphragm type pressure coefficient meter because the instrument "inhales" and "exhales" quite a bit of air, thus requiring rather large ports to reduce the time constant to an acceptable value. With all these uncertainties in mind, the variations in calibration curves indicated by Figures 24 and 26 are surprisingly narrow.
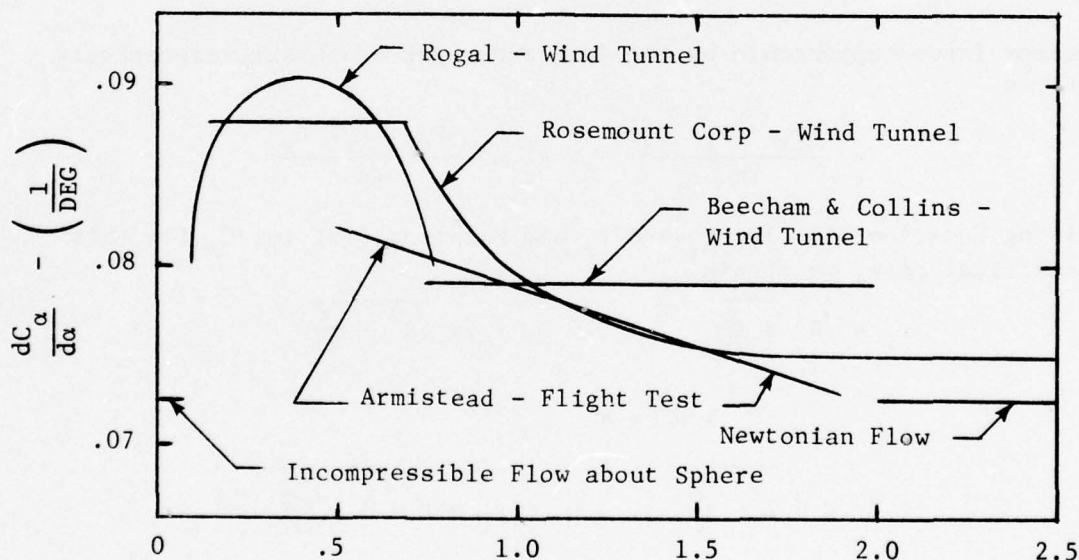

Figure 26. Summary of Sensitivity Data for Hemispherical Headed Probe

---

[38]
    Frage, A., Aeronautical Research Council Reports and Memoranda, No. 1766, 1937.

47

The hemispherical headed probe has good sensitivity throughout the pressure coefficient range $-2 < C_\alpha + 2$ and corresponding angle of attack range -22.5° to $+22.5^\circ$. At plus or minus $22\frac{1}{2}^\circ$ the pressure in the central chamber of the diaphragm type instrument becomes equal to the pressure in either the left or right side and the corresponding diaphragm will have no pressure difference to keep it inflated to the proper shape.

Even at lesser magnitudes of angle of attack the ability of the diaphragm tensile stresses to support the diaphragm away from the case is severely reduced. Returning now to Equation (32) we write an expression for the maximum force supported by the tension in the diaphragm on the left and right sides.

$$F_\ell = \frac{(p_m - p_\ell) r_\ell^{\,2}}{\tan \theta} \quad , \quad F_r = \frac{(p_m - p_r) r_r^{\,2}}{\tan \theta}$$

To investigate the simplest problem first suppose identical paraboloids of revolution are used for the backing plates and diaphragms. Then the slope of the surface at radius 'r' is given by reference to the text above Equation (9).

$$\tan \theta_{\ell,r} = \left. \frac{dz_{\ell,r}}{d\rho_{\ell,r}} \right|_{r=R} = 2 k r_{\ell,r} \; .$$

The max force supportable by the left and right diaphragm, respectively, becomes

$$F_\ell = \frac{(p_m - p_\ell) \, r_\ell}{2k} \quad , \quad F_r = \frac{(p_m - p_r) \, r_r}{2k} \; .$$

Solving Equation (8) for r_ℓ and r_r and Equation (10) for C_α for this symmetrical case, we obtain

$$r_\ell = \sqrt{R^2 + \frac{x}{2k}} \quad , \quad r_r = \sqrt{R^2 - \frac{x}{2k}}$$

$$C_\alpha k R^2 = x$$

$$r_\ell = R \sqrt{1 + \frac{C_\alpha}{2}} \quad , \quad r_r = R \sqrt{1 - \frac{C_\alpha}{2}}$$

$$F_\ell = \frac{(p_m - p_\ell) R \sqrt{1 + \frac{C_\alpha}{2}}}{2k} \quad , \quad F_r = \frac{(p_m - p_r) R \sqrt{1 - \frac{C_\alpha}{2}}}{2k}$$

Dividing by $p_m - \dfrac{p_\ell + p_r}{2}$ and multiplying by $2k$, one obtains the forces non-dimensionalized by the average pressure difference across the two diaphragms.

48

$$\frac{2F_{\ell}k}{R(p_m - \frac{p_{\ell} + p_r}{2})} = (1 - \frac{C_{\alpha}}{2})\sqrt{1 + \frac{C_{\alpha}}{2}} \qquad (43)$$

$$\frac{2F_r k}{R(p_m - \frac{p_{\ell} + p_r}{2})} = (1 + \frac{C_{\alpha}}{2})\sqrt{1 - \frac{C_{\alpha}}{2}} \qquad (44)$$

Unfortunately, the average pressure difference across the diaphragms does not remain constant as the angle of attack changes and Equations (43) and (44) must be multiplied by q_{α} to form a force coefficient non-dimensionalized with a pressure difference which is independent of angle of attack.

$$\frac{2F_{\ell}k}{R[p_m - \frac{p_{\ell} + p_r}{2}]_{C_{\alpha} = 0}} = (1 - \frac{C_{\alpha}}{2})\sqrt{1 + \frac{C_{\alpha}}{2}} \; q_{\alpha} \qquad (45)$$

$$\frac{2F_r k}{R[p_m - \frac{p_{\ell} + p_r}{2}]_{C_{\alpha} = 0}} = (1 + \frac{C_{\alpha}}{2})\sqrt{1 - \frac{C_{\alpha}}{2}} \; q_{\alpha} \qquad (46)$$

One obtains C_{α} vs. α and q_{α} vs. α from the probe calibration curves and substitutes into Equations such as (45) and (46) to obtain the forces available in the left and right diaphragms for supporting the backing plate assembly away from the case as functions of α. Theoretical probe calibration curves have been used here, although experimental data can be used as easily. Equations (45) and (46) were derived for parabolic diaphragms and different equations result for other shapes. These two curves are plotted in Figure 27 along with the total force available from the two diaphragms divided by its value at $C_{\alpha} = 0$ or $\alpha = 0$. Clearly, as the pressure coefficient goes near plus or minus two (corresponding to $\alpha \pm 22.5^{\circ}$) the ability of the instrument to tolerate g loads in a plane normal to the axis of symmetry is severely reduced.

For identical conically shaped diaphragms and backing plates on the two sides, we have from Equations (5) with a = b = 1

$$C_{\alpha} = \frac{4\bar{x}}{1 + \bar{x}^2}$$

$$\bar{x} = \frac{2}{C_{\alpha}} \pm \sqrt{\frac{4}{C_{\alpha}^2} - 1} \qquad \text{Minus sign for } C_{\alpha} > 0$$

$$\text{Positive sign for } C_{\alpha} < 0$$

where $\bar{x} = \frac{x}{2R \tan \theta}$.

49

The kinematics of the conical diaphragms, described in Figure 10, require

$$r_r = R + \frac{x}{2 \tan \theta} \quad \text{and} \quad r_r = R \frac{x}{2 \tan \theta} \; .$$

Making the indicated substitutions we obtain expressions for the left and right crease radii.
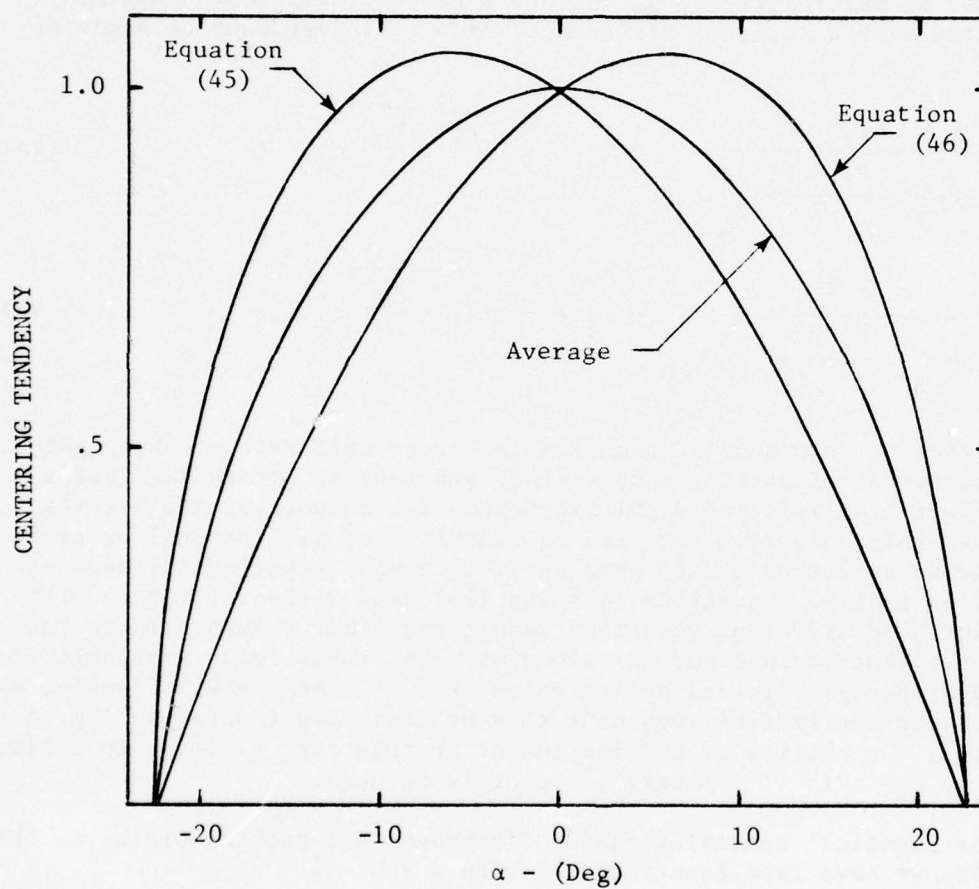

Figure 27. Centering Forces Assuming Identical Left and Right
Paraboloidal Diaphragms and Theoretical Probe Output

50

$$r_\ell^2 = R^2 \left(1 + \frac{2}{C_\alpha} \pm \sqrt{\frac{4}{C_\alpha^2} - 1}\right)^2$$

Minus sign for $C_\alpha > 0$

Plus sign for $C_\alpha < 0$

$$r_r^2 = R^2 \left(1 - \frac{2}{C_\alpha} \pm \sqrt{\frac{4}{C_\alpha^2} - 1}\right)^2$$

Plus sign for $C_\alpha > 0$

Minus sign for $C_\alpha < 0$

Substituting into Equation (32) the supportable force is obtained.

$$\frac{F_\ell \tan \theta}{R^2} = (p_m - p_\ell)\left(1 + \frac{2}{C_\alpha} \pm \sqrt{\frac{4}{C_\alpha^2} - 1}\right)$$

Minus sign for $C_\alpha > 0$

Plus sign for $C_\alpha < 0$

$$\frac{F_r \tan \theta}{R^2} = (p_m - p_r)\left(1 - \frac{2}{C_\alpha} \pm \sqrt{\frac{4}{C_\alpha^2} - 1}\right) .$$

Plus sign for $C_\alpha > 0$

Minus sign for $C_\alpha < 0$

Dividing the above two expressions by $\left(p_m - \dfrac{p_\ell + p_r}{2}\right)$ and multiplying by q_α one obtains the force divided by its value at $C_\alpha = 0$ in terms of C_α and q_α.

$$\frac{F_\ell \tan \theta}{R^2 \left(p_m - \dfrac{p_r + p_\ell}{2}\right)_{C_\alpha = 0}} = \left(1 - \frac{C_\alpha}{2}\right)\left(1 + \frac{2}{C_\alpha} \pm \sqrt{\frac{4}{C_\alpha^2} - 1}\right)^2 q_\alpha \qquad (47)$$

Minus sign for $C_\alpha > 0$

Plus sign for $C_\alpha < 0$

$$\frac{F_r \tan \theta}{R^2 \left(p_m - \dfrac{p_r + p_\ell}{2}\right)_{C_\alpha = 0}} = \left(1 + \frac{C_\alpha}{2}\right)\left(1 - \frac{2}{C_\alpha} \pm \sqrt{\frac{4}{C_\alpha^2} - 1}\right)^2 q_\alpha \qquad (48)$$

Plus sign for $C_\alpha > 0$

Minus sign for $C_\alpha < 0$

Equations (47) and (48) above are identical and the curve is presented in Figure 28.

51

One might incorrectly conclude by reference to Figures 27 and 28 that conical diaphragms and backing plates would have good g tolerance over a larger C_α range and corresponding α range than the paraboloidal shape. The position of the center of mass of the backing plate assembly in relation to the position of the two creases (where the supporting forces act) must also be considered. As C_α increases, the backing plate assembly moves distance 'x' to the right and the creases move to the left relative to the backing plate assembly by x/2. Let 'b' be the distance between the crease planes at $C_\alpha = 0$. The forces required to support the backing plate assembly on the left and right sides are

$$F_{\ell_{req}} = \frac{W}{2}\left(1 - \frac{x}{b}\right) \text{ and } F_{r_{req}} = \frac{W}{2}\left(1 + \frac{x}{b}\right) .$$
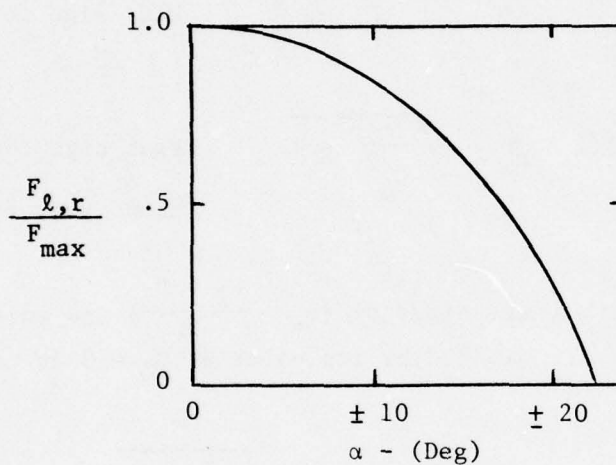

Figure 28. Centering Forces Assuming Identical
Left and Right Conical Diaphragms
and Theoretical Probe Output

52

From Equation (10) describing the calibration curves for identical paraboloidal diaphragms we obtain

$$x = C_\alpha \, k \, R^2$$

$$\frac{2 F_{\ell_{req}}}{W} = \left(1 - \frac{C_\alpha \, k \, R^2}{b}\right) \quad , \quad \frac{2 F_{r_{req}}}{W} = \left(1 + \frac{C_\alpha \, k \, R^2}{b}\right)$$

Now if one divides the non-dimensional available force given by Equations (45) and (46) by the non-dimensional required force above, expressions are developed which are useful for assessing the range over which the paraboloidal instrument can be used for various values of the parameter $b/k \, R^2$.

$$\frac{\dfrac{2 F_\ell \, k}{R \left[p_m - \dfrac{p_\ell + p_c}{2} \right]_{C_\alpha = 0}}}{\dfrac{2 F_{\ell_{req}}}{W}} = \frac{\left(1 - \dfrac{C_\alpha}{2}\right) \sqrt{1 + \dfrac{C_\alpha}{2}} \; q_\alpha}{\left[1 - \left(\dfrac{kR^2}{b}\right) C_\alpha\right]} \tag{49}$$

$$\frac{\dfrac{2 F_r \, k}{R \left[p_m - \dfrac{p_\ell - p_c}{2} \right]_{C_\alpha = 0}}}{\dfrac{2 F_{r_{req}}}{W}} = \frac{\left(1 + \dfrac{C_\alpha}{2}\right) \sqrt{1 + \dfrac{C_\alpha}{2}} \; q_\alpha}{\left[1 + \left(\dfrac{k \, R^2}{b}\right) C_\alpha\right]} \tag{50}$$

The plot of Equations (49) and (50) for three values of b/kR^2 in Figure 29 shows that making $b/kR^2 \approx 4$ allows the instrument to remain properly inflated for about the equal magnitudes of C_α positive or negative.

A similar computation carried out for conical diaphragms and backing plates shows that the very symmetric behavior (both diaphragms equally likely to collapse) shown in Figure 28 is for an infinite span between the creases and that at finite spans cause the diaphragm whose crease is nearest the center of mass of the backing plate assembly to be most subject to collapse under g load. An infinite span between creases with paraboloidal diaphragms would yield curves identical to those in Figure 27.

53
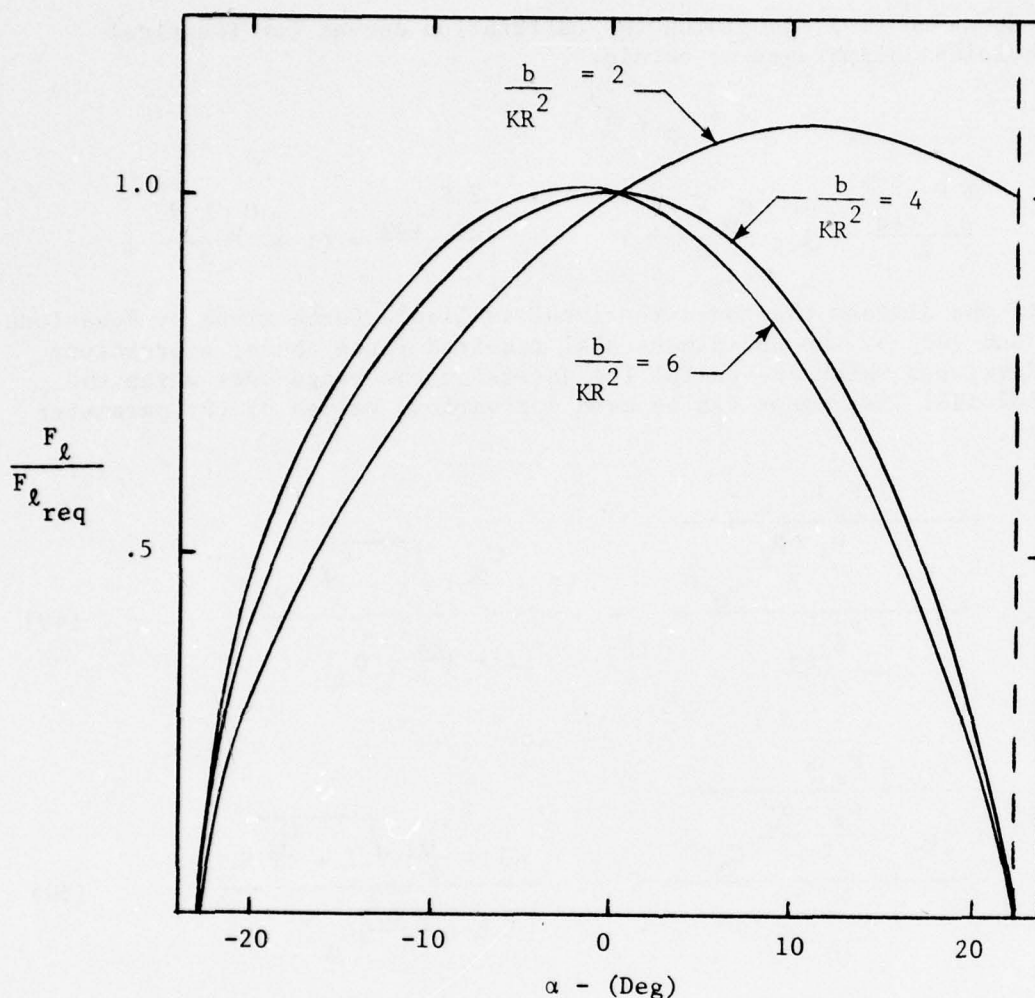
Figure 29. Resistance of Left Diaphragm to Collapse Due to g Force for Identical Paraboloidal Left and Right Diaphragms and Theoretical Probe Output

In summary, the requirements for matching the probe and indicator are: (1) output curves for the probe (represented here by Figure 24); (2) the possible centering forces for each diaphragm (represented here by Equations (45) and (46); (3) the calibration curves giving C_α as a function of x (represented here by the Equation $C_\alpha = 2\bar{x}$); and (4) the spacing between the backing plates (represented here by the parameter $b/kR^2 = 4$). These four pieces of information are combined as in the example discussed above to arrive at a curve as in Figure 29 for

54

$b/kR^2 = 4$. From this curve one concludes that the particular probe and pressure coefficient meter considered would operate between $\pm 10^o$ while retaining the ability to tolerate 85% of the g load calculated by Equation (33).

Another question that can be easily addressed is: How does the indicated $C_{\alpha_{ind}}$ differ from the actual C_α where $C_\alpha \neq 0$? Equilibrium of the backing plate assembly with a g force along the axis requires

$$(p_m - p_\ell) \; \pi \; r_\ell^2 - (p_m - p_r) \; \pi r_r^2 = mg.$$

For paraboloidal diaphragm assemblies we have

$$C_{\alpha_{ind}} - C_\alpha = \frac{mg}{\pi \; R^2 \left[p_m - \frac{(p_r + p_\ell)}{2} \right]}$$

$$C_{\alpha_{ind}} - C_\alpha = \frac{mg}{\pi \; R^2 \left[p_m - \frac{p_r - p_\ell}{2} \right]_{C_\alpha = 0}} \; \frac{1}{q_\alpha} \; . \tag{51}$$

Thus, the erroneous C_α indication would be greater than that calculated by Equation (30) if $C_\alpha \neq 0$. Specifically, for the hemispherical probe and paraboloidal diaphragms considered here one sees by reference to Figure 24 that the appropriate factor is $1/.94 = 1.06$ at $\pm 10^o$.

SECTION IV

PRESSURE COEFFICIENT METER CONSTRUCTION

The pressure coefficient meter illustrated in Figures 30 and 31 was constructed. In this instrument the backing plate assembly drove the indicating needle through a simple connecting rod and crank arrangement. All parts except the diaphragms were fabricated from basic metals, glass and plastic by standard shop procedures. Some assembly procedures were unlike those of other instruments. Some useful procedures were learned in fitting the conical backing plates to the conical diaphragms. In the following paragraphs the manufacture of diaphragms and instrument assembly procedures are discussed.

MANUFACTURE OF DIAPHRAGMS

The diaphragms were pressure formed at 450°F from transparent half-mil (0.0005") flat Mylar® Type A film. The literature on plastic forming does not encourage this method for Mylar®. After months of frustration with various contact cemented seams, the authors finally accepted the suggestion of Mr. Glander, the instrument builder, and tried the hot pressure forming method. It was found to be quite successful for this rather shallow shape.
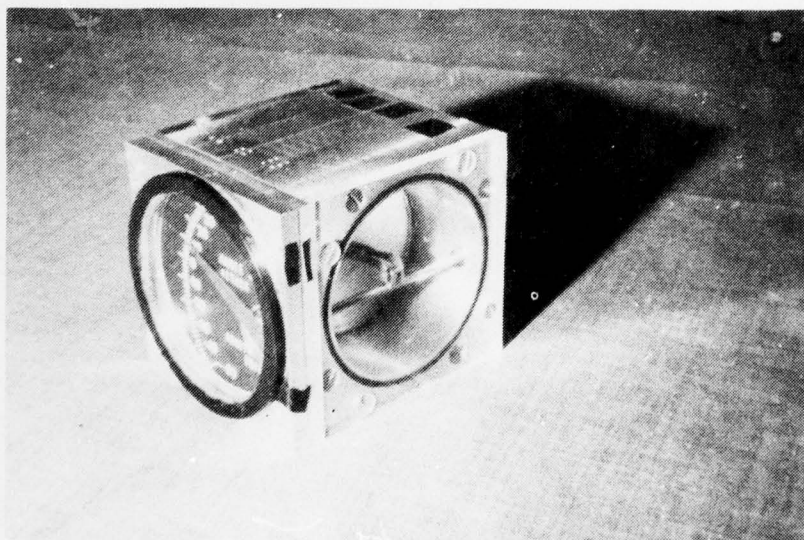

Figure 30. Photograph of Diaphragm Type Pressure Coefficient Meter
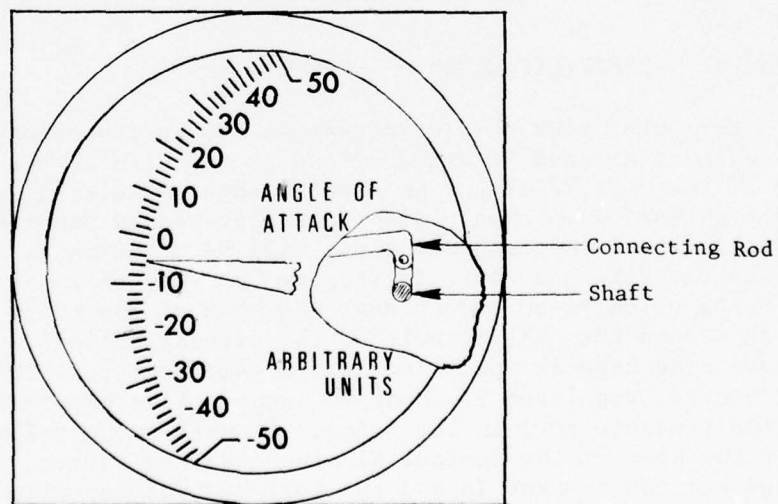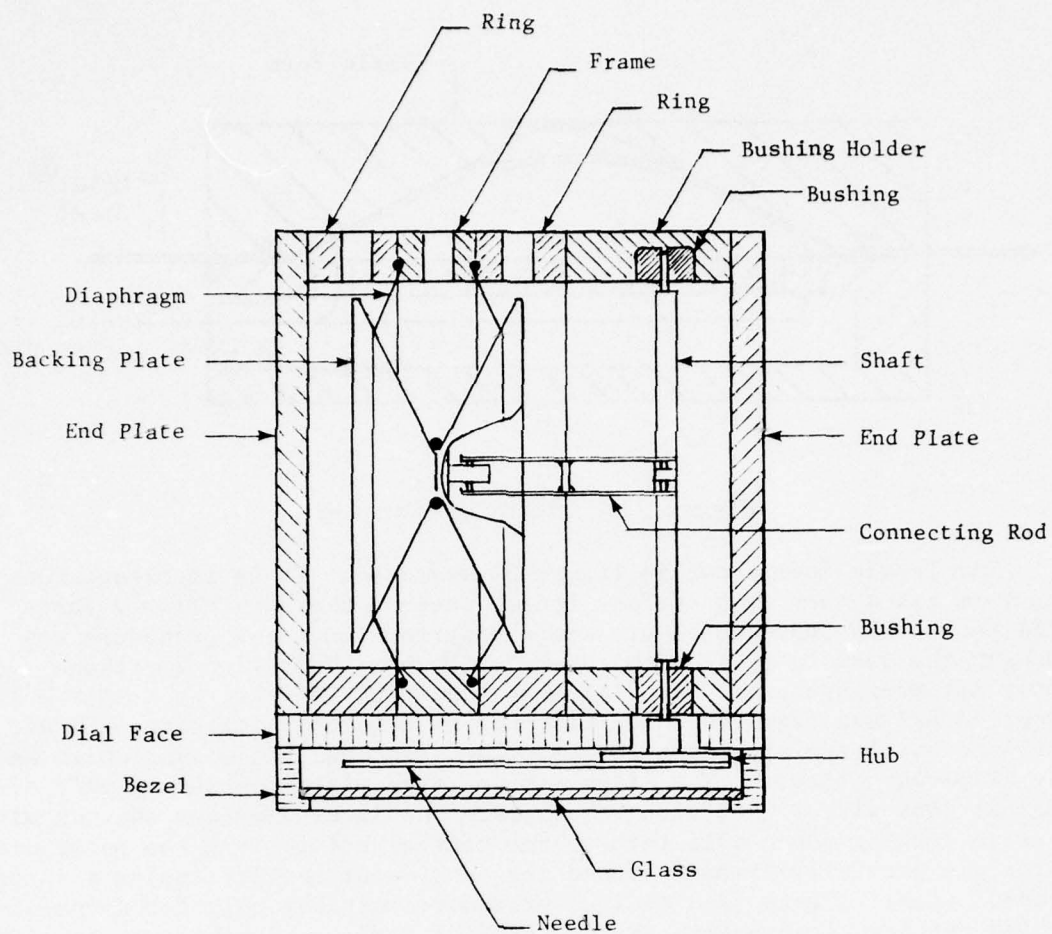
56

Figure 31. Assembly Drawing of Pressure Coefficient Meter
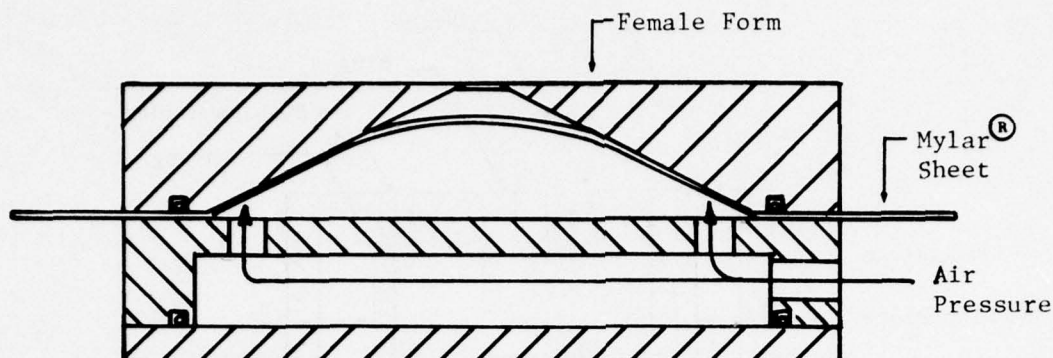
57

Female Form

Mylar® Sheet

Air Pressure

Figure 32. Diaphragm Forming

The female form shown in Figure 32 was used. It is important that the form has a very good surface finish because the thin Mylar® sheet will accurately reproduce every minor imperfection. The procedure was to heat the form to 450°F with the Mylar® sheet installed and then apply air pressure until the film just became visible at the center hole. About 30 psi was required. The film was held in this position with air pressure until the apparatus cooled. The form was then disassembled and the diaphragm removed. The diaphragm was then placed between a pair of conical dies with a hole along the axis. The inner diameter was cut with a close fitting punch slid through the central hole. Then the outer diameter was carefully trimmed around the outside of the dies using a razor blade. Clearly, this is a tedious procedure suitable only for a one-of-a-kind research instrument. For production, serious thought must be given to methods for the efficient manufacture of diaphragms.

PRESSURE COEFFICIENT METER ASSEMBLY

The outer edge of a diaphragm is set in its triangular groove in the frame and a greased 'o' ring of the proper size is placed carefully on top of the Mylar® diaphragm's outer edge. The ring is then installed and tightened down evenly with four flat-headed machine screws. If the installation is successful, there will be no wrinkles in the diaphragm. Before the same procedure is repeated on the other side, the small soft 'o' ring which is to end up near the apex of the cones is greased and stuck around the central hole of the already installed diaphragm. The second diaphragm is installed in the same manner as the first one. An air source, regulated to about 10 inches of water pressure, is attached to the pressure port in the frame. A small amount of grease is applied near the apex of the conical aluminum backing plates. The aluminum cones are now brought in and the bolt and nut installed. Care must be taken to assure that the cones end up centered in the case and that the axis of the backing plate assembly is aligned with the axis of the frame and rings. Also, the pivot pin in the bolt head, which is to later be

58

attached to the connecting rod, must be parallel to the bottom edge of the frame and consequently parallel to the indicating needle shaft when it is installed. All alignments are carefully checked by eye only and this has been found to provide adequate accuracy. The air pressure in the central chamber makes these alignment tasks much easier by keeping the diaphragms inflated as they will be when the instrument is in operation. After the nut is tightened, the air pressure is removed and epoxy is applied around the bolt head and the nut to prevent leakage along the bolt betewen the left and right chambers. Leakage from the central chamber is prevented by the 'o' ring near the apex of the cones. Leakage along the backing plate between the Mylar® and aluminum is prevented by the small amount of grease which was applied to the backing plate near the apex of the cone.

With the air pressure again applied one looks past the edge of each of the backing plates to see the crease in the Mylar® on the other backing plate. Ideally these creases should be perfectly circular and roll smoothly in and out as the backing plate assembly is displaced by pressing on the bolt head or nut. Two poorly understood difficulties can occur at this point. (1) The crease may appear polygonal with small pleats, transverse to the main crease, appearing at the apexes of the polygon. This pattern is sketched in Figure 33. (2) The crease may appear nicely circular but with the Mylar® standing away from the aluminum in small crescent shaped or ring shaped areas inside the main crease as sketched in Figure 34.
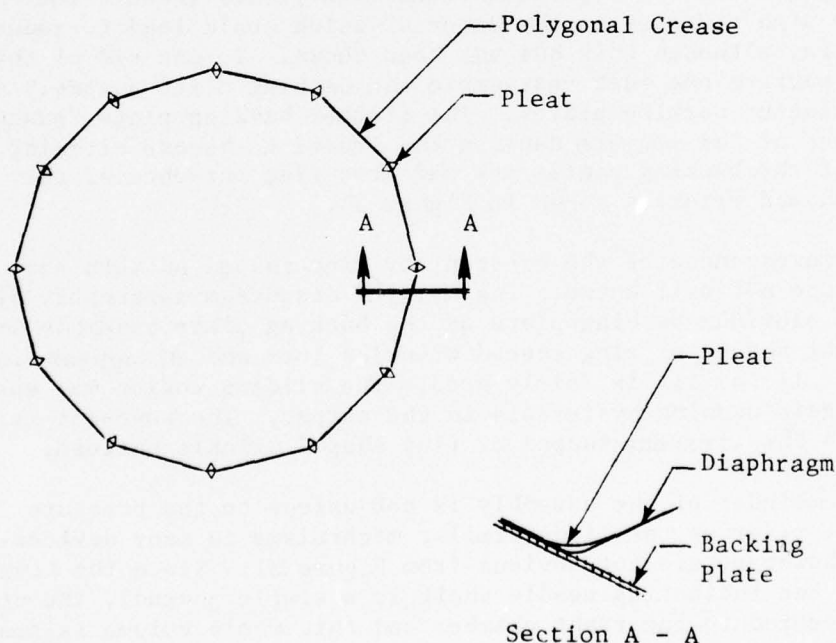

Section A - A

Figure 33. Polygonal Crease

59

Circular Crease

Crescent Wrinkle

B

B

Crescent
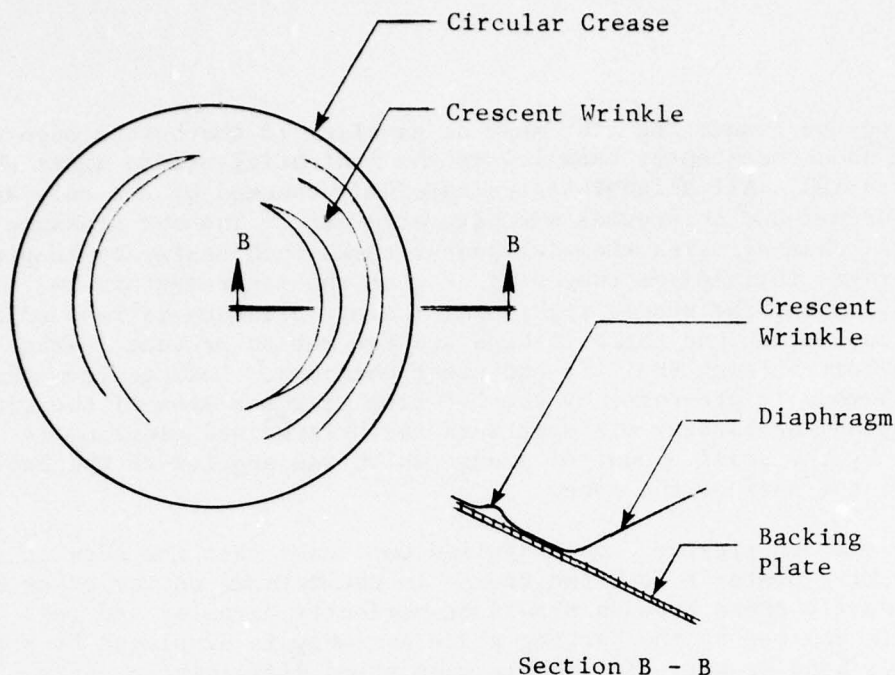Wrinkle

Diaphragm

Backing
Plate

Section B - B

Figure 34. Crescent Shaped Wrinkles

The polygonal pattern of Figure 33 caused a slight "crinkling" noise as the backing place assembly moved. Also it was apparent that the polygonal pattern was associated with an irregular friction-like force which caused appreciable hysteresis in the output. It is believed that the movement of the sharp pointed transverse pleats through the Mylar® must cause high stresses in the material which could lead to reduced fatigue life, although this has not been shown. To get rid of this polygonal pattern one must reassemble the backing plate assembly using slightly flatter backing plates. The flatter backing plate "pushes out" on the sides of the polygon causing the crease to become circular. However, if the backing plates are made too flat one obtains the crescent-shaped wrinkles shown in Figure 34.

The consequences of the crescent or ring shaped pattern shown in Figure 34 are not well known. The Mylar® diaphragm apparently slides a bit on the aluminum backing plate as the backing plate assembly moves. The crescent shaped or ring shaped wrinkles form and disappear inside the main crease if the fit is fairly good. The sliding action may appear as friction again causing hysteresis in the output. The movement is nearly silent with the crescent shaped or ring shaped wrinkle pattern.

The remainder of the assembly is not unique to the pressure coefficient meter as one finds similar mechanisms in many devices. Two features, however, are not obvious from Figure 31. Since the front bearing on the indicating needle shaft is a simple journal, the dial face cavity is vented to the right chamber and this whole volume is sealed with appropriately placed 'o' rings. Therefore, the glass face can be required to support a pressure difference and this will require checking for

60

pressurized aircraft of or for very high speed applications. To avoid
mechanical play, the connecting rod was made up of two parallel thin
spring bronze pieces fastened in the middle to a post for proper
spacing. The tiny holes in respective ends of the connecting rod then
could be easily snapped over the pivots on the bolt through the
backing plate assembly and over the pivots on the crank.

61

TESTING

Component tests of various parts of the pressure driven angle
of attack indicating system and complete tests of the assembled system
in the wind tunnel and on an aircraft are described.

PRESSURE COEFFICIENT METER TESTS

A fatigue test of sample pressure coefficient meter diaphragms
was conducted to allay any fears that the life of this component might
be too short for use in a practical device. While no diaphragms were
tested to failure of the Mylar® material, enough cycles were accumulated
to develop complete confidence in the Mylar® diaphragms. Also, a meter
response test was run with various sized tubes connecting the probe and
the meter in an attempt to verify Equation (25). As might be expected,
agreement with Equation (25) was achieved only for very small tube
diameters. Both the diaphragm fatigue test and the response test were
made on the first pressure coefficient meter in which the two backing
plates were connected by nylon string which was wrapped windlass-fashion
around the indicator needle shaft in the central chamber. This first
pressure coefficient meter was fitted with the older diaphragms which
had contact cemented seams.

Diaphragm Fatigue Test--The apparatus depicted in Figure 35 was
used to maintain a pressure difference across the diaphragm and to cycle
the diaphragm through the proper range of movement. The range of move-
ment was set so that the crease rolled from the outer edge of the conical
aluminum backing plate into a radius of about two-thirds that of the
outer edge. The counter advanced one for each complete cycle. The dia-
phragm was checked for leaks about every 100 cycles by: (1) disconnecting
the string from the cycling mechanism; (2) turning the diaphragm retaining
ring upside-down on the test cylinder; (3) pressurizing the cylinder
slightly with air; (4) placing the test cylinder and diaphragm under water;
and (5) exercising the diaphragm manually by pressing on the center of the
backing plate. The appearance of bubbles indicated a leak.

The results of the fatigue test are summarized in Table 3. These
results show clearly that the contact cemented seam was the weakest part
of the diaphragm. No leaks ever developed in the parent Mylar® material.
Consequently, an estimate of the fatigue life of the newer heat and
pressure formed diaphragm is not possible. It is certainly possible to
conclude that the heat and pressure formed diaphragms will have a fatigue
life exceeding 2000 complete cycles.
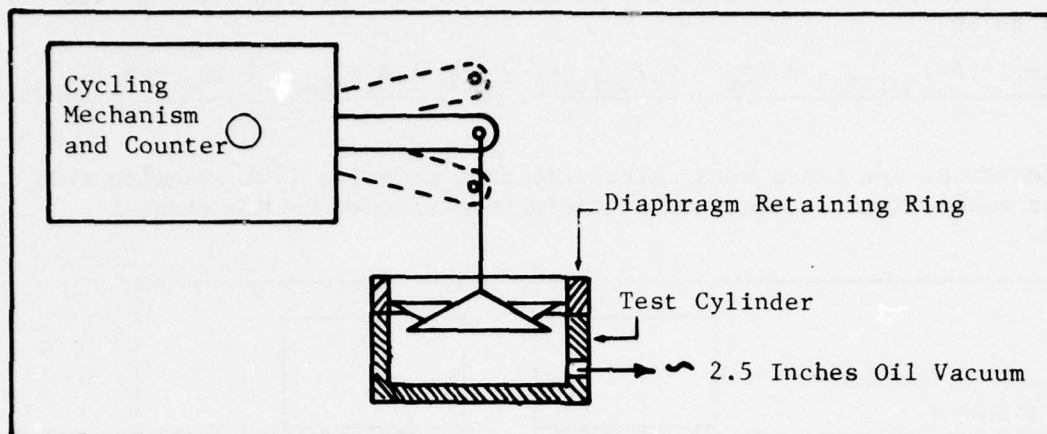
Figure 35. Diaphragm Fatigue Test

TABLE 3. RESULTS OF DIAPHRAGM FATIGUE TEST

Diaphragm	1	2	3
Initial Condition	Small Leak in Seam	Leak Free	Leak Free
Pressure Difference	2.15 in. of oil	2.15 in. of oil	2.62 in. of oil
Cycling Rate	0.1 cps	0.4 cps	0.4 cps
Results	No change @ 100 cycles. Leak increased at 1000 cycles.	Small leak appeared in seam at 2000 cycles.	Small leak appeared in seam at 2000 cycles.

Pressure Coefficient Meter Response Test--The apparatus depicted in Figure 36 was used to measure the time constant of the pressure coefficient meter. The procedure was to suddenly partially block or unblock one of the vacuum hoses to cause an instantaneous change in pressure at either the left or right tube. The movement of the indicator was assumed to be restricted primarily by the viscous flow through the narrow sections of tube. This assumption was verified by Equations (25) and (26) which showed that viscous damping was much more important than inertia. A motion picture camera recorded the movement of the blockage, the movement of the pressure coefficient meter needle, and the clock. Later, the position of the pressure coefficient meter indicating needle was plotted vs. time on semi-log paper with the pressure coefficient meter indicating needle position on the logarithmic scale. A straight line was passed through the data by

63

eye and the 1/e time taken from the slope. The average pressure, p, was defined to be

$$p = \frac{(p_m - p_\ell)_{initial} + (p_m - p_r)_{initial} + (p_m - p_\ell)_{final} + (p_m - p_r)_{final}}{4}.$$

The theoretical 1/e times were calculated from Equation (25) assuming that only the small diameter sections of tubing contributed to the viscous damping.
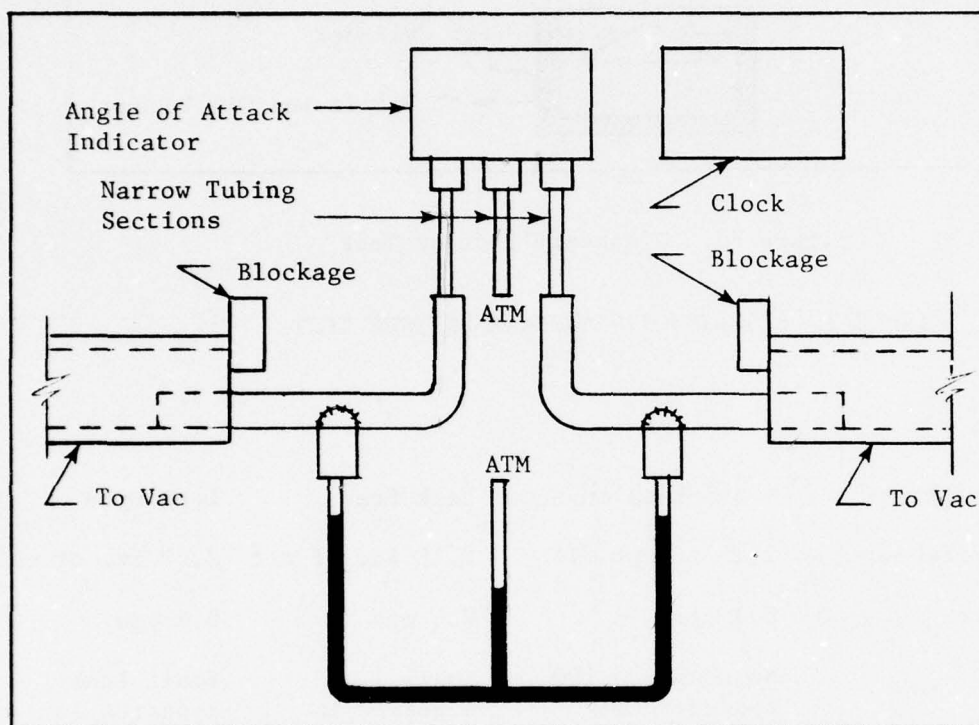
Figure 36.   Pressure Coefficient Meter Response Test

The results are presented in Table 4. Agreement was nearly achieved only for the smallest diameter tubes. Differences between the experimental and theoretical values are attributed to: (1) turbulent flow in the tubes; (2) losses in the large diameter tubes; and (3) inability to change the pressure quickly enough to measure the very short time constants. Experimental time constants of less than one-tenth of a second were achieved--certainly fast enough for pilot use.

64

TABLE 4.   TIME RESPONSE TEST RESULTS

Length of Narrow Tube - (In)	Internal Radius of Narrow Tube - (In)
Pressure - (Lbf/Ft^2)	
Theoretical 1/e Time - (Sec)	Measured 1/e Time - (Sec)

6	.026
24.85	
.387	.583

6	.026
39.97	
.250	.435

6	.0505
25.77	
.027	.227

6	.0505
39.46	
.018	.320

3	.0505
25.27	
.014	.183

3	.0505
41.58	
.008	.058

6	.0885
24.76	
.003	.085

6	.0885
37.16	
.002	.060

WIND TUNNEL TESTING

All wind tunnel tests were conducted in the U. S. Air Force Academy two-foot by three-foot subsonic wind tunnel. Since the probes were full sized, Reynolds number matching was perfect. The probes were mounted on a sideslip adjusting hinge which, in turn, was mounted on an angle of attack adjusting mechanism which could be operated while the tunnel was running. The sideslip angle had to be set manually with the tunnel off. The hinge line of the sideslip adjustment rotated with angle of attack changes. In other words, our angle of attack was the angle between the projection of the probe centerline on the vertical plane aligned with the wind and the horizontal plane. Our sideslip angle was the angle the probe centerline makes with the vertical plane aligned with the wind. This is in contrast to the usual definition where the angle of attack is the angle between the probe centerline and the horizontal plane and the angle of sideslip is the angle formed by the projection of the probe centerline on the horizontal plane and the vertical plane aligned with the wind. The conventional definition uses a spherical coordinate with a vertical axis whereas the system more directly applicable to our tunnel apparatus uses a spherical coordinate system with a horizontal axis perpendicular to the free stream velocity. For the small angles of sideslip considered here this difference is totally negligible.

65

Probe outlets were attached by plastic tubing to oil-filled manometers for probe calibrations and directly to the pressure coefficient meter for the combined system tests. Oil-filled manometers were also used to take the total and static pressure in the test section.

Probe Calibrations--Three probes suitable for use with the diaphragm type pressure coefficient meter were calibrated. These were given the descriptive names: (1) Hemi-Head Probe; (2) Winged Alpha Probe; and (3) Winged Wind Vector Probe. All these probes had large pressure ports to allow for adequate time response with the diaphragm type instrument. A fourth probe, called simply the Wind Vector Probe, was fully calibrated by Trumbull.[39] The Wind Vector Probe calibrations are not included here because the small pressure ports prevent the achievement of adequate time response with the diaphragm type pressure coefficient meter. The Wind Vector Probe performed well and is suitable for use with capacitive pressure sensors where the airflow requirements are not high.

Figures 37, 38, 39, and 40 summarize the calibration data collected on the three probes.

Several features of the Hemi-Head Probe calibration curves depicted in Figures 37 and 38 require interpretation. First, the product $q_o q_\alpha$ which was forecast by incompressible flow theory to have a maximum of 1.125 actually peaks at about 0.8 at zero sideslip. The apparent reason for this discrepancy is the very large holes in the Hemi-Head Probe which were required for adequate speed of response. The large holes apparently act a bit like air scoops and sense an average pressure appropriate to a position about one quarter of a hole diameter from the hole front edge. This, of course, primarily influences the tension in the diaphragms, making it less than predicted. Second, the slope of the C_α vs. angle of attack curve is about 0.094 per degree which is considerably higher than expected from theory -- namely 0.0724 -- and higher than any measured in previous experiments described in the section titled "Pressure Coefficient Meter and Probe Interfacing." This difference can again be attributed to the fact that the larger holes at $\pm 45^o$ sense pressures near their leading edges instead of at the hole centerline. Third, the fact that the C_α vs. angle of attack curve does not pass through the origin must be attributed to manufacturing inaccuracies resulting in non-axisymmetric geometry of the probe. Fourth, the vertical shift in the C_α vs. angle of attack curve with sideslip must also be attributed to manufacturing inaccuracies. A systematic error of an axisymmetric probe would require the curves to cross at the origin and to have different slopes. The fact that the zero sideslip and small sideslip curves have the same slope shows that the design, if accurately manufactured, would have practically no sensitivity to sideslip --a very desirable feature. Fifth, the shift of the $q_o q_\alpha$ vs. angle of attack

[39] Trumbull, K. and T. Carter, "A Report on the Wind Vector Probe," Aero 350 Laboratory Report, Dept of Aeronautics, USAF Academy, Dec. 1973.

0.750 Inch

45 Degrees.

0.155 Dia Ports Typ

Hemi-Head Probe
Calibration Curves
M = 0.21
$R_e = 6.5 \times 10^4$

$q_o q_\alpha$, $\beta = 5$ Degrees

$q_o q_\alpha$, $\beta = 0$

C_α, $\beta = 5$ Degrees

C_α, $\beta = 0$

C_α

$q_o q_\alpha$
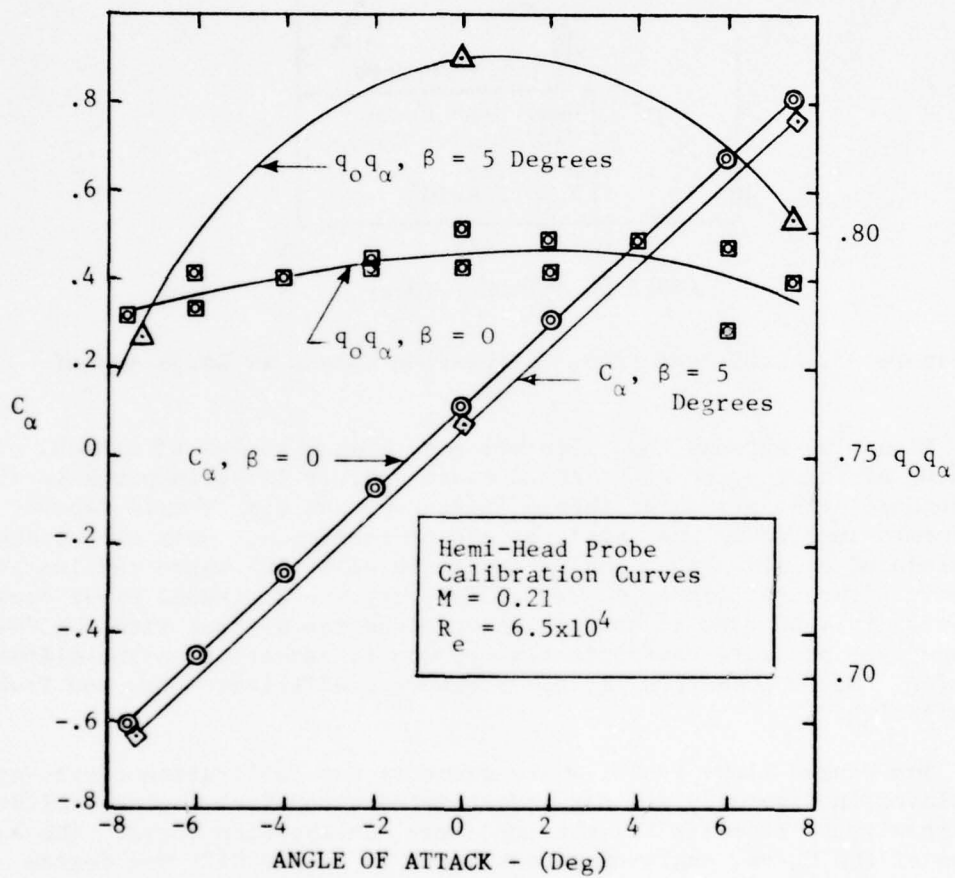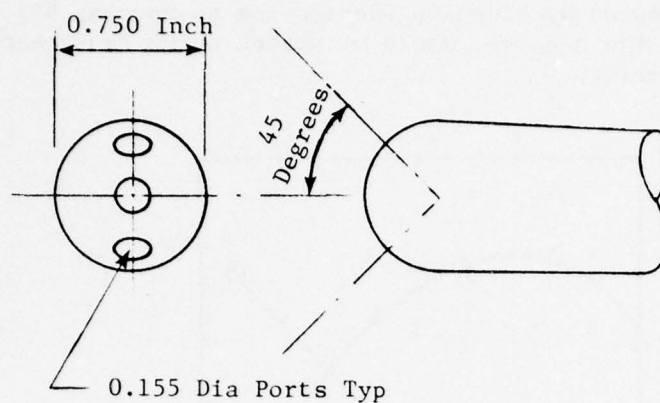
ANGLE OF ATTACK - (Deg)

Figure 37.   Hemi-Head Probe Calibration Curves at Small Angles

67

curve caused by sideslip cannot be simply and certainly attributed to manufacturing errors. However, the fact that the theory indicates that $q_o q_\alpha$ should be reduced by sideslip (decreasing to zero at 90) indicates that the shift in the $q_o q_\alpha$ vs. angle of attack curve is probably caused by manufacturing errors.
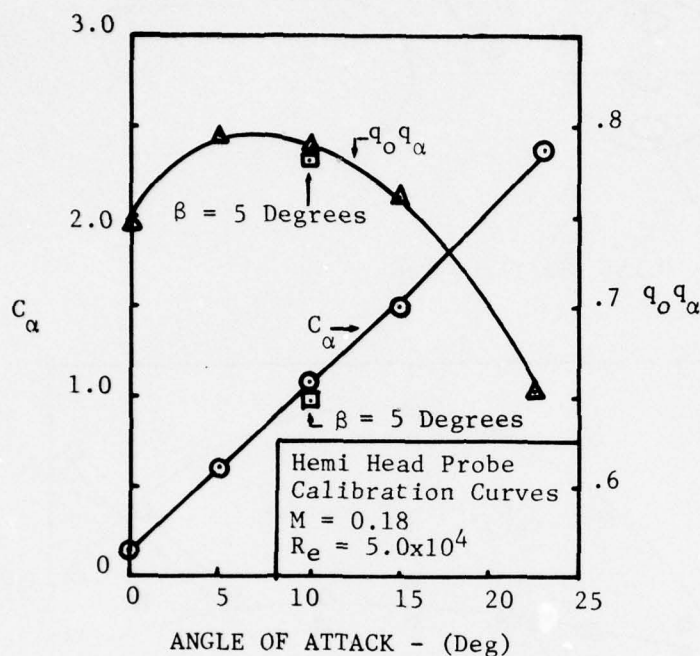

Figure 38. Hemi-Head Probe Calibration Curves at Large Angles

Figure 38 extends the calibration to higher angles of attack. The peaking of the $q_o q_\alpha$ curve at about seven degrees is again probably due to manufacturing errors as theory indicates that $q_o q_\alpha$ should become uniformly smaller as the angle of attack increases. Only tiny changes are induced by sideslip. The C_α vs. angle of attack curve retains good linearity through fifteen degrees. However, the Hemi-Head Probe could probably only be used to about plus or minus ten degrees with the diaphragm type pressure coefficient meter due to reduction in the diaphragm tension. (See the section titled "Pressure Coefficient Meter and Probe Interfacing.")

The Winged Alpha Probe, whose geometry and calibration curves are displayed in Figure 39, was not investigated extensively because of its sensitivity to sideslip and the nonlinear calibration curve. The average slope of the C_α vs. angle of attack curve is only 0.0175 per degree between zero and ten degrees angle of attack.

68

0.188 Inch

1.35 Inch

0.196 Inch

0.156 Inch

1.00 Inch

0.40 Inch

0.75 Inch

0.196 Inch

0.196 Inch

0.500 Inch Radius

$\frac{5}{32}$ Inch Dia Typ

Winged Alpha Probe
Calibration Curves
$M = 0.17$
$R_e = 5.8 \times 10^4$

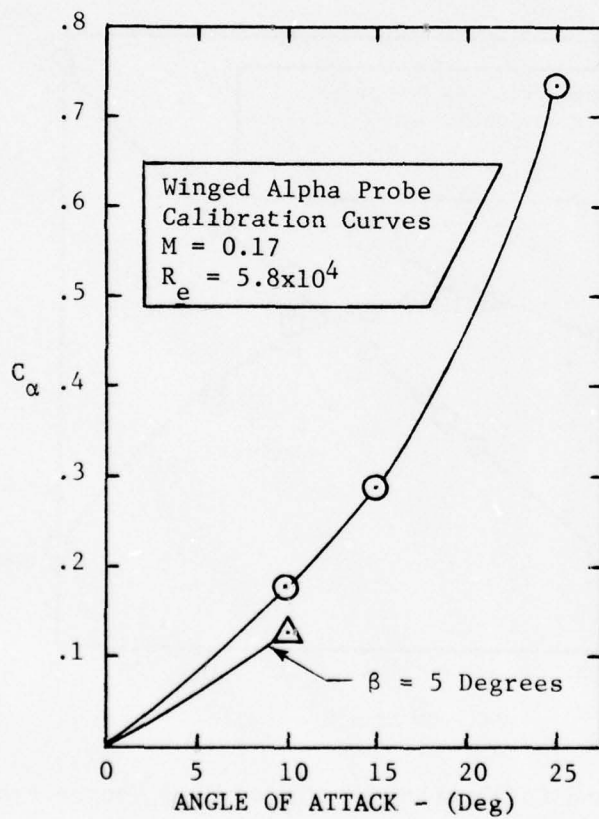C_α

$\beta = 5$ Degrees
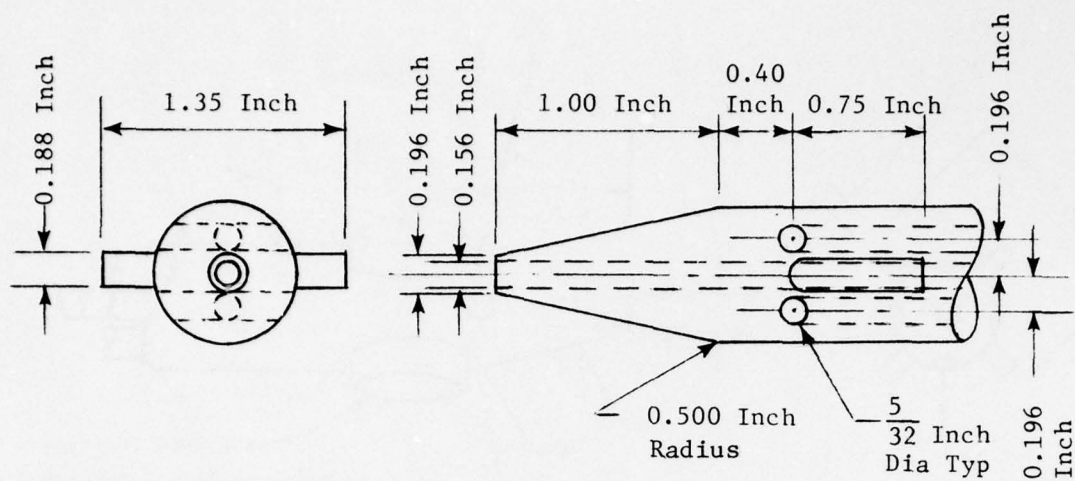
ANGLE OF ATTACK - (Deg)

Figure 39. Geometry and Calibration of Winged Alpha Probe
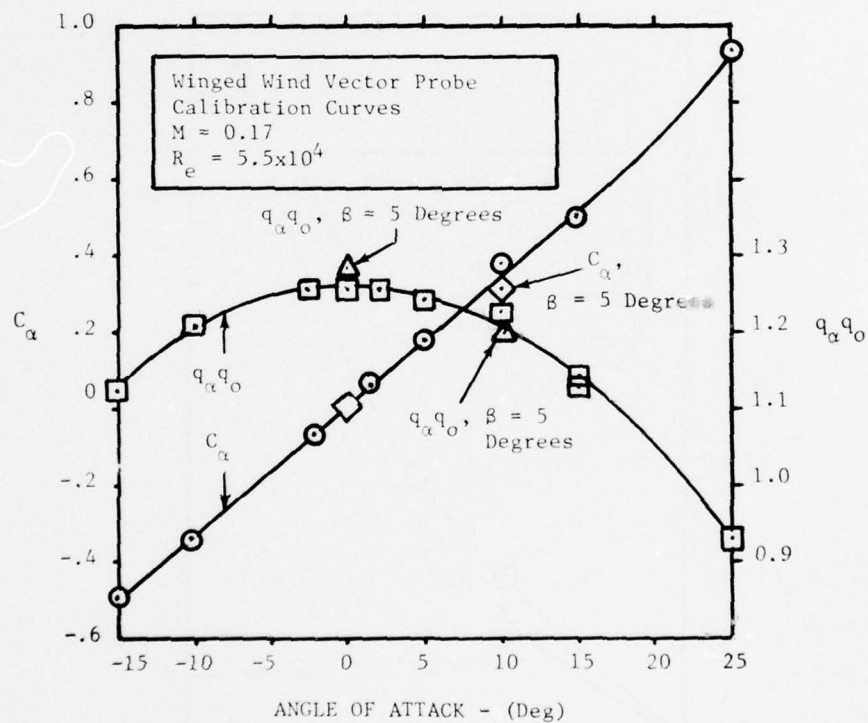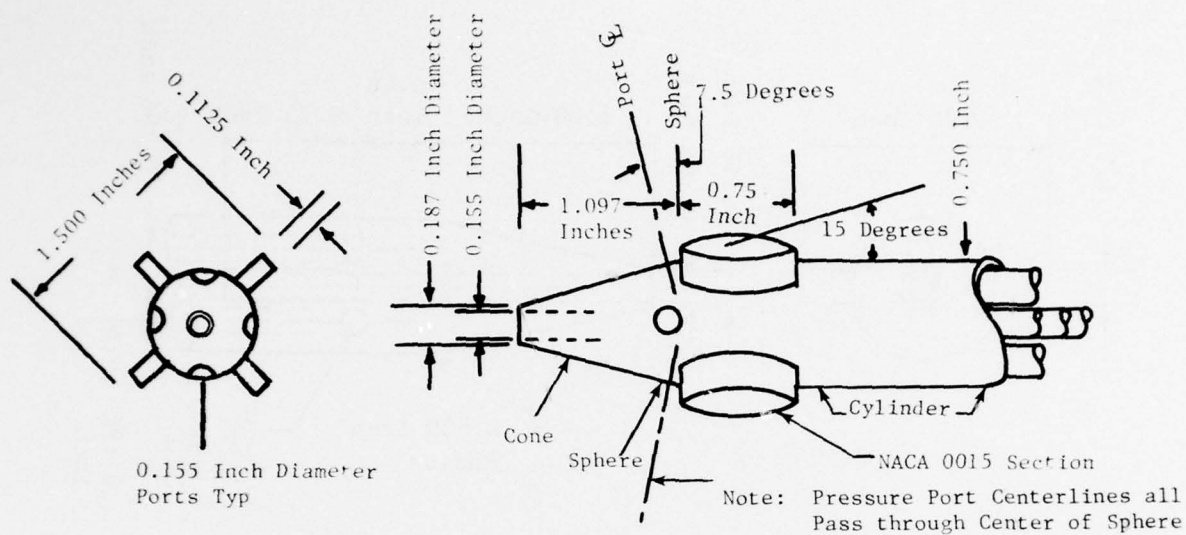
69

Figure 40. Geometry and Calibration of Winged Wind Vector Probe

70

The Winged Wind Vector Probe, whose geometry and calibration curves are shown in Figure 40, was chosen to be included in the flight test. It has good linearity through plus and minus fifteen degrees and acceptable linearity through plus and minus 25 degrees. When used with the diaphragm type pressure coefficient meter, it will maintain a good pressure differential across the diaphragms as indicated by the relatively high values of $q_o q_\alpha$. The few data points taken at a sideslip angle of five degrees indicate low sensitivity to sideslip. The slope of the linear part of the C_α vs. angle of attack curve is 0.034 per degree. In summary, the Winged Wind Vector Probe could be used with the diaphragm type pressure coefficient meter to indicate angle of attack over a 50-degree range.

Combined System Tests--The Hemi-Head Probe was mounted in the test section at zero sideslip on the angle of attack adjusting mechanism, and connected with plastic tubing to the pressure coefficient meter clamped to the tunnel operator's console. The angle of attack was increased from near zero in random steps to a value which caused the pressure coefficient meter indication to approach the positive end of the scale, then reduced in random steps to a value approaching the negative end of the scale, then increased in random steps to near zero. The intent was to generate a hysteresis loop. This procedure was used to avoid having to fine adjust the angle of attack mechanism to reach a precise value and to avoid possibly "backing" into a data point from the wrong direction.

The results of the wind tunnel combined system test are presented in Figure 41. From these hysteresis loops we conclude that the combined system has an accuracy of $\pm$ 0.7 degree at a calibrated airspeed of 61.366 miles per hour, an accuracy of $\pm$ 0.3 degree at a calibrated airspeed of 83.801 miles per hour, an accuracy of $\pm$ 0.1 degree at a calibrated air-speed of 119.566 miles per hour, and an accuracy of better than $\pm$ 0.08 degree at a calibrated airspeed of 161.143 miles per hour. It should be noted that the smallest division on the face of the dial was two degrees. So, one could estimate the output indication to plus or minus 0.5 degree corresponding to plus or minus 0.082 degree angle of attack. Here, the meter indication was about a six-to-one magnification of the angle of attack. One can also conclude that the calibration curve of the combined system is completely independent of the airspeed by overlaying the four parts of Figure 41.

Certain qualitative features of the hysteresis loops deserve comment. First, the "wavy" output at the lowest airspeed is apparently associated with the movement of small wrinkles in the Mylar® diaphragms. This phenomena was discussed under "Pressure Coefficient Meter Assembly" referencing Figures 33 and 34. It shows up in the output much like dry friction with a breakaway coefficient of friction higher than the moving value. Second, the apparent increase in sensitivity near the ends of the range is due primarily to the geometry of the connecting rod and crank mechanism driving the indicating needle and partly to the fact that, for conical diaphragms and backing plates, the movement of the backing plate assembly is greatest for a given C_α change near the ends of the range. (See Figure 11.) Third, the fact that the hysteresis loop does not go
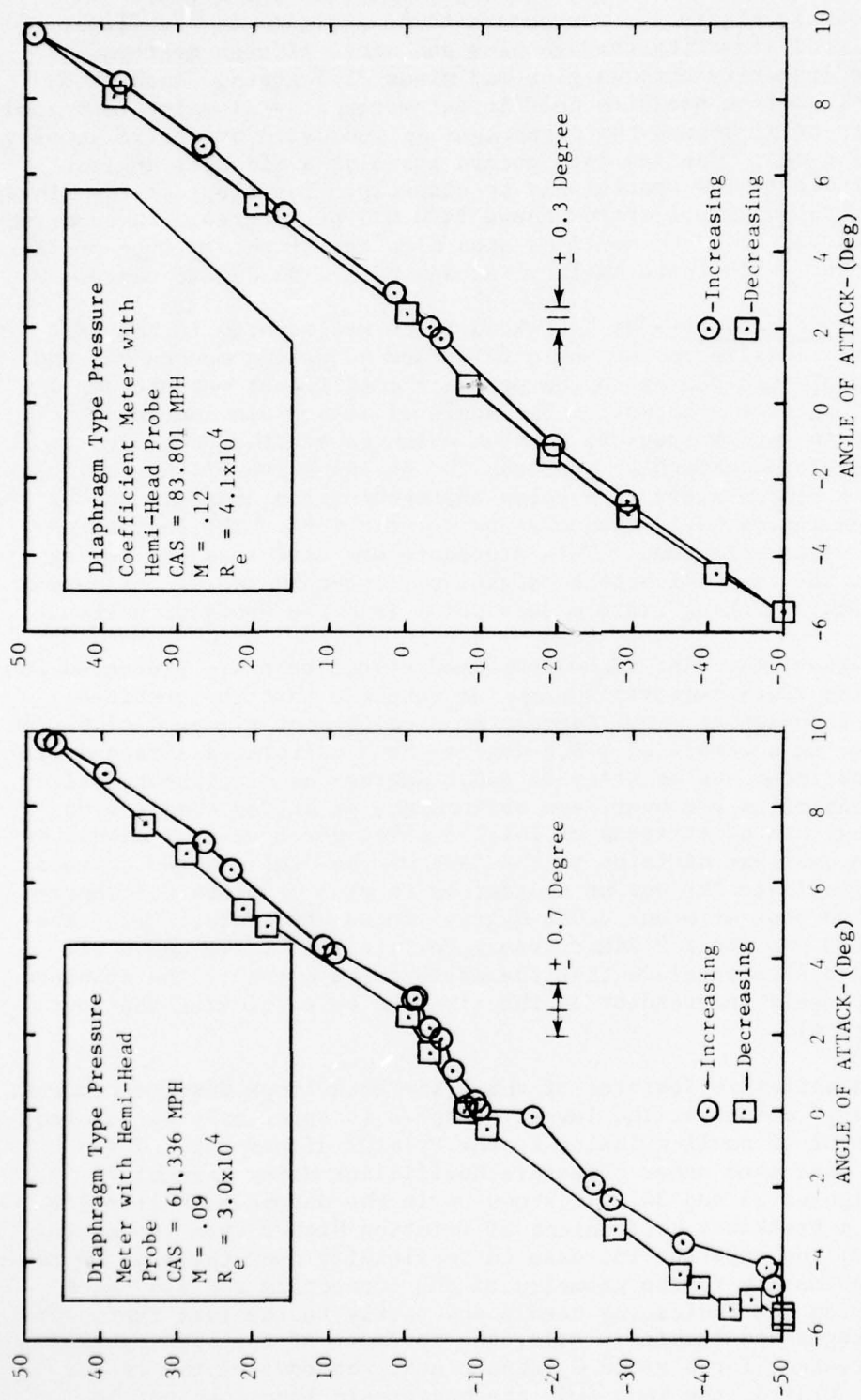
71

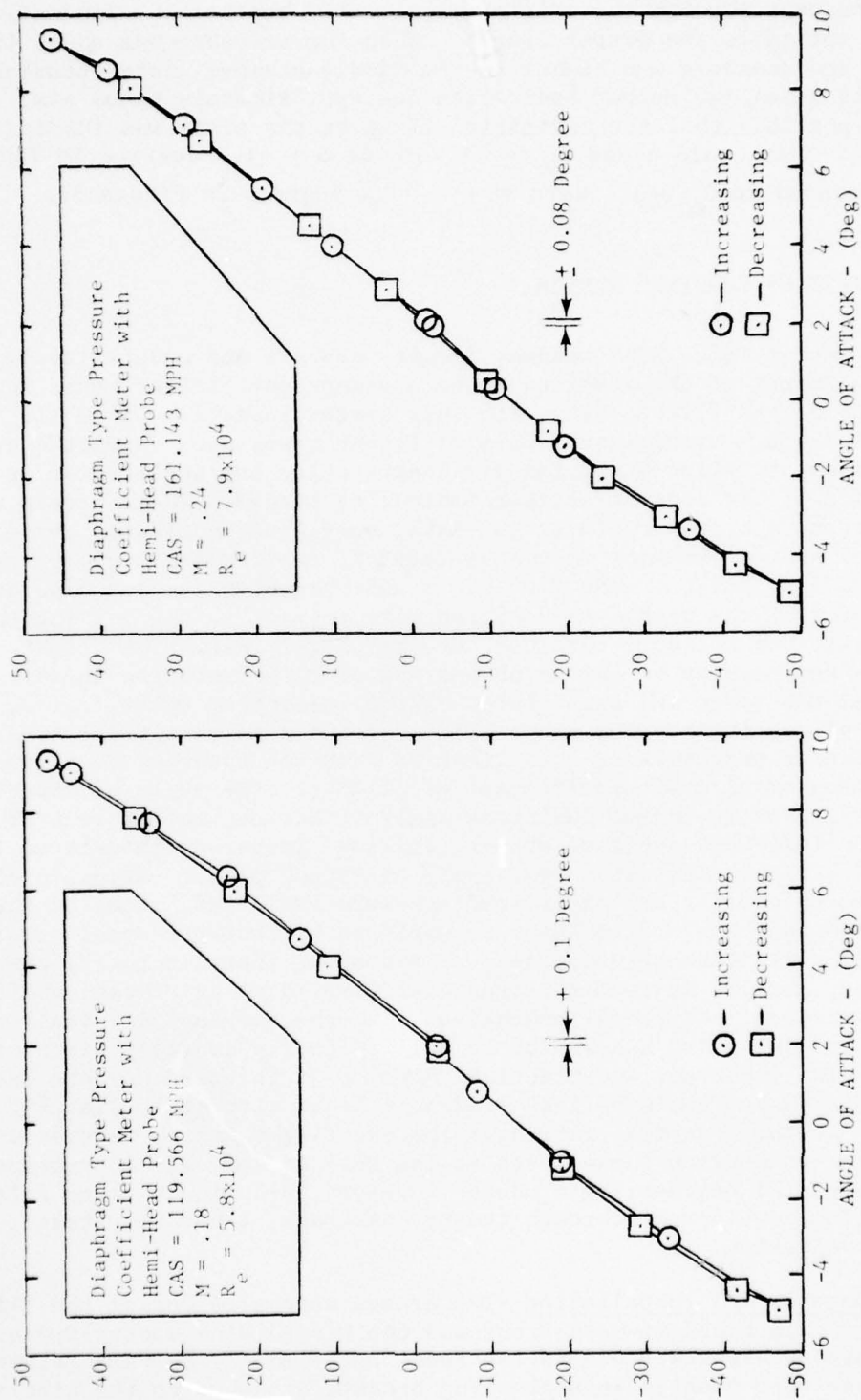Figure 41. Combined System Hysteresis Loops

Figure 41. Combined System Hysteresis Loops (Concluded)

73

around or pass through the origin is primarily because the connecting
rod was not quite the proper length. When the pressure was equal in
the two end chambers and higher in the middle chamber (corresponding to
C_α equals zero), the output indication was approximately minus six. It
is also possible that the definition of up on the probe was inadvertantly
changed. This would cause C_α equal zero at $\alpha = +1.3$ degrees in Figure 41
to correspond to C_α equal zero at $\alpha = -1.2$ degrees in Figure 37.

FLIGHT TEST OF COMBINED SYSTEM

In May of 1974, USAF Academy faculty members and cadets involved in
the development of the combined probe/pressure coefficient meter indicating
system conducted flight tests with this system installed on an Air Force
T-41A aircraft. Twenty-five hours of flight tests were conducted at the
USAF Academy to allow a preliminary quantitative and qualitative on board
evaluation of the angle of attack indicating system. There were a number
of questions not answerable in the laboratory which motivated these tests.
The total system dynamics in the operational environment could be seen as
the overall objective. The flow field near the wing leading edge and the
sensitivity of the probes to position with respect to the leading edge was
most easily and reliably obtained through flight test. The flights pro-
vided an opportunity to change probes and probe orientation in ways which
optimized the range and sensitivity of the indicating meter. Also, this
varying of sensitivity and range allowed for a more complete evaluation of
the indicator performance. Quantitative data was recorded to allow
correlation of aircraft coefficient of lift vs. true angle of attack, true
angle of attack vs. meter indicated angle of attack, coefficient of lift
vs. meter indicated angle of attack, and load factor as calculated from the
aircraft attitude indicator vs. angle of attack meter. Sideslip effects
upon the angle of attack meter readings were evaluated. Some of the
qualitative and subjective features explored by test personnel were:
(1) pilot evaluation of usefulness as a control instrument, (2) comparison
with other cockpit instruments (response time, damping vibration effects,
ease of reading, etc.), (3) comparison with the conventional stall warning
device, and (4) pilot assessment of ability to fly constant pitch attitude
tracks. The important and practical feature of interest was the ease with
which this system could be installed on a light aircraft. Finally, in
addition to the technical rationale for the flight tests, another moti-
vation for conducting these tests at the USAF Academy was to provide broad
training to the engineering students involved, allowing them to follow the
engineering development through theory, hardware, laboratory tests, and
flight evaluation.

Apparatus and Installation--Two probes were used during the flight
tests - namely the Hemi-Head Probe and the Winged Wind Vector Probe. Both
of the probes are described in the section titled "Probe Calibrations."
The probes were mounted in a pivoting bracket attached to the aircraft wing
strut near the strut-wing junction. The pivoting bracket installation is

74

illustrated in Figure 42. This bracket allowed accurate positioning of the probe relative to the aircraft longitudinal axis in both the angle of attack and angle of sideslip planes. In fact, in order to get the meter to operate over the angle of attack range appropriate to the aircraft, systematic adjustments were made to the angle between the aircraft longitudinal axis and the probe axis (viewed from the side) before data was taken. Flexible plastic tubing was routed from the probe through the wing just aft of the main spar and into the cabin. For the tests, the rear seat was removed and an instrumentation bench installed in its place. The instrumentation bench held a transit (used to establish the true angle of attack) and the pressure coefficient meter. The right front seat was reversed in its existing tracks to allow the data taker to face his work. The general arrangement is shown in Figure 43.

Figure 42. Pivoting Bracket

75
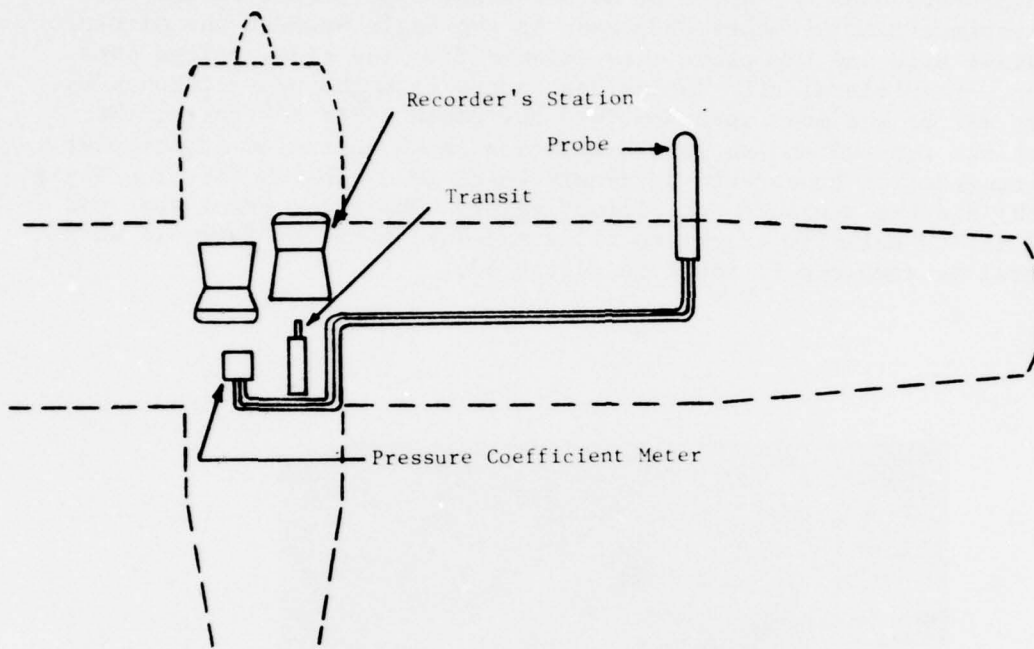
Figure 43. General Arrangement

Flight Test Procedures--Four essentially different procedures were
used, each intended to explore a particular aspect of system performance.
(1) The tower fly-away maneuver produced data which allowed comparison
of optically measured angle of attack to the pressure coefficient meter
indication. (2) Level coordinated turns were flown to demonstrate the
dependence of the indication on g load. (3) The aircraft was slipped
to investigate any dependence of the output indication on sideslip angle.
(4) Flaps were operated to verify the expected shift in the indicated vs.
actual angle of attack curve.

Figure 44 illustrates the idea behind the tower fly-away test. The
aircraft was flown by a tower at the same elevation as the top and the
altitude was noted. Flight continued outbound, directly away from the
tower, at constant altitude and pitch attitude while the data taker
recorded indicated airspeed, the pressure coefficient meter reading, and
the angle of attack measured with the transit.

76

Figure 44. Tower Fly-Away Maneuver
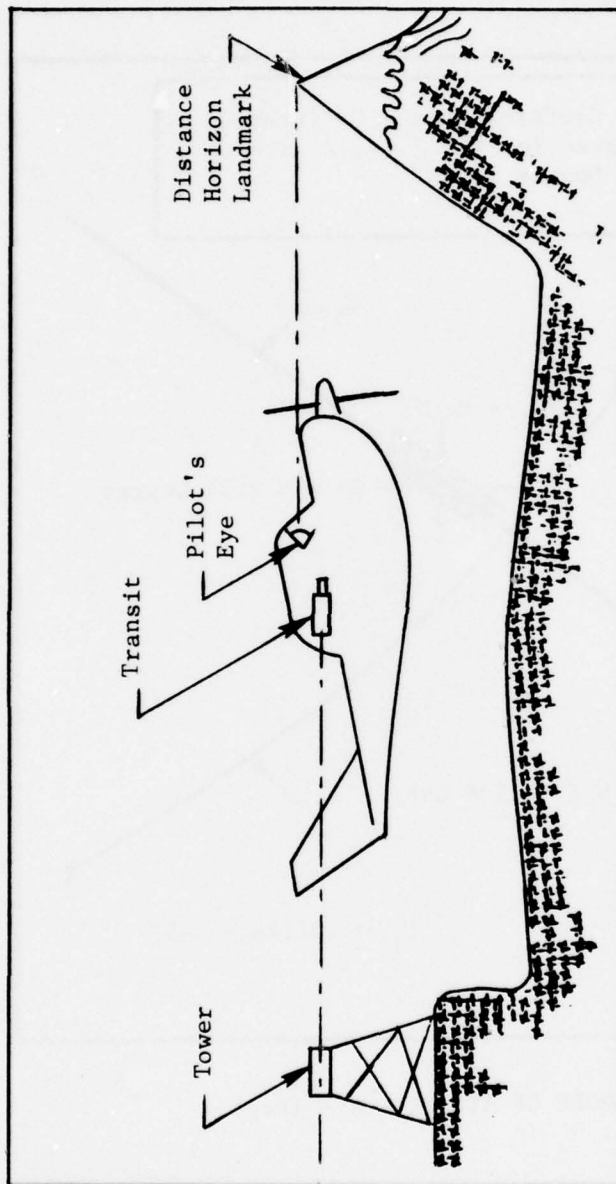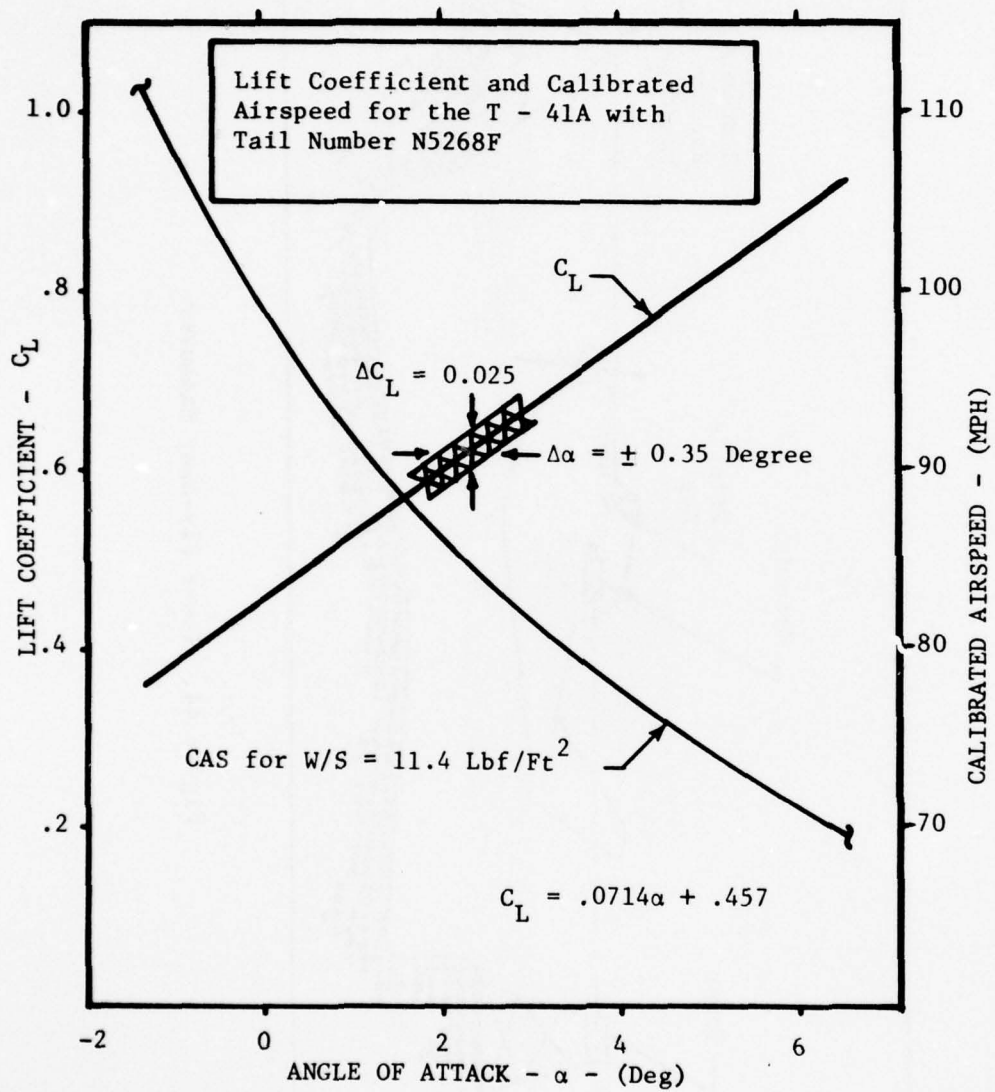
77

Figure 45. Lift Coefficient vs. Angle of Attack for Test Aircraft

The piloting task was rather tedious because it was desirable to hold pitch attitude to within about plus or minus 0.16 degree and altitude to within about plus or minus twenty feet. The best procedure was to shut one eye, and with the head and body very still, hold a speck on the windshield on a point on the horizon using elevator and rudder. Frequent quick glances at the altimeter provided inputs for the minute power changes required to hold altitude. It should be noted that the data taker looking through the transit can easily detect altitude changes by movement of the cross hairs on the tower if the pilot is holding on absolutely constant pitch attitude. In a series of level runs the pitch attitude was varied over a range of about fifteen degrees corresponding to an airspeed range from a safe margin above stall to maximum cruise speed. There are several inaccuracies which can creep into this procedure and which caused us to reduce the data in a seemingly roundabout fashion.

For example, if one was flying at a constant altitude and pitch attitude in a mass of air that was moving vertically at only 100 feet per minute, then the angle of attack measured by the transit would be in error by 0.65 degree at a true airspeed of 100 miles per hour. There was no way to detect this error with the installed instrumentation. If one inadvertently took data while the aircraft's vertical velocity was 100 feet per minute in still air, the same error would occur. However, it is possible to eliminate this potential error by using the airspeed indicator, if one has a good trimmed lift coefficient vs. angle of attack curve for the aircraft and knows exactly the aircraft weight. For comparison, an altitude error of 600 feet at ten miles from the tower, or 60 feet at one mile, is required to induce the same 0.65-degree angle of attack error. If, for some reason, the vertical acceleration was 0.1 g at a calibrated airspeed of 100 miles per hour during data taking; again, a 0.65-degree error would result.

Because of these possible error sources, and because based on our wind tunnel results we expected the accuracy of the instrument to be better than plus or minus 0.65 degree, we decided to use the airspeed indicator as the working standard for evaluating the angle of attack indicator. The airspeed indicator could be read to about plus or minus one mile per hour corresponding to an angle of attack range of plus or minus 0.095 degree at the high speed end of the range and plus or minus 0.36 degree at the low speed end of the range. Therefore, a good calibration of trimmed lift coefficient vs. angle of attack at one g was required.

Results and Discussion--Figure 45 illustrates the trimmed lift coefficient vs. angle of attack curve as determined from the airspeed indicator and current weight for the particular aircraft used. The error band shown includes all points not rejectable by some anomalous test condition, e.g., vertical velocity not zero, not at one g, or not on altitude. The calibrated airspeed vs. lift coefficient curve provided for convenience in Figure 45 is appropriate only for one aircraft weight and is not a calibration curve.

Figure 46 summarizes the only direct comparison of optically measured angle of attack with meter indication, θ. This particular data was taken on an especially quiet day early in the morning. Even so, an error band occurs after all sensibly rejectable points are discarded. This error band of plus or minus 0.25 degree includes angle of attack indicator errors, transit reading errors along with uncertainties associated with the unknown air mass vertical motion. When one compares Figure 46 to the wind tunnel data of Figure 41, the striking difference is the increased sensitivity in the aircraft installation of twelve degrees indicator change for one degree angle of attack change compared to an amplification factor of 6.1 in the wind tunnel. The reason for this difference is the increasing upwash in front of the wing associated with increasing circulation at higher angle of attack.

Having essentially calibrated the aircraft one could calculate lift coefficient from aircraft weight, g load, dimensions, and airspeed and then look up the angle of attack in Figure 45. Figure 47 shows the pressure coefficient meter indication, θ, vs. the computed lift coefficient. Here, the error band includes angle of attack indicator errors and airspeed indicator errors but does not include errors due to vertical movement of the air mass. It is from this data that one can conclude that the pressure driven angle of attack indicator system has an accuracy of plus or minus 0.17 degree in an actual light aircraft installation. This agrees quite favorably with the plus or minus 0.3 degree error band in the second panel of Figure 41 when one takes into account the favorable (for accuracy) amplification effect due to upwash in front of the wing. This amplification effect is unfavorable in the sense that it reduces the useful range of the instrument installation.

In Figure 48 similar data is presented for the Winged Wind Vector Probe. Here the error band is plus or minus 0.28 degree in angle of attack. However, the useful range of the system was extended to include the entire useful angle of attack range of the aircraft. The meter movement permitted output indications in the range $-50^{o} < \theta < +50^{o}$ and the range actually used with the Winged Wind Vector Probe was only $-25^{o} < \theta < 28^{o}$.

Table 5 summarizes some data hurriedly taken in level turns. Load factors calculated from the bank angle are compared to load factor calculated from the angle of attack indicator readings. Errors in the bank angle, ϕ, are considered. The objective was to demonstrate that the angle of attack indication was independent of airspeed in the aircraft as had already been shown in the wind tunnel. Although the trends are in the right direction, the quantitative comparisons are rather poor. This discrepancy is attributable to: (1) ordinary piloting imprecision in flying the turns and (2) lack of aircraft performance precluding steady level turns of two g's.

Finally, there are several lasting pilot and data taker impressions that are significant enough to be recorded. First, the time response

80

Figure 47. Pressure Coefficient Meter Reading vs. Computed Lift Coefficient Using Hemi-Head Probe

Pressure Coefficient
Meter Reading vs.
Lift Coefficient
Hemi-Head Probe
Axis 11 Degrees Nose
Down

$\Delta C_L = \pm .012 \rightarrow \Delta\alpha = \pm 0.17$ Degree

$\Delta\theta = \pm 2$ Degrees
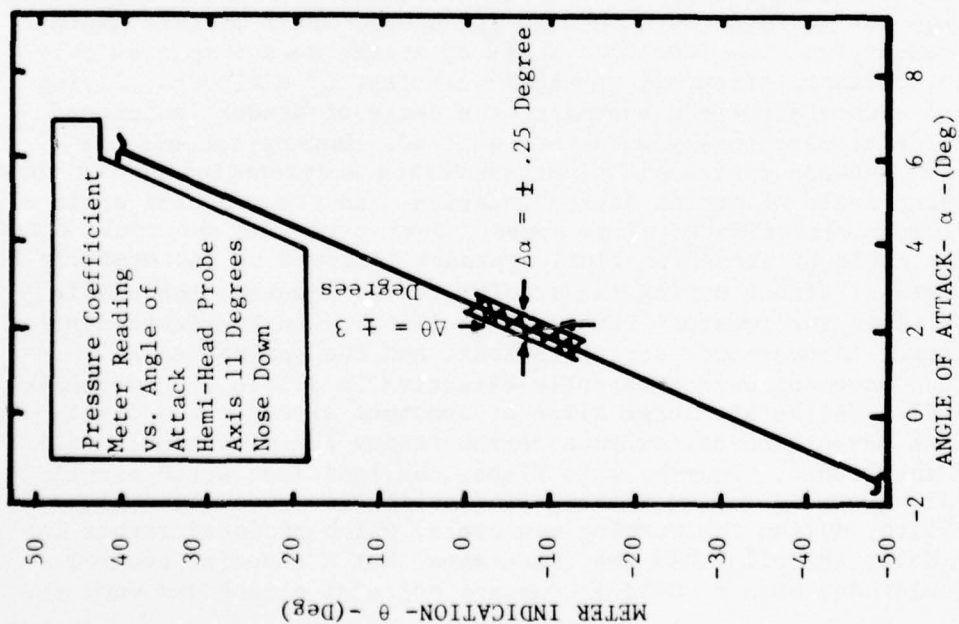
METER INDICATION- θ -(Deg)

LIFT COEFFICIENT- C_L

Figure 46. Pressure Coefficient Meter Reading vs. Optically Measured Angle of Attack

Pressure Coefficient
Meter Reading
vs. Angle of
Attack
Hemi-Head Probe
Axis 11 Degrees
Nose Down

$\Delta\alpha = \pm .25$ Degree

$\Delta\theta = \pm 3$ Degrees

METER INDICATION- θ -(Deg)
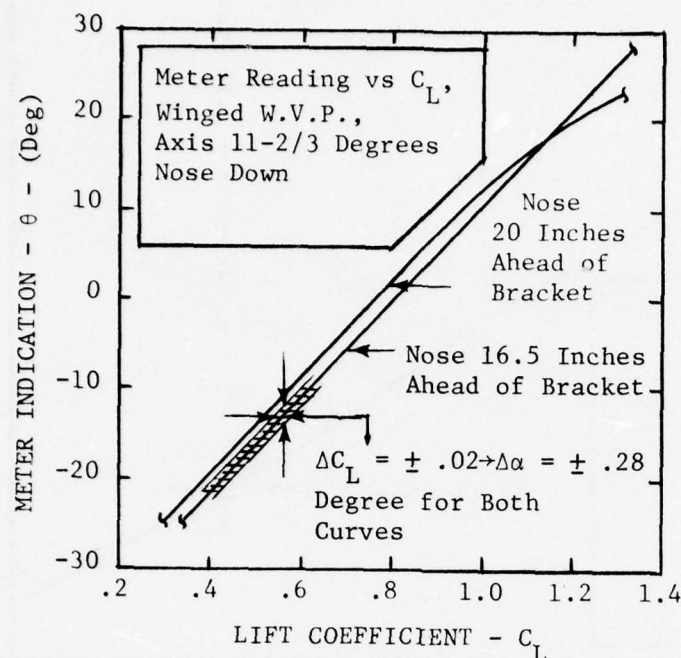
ANGLE OF ATTACK- α -(Deg)

81

Figure 48.   Pressure Coefficient Meter Reading
vs. Computed Lift Coefficient Using
Winged Wind Vector Probe

was certainly adequate for pilot use. In fact, one formed the impression
that this was the fastest instrument in the cabin. Part of this impres-
sion must result from the fact that angle of attack does change quickly
compared to attitude, airspeed, vertical velocity, or altitude. Flying
into typical summer afternoon thermals, the angle of attack indicator
seemed to rise simultaneously with the g load. During takeoff one
could observe the constant angle of attack during acceleration on the runway,
the increasing angle of attack during rotation, and the reducing angle of
attack during acceleration to climb speed. During landing one could observe
the constant angle of attack on final approach followed by the steadily in-
creasing angle of attack during the landing flare. Second, the needle
was very steady. The pressure forces in equilibrium in the instrument
were sufficient to overpower any vibrations, and the spring loaded
pivots in the movement were apparently effective in eliminating mechanical
play. Thirdly, deliberate large slips at constant airspeed had little
effect on the output indication, thus corroborating the wind tunnel cali-
bration of the probes. Fourth, with flaps, the indicator acted exactly
as in the clean configuration although the calibration was obviously
changed. Fifth, during the turning maneuvers, which produced rather in-
conclusive data, the pilot had the impression that a superior control
strategy would have been to hold a constant angle of attack and vary the

bank angle slightly to maintain altitude. Unfortunately this was not possible due to the position of the instrument in the aircraft during the test.

<div align="center">TABLE 5.   LEVEL TURN RESULTS</div>

CAS (mph)	ϕ	n_ϕ	n_θ
92	30°	1.15	1.40
93			1.42
91			1.38
103			1.14
106			1.19
100	45°	1.41	1.55
101			1.63
98			1.58
101			1.63
102			1.39
103			1.34
102			1.34
104	30°	1.15	.99
103			1.02
106	45°	1.41	1.18
106			1.18
101	60°	2.00	1.47
103			1.48

Note on Error Sources:

(1) Bank Angle Flown; ϕ, $\pm\ 7°$
→ $\Delta n_{(\phi)} = \pm$ .10, 30°
.20, 45°
.50, 60°

(2) q Error; CAS Error due to the change in C_L vs V for turns. If CAS is ± 2 mph → $\Delta n_{(q)} = \pm$ .07

(3) AOAI Error; $\pm$ .025 C_L → $\Delta n_{(\theta)} = \pm$ .05

n_ϕ = load factor calculated from bank angle, ϕ

n_θ = load factor calculated from pressure coefficient meter reading, θ

SECTION VI

CONCLUSIONS

A unique pressure driven angle of attack indicating system consisting of an external element (usually a separate probe, although, the aircraft nose or wing leading edge can be used instead) and an internally mounted indicator or sensor called the pressure coefficient meter has been invented, designed, built, and tested.

Accuracy limits are not known precisely. However, test results verify that satisfactory accuracy for many applications has been achieved. The width of hysteresis loops determined from wind tunnel tests can be roughly correlated by

$$\Delta \alpha \text{ (degrees)} = \pm \frac{0.288}{q \left[\frac{\text{lbf}}{\text{ft}^2} \right]} \quad .$$

The useful range in these tests was about fifteen degrees. With the probe used in this particular series of tests the diaphragm material would have yielded at about $q = 401$ lbf/ft². If one adopts an accuracy requirement of $\pm 1\%$ of the instrument range, i.e., ± 0.15 degree in this case, then this system as tested would be useful over a range of 35 lbf/ft² $< q < 401$ lbf/ft² which corresponds to a calibrated airspeed range of $116 < CAS < 396$ miles per hour. The wind tunnel and flight testing was mostly outside this range on the low end with the highest calibrated airspeed for wind tunnel tests being 161 miles per hour and the highest calibrated airspeed for flight tests being 122 miles per hour. During the wind tunnel tests accuracies from ± 0.7 degree to ± 0.08 degree were achieved depending on airspeed. During the flight tests accuracies from ± 0.17 degree to ± 0.28 degree were achieved depending on the probe installed.

Based on the design of the pressure driven angle of attack indicating system one can conclude that: this system is as rugged as any in existence; is more resistant to foreign object damage than any other system; is less expensive than any other system; has great freedom of mounting positions comparable to the best of other systems; and is totally independent of all other aircraft systems. A discussion of these comparisons is found in the "Introduction."

Probes for the pressure driven angle of attack indicating system can be designed for almost any range and sensitivity. Design principles are given under "Probe Design Considerations." Examples of two successful probe calibrations of different sensitivities and range are given under "Probe Calibrations." The most sensitive probe tested had a probable useful range of about twenty degrees and a sensitivity of $dC_\alpha/d\alpha = 0.094$/degree. The less sensitive probe tested had a useful range of about 50 degrees and a sensitivity of $dC_\alpha/d\alpha = 0.034$/degree.

Mylar® can easily be heat and pressure formed into the rather shallow dish-like shapes desirable for diaphragms. The procedure is described under "Pressure Coefficient Meter Construction."

The Mylar® diaphragms will last more than 2000 complete cycles before failure which translates to about 3000 hours of easy cross country flying. The fatigue test is described under "Diaphragm Fatigue Test."

Numerous formulas have been developed to aid engineers in the design of pressure coefficient meters for almost any application. Specifically, procedures have been developed to: (1) derive calibration curves; (2) design for maximum expected pressures; (3) predict changes in calibration curves caused by changes in pressure level while pressure coefficient remains constant; (4) predict inaccuracies due to friction; (5) predict response characteristics for laminar flow in connecting tubes; and (6) predict erroneous readings due to acceleration. By careful use of these formulas the engineer can design the best pressure coefficient meter for his application. These design formulas are presented under "Pressure Coefficient Meter Design Considerations."

The process of interfacing a probe with a pressure coefficient meter to yield desirable overall system range, sensitivity, acceleration tolerance, and other performance characteristics has been demonstrated with two specific examples. These examples are presented under "Pressure Coefficient Meter and Probe Interfacing."

During flight tests, response characteristics of the pressure driven angle of attack indicating system were found to be ideal for pilot use.

REFERENCES

1. Lambdin, R. L., "Standarized Angle of Attack System Feasibility Study," Aeronautical Systems Division Technical Memorandum, ASNF 68-4, August 1968.

2. Gunship Operational Flight Program, Part II, Specification for Gunship Software Product Specification, Volume II, Prepared for Gunship System Program, Air Force Systems Command, Wright Patterson Air Force Base, Ohio, Contract F33-657-71-C-0595, 15 Sept 1971 Revised 17 Sept 1973, IBM File No. 71-M-54-001.

3. D. Donato, A. R., Jarnagin, M. P., Jr., and Hageman, R. K., "The Preyss-Willes Method in Air to Air Gunnery-Proofs and Computer Evaluation," U. S. Naval Weapons Laboratory Technical Report TN-K-64/73, Dec 1973.

4. Gilbert, S. W., Preyss, A. E., and Willes, R. E., "Snap-Shoot Gunsight for Fixed-Gun Fighter Aircraft," USAF Academy Technical Report TR-69-3, Dec 1969.

5. Leatham, A. L., Durrette, J. C., and Alfano, S., "Digital Lead Computing Optical Sight Model," USAF Academy Technical Report, USAFA-TR-74-17, Sept 1974.

6. Dendy, J. B. and Transier, K. G., "Angle of Attack Computation Study," Air Force Flight Dynamics Laboratory Technical Report, AFFDL-TR-69-93, October 1969.

7. Mellinger, B. L., Kramer, R. M., Griffiths, D. M., et al., "Design Definition Study Universal Stall Margin Indicating System," Aeronautical Systems Division Technical Report, ASD-TR-69-91, December 1969.

8. Freeman, D. B., "Angle of Attack Computation System," Air Force Flight Dynamics Laboratory Technical Report, AFFDL-TR-73-89, October 1973.

9. Webb, J. A., "Static Stability and Control Effectiveness of the MK-84 Modular Guided Glide Bomb II at Transonic Mach Numbers," Arnold Engineering Development Center Report AEDC-TR-74-58 or Air Force Armament Laboratory Report AFATL-TR-74-99, July 1974.

10. Advisory Group for Aerospace Research and Development, Paris (France), "Methods for Aircraft State and Parameter Identification," N75-29997, May 1975, Meeting held at Hampton, VA, 5-8 Nov 1974.

11. Department of Transportation, Federal Aviation Administration, Flight Standards Service, "Flight Instructors Handbook," Revised 1969.

12. Blodget, R., "What's It All About, Alpha?" Flying Magazine, November 1971.

13. Garrison, P., "Angle of Attack Indicator," Flying Magazine, April 1973.

14. Kohlman, D. L. and Brainerd, C. H., "Evaluation of Spoilers for Light Aircraft Flight Path Control," Journal of Aircraft, Vol II, No. 8, Aug 1974.

15. Yaffee, M. L., "New Controls to Shape Future Aircraft," Aviation Week and Space Technology, October 16, 1972.

16. Rosemount promotional brochure, "Model 858 Flow Angle Sensors," Bulletin 1014, 1974, Rosemount Inc., Post Office Box 35129, Minneapolis, Minnesota 55435.

17. Pringle, G. E., "Stall Warning Devices," A.R.C. 5049, 1941.

18. Rettie, I. H., "An Investigation of the Velocity Distribution Around the Nose of the Aerofoil with a Flap," Reports and Memoranda No. 3027, May 1955.

19. Schuck, O. H., "Angle of Attack Indicating Device," U. S. Patent No. 2,948,149, Aug 9, 1960.

20. Beecham, L. J. and Collins, S. J., "Static and Dynamic Response of a Design of a Differential Pressure Yawmeter at Supersonic Speeds," RAE Report No. GW 19, February 1954.

21. Dean, R. C., Jr., "Aerodynamic Measurements," The MIT Press, 1953, (Chapter VI - Flow Direction Measurements).

22. Hutton, P. G., "Static Response of a Hemispherical-Headed Yawmeter at High Subsonic and Transonic Speeds, RAE Technical Note No. Aero 2525, CP No. 401, Aug 1957.

23. Rogal, B., "Differential Pressure Measurements in Sensing Sideslip and Angle of Attack," Flight Test Instrumentation Proceedings of the Third International Symposium - 1964, Vol 3, M. A. Perry, ed., Pergamon Press, 1965, pp 1-22.

24. Nowack, C. F. R., "Improved Calibration Method for a Five-Hole Spherical Pitot Probe," Journal of Physics, Part E - Journal of Scientific Instruments, Vol. 3, Jan 1970.

25. Wright, M. A., "The Evaluation of a Simplified Form of Presentation for a Five-Hole Spherical and Hemispherical Pitometer Calibration Data," Journal of Physics, Part E - Journal of Scientific Instruments, Vol 3, May 1970.

26. Armistead, K. H. and Webb, L. D., "Flight Calibration of a Nose-Boom-Mounted Fixed Hemispherical Flow-Direction Sensor," NASA TN D-7461, October 1973.

27. Dau, K., McLeod, M., and Surrey, D., "The Probes for the Measurement of the Complete Velocity Vector in Subsonic Flow," Aeronautical Journal, Vol 72, December 1969.

28. Bryer, D. W., Walshe, D. E., and Garver, H. C., "Pressure Probe
Selected for Three Dimensional Flow Measurements," ARC R&M 3037, 1958.

29. Dudzinski, T. J. and Krause, L. N., "Flow Direction Measurements
With Fixed-Position Probes in Subsonic Flow Over a Range of Reynolds
Numbers," NASA TM X 1904, N69 40059, 1969.

30. Rojaratnam, N. and Muralidhar, D., "Yaw Probe Used as Preston Tube,"
Aeronautical Journal, Vol 72, A69 16396, Dec 1969.

31. Liepmann, H. W. and Roshko, A., "Elements of Gasdynamics," John
Wiley & Sons, 1957.

32. Herrington, R. M., Shoemaker, P. E., Bartlett, E. P., and Dunlap,
E. W., "Pressure Lag Error--Theory and Calibration," Flight Test
Engineering Handbook, Ch. 1, Sec. 4, Tech. Rep. No. 6273, Air Force
Flight Test Center, May 1951 (rev. June 1964), pp. 28-47.

33. Turner, K. J., "Free Flight Model Techniques for Aerodynamic Research
at Supersonic and Hypersonic Speeds," Flight Test Instrumentation, Vol 3,
Proceedings of the Third International Symposium, 1964, M. A. Perry, ed.,
Pergamon Press, pp 227-247.

34. Lamb, Sir Horace, "Hydrodynamics," Dover Publications, New York,
6th Edition, 1932.

35. Kuethe, A. M., and Schetzer, J. D., "Foundations of Aerodynamics,"
John Wiley and Sons, Inc., 2nd Edition, 5th Printing, October 1964.

36. Chernyi, G. G., "Introduction to Hypersonic Flow," Academic Press,
New York and London, 1961.

37. Markarieni, F., "Experimental Surface Pressure Distribution on Three
Bodies of Revolution from M = 0.7 to M = 2.2," Naval Weapons Center,
NWC-TT-5393, AD-749934, August 1972.

38. Frage, A., Aeronautical Research Council Reports and Memoranda,
No. 1966, 1937.

39. Trumbull, K. and T. Carter, "A Report on the Wind Vector Probe,"
Aero 350 Laboratory Report, Dept of Aeronautics, USAF Academy, Dec. 1973.